Kerr Nonlinear Instability: Classical and Quantum Optical Theories

Michael Nesrallah

A thesis submitted in partial fulfillment
of the requirements for the degree of
Doctor of Philosophy in Physics
at the University of Ottawa

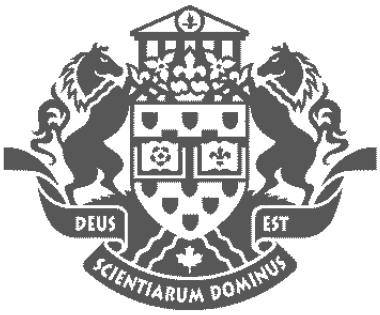

Abstract

An important aspect of third-order optical nonlinearity is the intensity-dependent refractive index, where the intensity of the light itself affects the refractive index. This nonlinear effect is known as Kerr nonlinearity. In this work, a theory of amplification based on Kerr nonlinearity is developed.

Kerr nonlinearity is well known to exhibit instability. Our amplification theory is based on seeding this instability. The full theory is developed to obtain the vectorial wave equations of the instability. It is shown that for materials of interest, vectorial effects are negligible across the instability regime and the scalar theory gives an accurate account of Kerr instability amplification. It is also shown that this instability analysis is a spatiotemporal generalization to four-wave mixing, modulation instability, and filamentation instability. It fact, it can be considered a seeded conical emission process.

Subsequently, the theory of plane wave Kerr instability is explored. Quantitatively, the importance of pump wavelength, linear dispersive properties, and non-collinear angles for optimal amplification are demonstrated.

Next, the seed beam is generalized to a finite Gaussian pulse in both time and space; the effect of a finite seed beam is quantitatively analyzed. Our analysis of Kerr instability in bulk dielectric crystals demonstrates the potential to amplify pulses in the wavelength range of $\sim 1 - 14\,\mu$m. Whereas plane wave amplification is shown to extend to $40\,\mu$m in the example materials shown, material damage limits finite pulse Kerr instability amplification to about $14\,\mu$m. There, seed pulse output energies in the $50\,\mu$J range appear feasible with a ratio of pump to seed pulse energy in the range $400-500$. Three key aspects of Kerr amplification are the capacity for single cycle pulse amplification, that it is intrinsically phase-matched, and its simplicity and versatility.

As the Kerr instability gain profile is of Bessel-Gaussian nature in the transverse space domain, it lends itself naturally to the amplification of Bessel-Gauss beams. It is shown that pump-to-seed energy amplification that is more efficient than the Gaussian case by a factor of about $5 - 7$. Whereas in the Gaussian case, the efficiency is on the order of about $0.15 - 0.2\%$, in the Bessel-Gaussian case it is on the order of about 1%. It is also demonstrated that Bessel-Gaussian seed beams centered at longer wavelengths than ordinary Gaussian beams may be amplified. Lastly, Bessel-Gauss beams are known to have favourable properties, such as being diffraction-free over a certain propagation range.

Finally, a quantum optical theory of Kerr instability is developed. In particular, we explore a theory of the generation of ultrashort photon pairs (biphotons) from vacuum with Kerr instability.

Acknowledgements

I want to thank my supervisor and teacher, Dr. Thomas Brabec. He has taught me more than just physics. He taught me by example what it means to be a good supervisor. This thesis is only possible because of his patient guidance.

For my family

List of publications related to this work

1. M. Nesrallah, G. Vampa, G. Bart, P.B. Corkum, C.R. McDonald and T. Brabec, "Theory of Kerr instability amplification", Optica 5(3), 271278 (2018).

2. G. Vampa, T. J. Hammond, M. Nesrallah, A. Yu Naumov, P. B. Corkum and T. Brabec, "Light amplification by seeded Kerr instability", Science 359, 673–675 (2018).

3. M. Nesrallah, A. Hakami, G. Bart, C. R. McDonald, C. Varin, and T. Brabec, "Measuring the Kerr nonlinearity via seeded Kerr instability amplification: conceptual analysis," Opt. Express 26(6), 76467654 (2018).

4. M. Nesrallah, T. J. Hammond, A. Hakami, G. Bart, C. R. McDonald, T. Brabec, and G. Vampa, 'Kerr Instability Amplification', in Light Filaments: Structures, Challenges and Applications, IET, (to be published 2019).

Contents

List of Figures

1 Introduction

In this work, a general and comprehensive theory of an amplification scheme based on Kerr nonlinearity is developed. Kerr nonlinear optics is an extension to linear optics which includes a nonlinear index of refraction responding quadratically to an applied electric field. This is described mathematically by considering Taylor expansion of the polarization vector as a power series of the electric field vector [1], $\boldsymbol{E}$,

$$\boldsymbol{P} = \epsilon_0 \chi^{(1)} \boldsymbol{E} + \varepsilon_0 \chi^{(2)} \boldsymbol{E}^2 + \epsilon_0 \chi^{(3)} \boldsymbol{E}^3 + ..., \tag{1}$$

where ϵ_0 is the vacuum permittivity. The first-order term is linear in the electric field and $\chi^{(1)}$ is the first-order electric susceptibility, responsible for the linear refractive index. The second-order electric susceptibility tensor, $\chi^{(2)}$, in the expansion typically vanishes identically due to centrosymmetry [1]. Even if it doesn't, we can still directly study the effects of Kerr nonlinearity in noncentrosymmetric material [2]. The third-order term gives rise to the Kerr nonlinearity, where $\chi^{(3)}$ is the third-order electric susceptibility tensor and is clearly cubic in the electric field. This nonlinear term will be the basis of this work. Furthermore, isotropic materials in the presence of linearly-polarized light are of interest, so this reduces the general tensor $\chi^{(3)}$ to a scalar [1] and where $\boldsymbol{E}^3 = (\boldsymbol{E} \cdot \boldsymbol{E})\, \boldsymbol{E}$. The polarization vector of interest then becomes:

$$\begin{aligned} \boldsymbol{P} &= \epsilon_0 \chi^{(1)} \boldsymbol{E} + \epsilon_0 \chi^{(3)} \boldsymbol{E}^3 \\ &\equiv \boldsymbol{P}^{(1)} + \boldsymbol{P}^{(3)}. \end{aligned} \tag{2}$$

Eq. (2) is the basis for Kerr nonlinear optics[1].

It is well-known that Kerr nonlinearity exhibits both spatial (filamentation) [5], and temporal (modulation) instability [6].

The onset of filamentation instability is the result of a single, intense beam propagating in a Kerr nonlinear material having small perturbations in the form of noise that can become exponentially amplified. The noise drastically modifies the beam given a long enough propagation distance, and the beam can eventually form narrow filaments. A complete theory of all the exact mechanisms behind filamentation is still debated [3, 4, 7–13], but the onset is certainly due to transverse Kerr instability as originally described by Bespalov and Talanov [5]. Mathematically, for the onset of the filamentation process, one perturbs the electric field in the nonlinear transverse wave equation and finds the wavevector solution for the perturbation. There are two transverse wavevectors symmetrically about the pump

[1]Note that this regime of nonlinear optics is known as the perturbative regime, perturbative in the sense of expanding the polarization vector as a power series in the electric field. This formalism is valid for moderate to high intensities, but becomes questionable for very high intensities, where the nonlinearity has been observed to saturate and even change from positive to negative in sign [3, 4]. For what follows in this work, the perturbative regime of nonlinear optics is used and is sufficient, except in Chapter **??**, where the non-perturbative regime of nonlinear optics is explored on purpose.

wavevector that correspond to maximum instability, which are amplified and extract energy from the pump. As this process ensues, the laser beam breaks up into many filaments.

Note that filamentation can occur in any dielectric, such as glass, air, or liquids [5, 7]. In fact, the first evidence of filamentation was seen as filamentary damage tracks in glass [14]. Next, consider modulation instability, which is a temporal instability effect.

In general, modulation instability is a perturbation to a periodic waveform that is reinforced by nonlinearity. In the field of optics, modulation instability is usually studied within nonlinear fiber optics, the basis of which is taken from the Nonlinear Schrödinger equation (NLSE) [6]. As will be evident in Chapter 2, the NLSE is a wave equation that is a limiting case of the wave equation developed in the work of this thesis. Analogously to filamentation instability, a well-established stability analysis [6] may be done to show that there is an instability regime that exists whereby perturbations from an intense beam are reinforced by the Kerr nonlinearity. Of course, this is provided the material exhibits appropriate dispersive properties−namely, negative group velocity dispersion−leading to the generation of spectral sidebands and the eventual breakup of the waveform into a train of pulses. Both filamentation and modulation instability will be explicitly shown to be limiting cases of our general spatiotemporal instability, seen in section 2.3.

When both spatial and temporal effects are considered in the third-order optical instability analysis, a phenomenon known as conical emission [15] can ensue. That is, the emission of broadband radiation at a frequency-dependent angles to the filament [7, 15, 16], forming rings of different colours when viewed on a screen in the far-field. This is discussed further in Chapter 5.

In this work, it is shown that a different regime of conical emission occurs when the Kerr instability is seeded by a second pulse at a noncollinear angle. A general and unifying theory is presented to model this phenomenon that has been previously been understood only in terms of four-wave mixing optical parametric amplification (FWOPA) [17–19], a four-wave mixing (FWM) process. In this regime, the seed pulse experiences substantial growth through amplification long before filamentation occurs, as in Fig. 1. As the seed beam is amplified via the Kerr instability, this process is called Kerr Instability Amplification (KIA). The pump and seed beams are aligned noncollinearly at the angle of maximum amplification that depends on the seed pulse frequency. Conical emission−whether unseeded or seeded, requires high intensity laser beams acting as the energy pumps for the process. In section 2.6 we discuss the relation between KIA and FWM. The initial equations of KIA and FWM are shown to be identical in the appropriate generalization of FWM. Thus, it is shown that the theories of FWM, modulation instability, and filamentation instability, are unified under one over-arching theory of KIA. Before proceeding with KIA, the fundamentals of OPAs, both second-order, and third-order (FWOPAs) will be discussed in further detail.

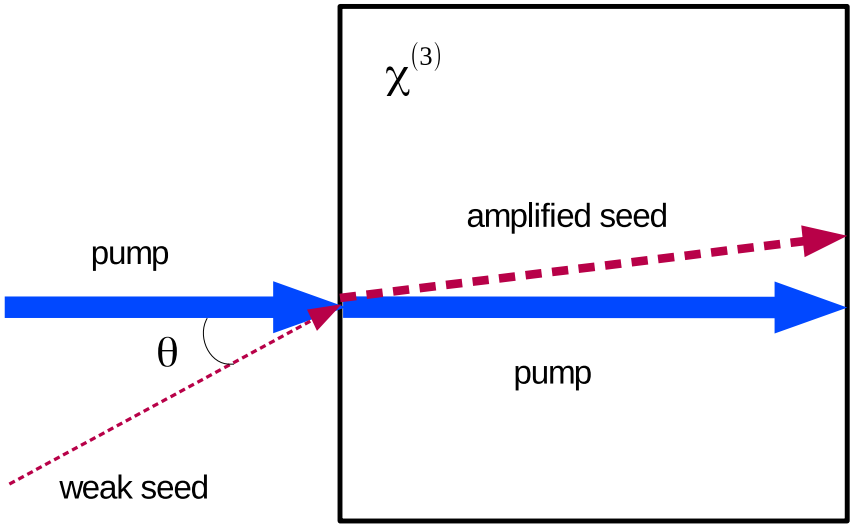

Figure 1: Schematic of seeded Kerr instability amplification. A strong, monochromatic pump beam (thick solid blue arrow), interacts non-collinearly at an angle θ with a weak monochromatic seed beam (thin dashed red arrow) in a $\chi^{(3)}$ nonlinear medium. Through Kerr nonlinear instability, the seed beam is amplified (thicker dashed red arrow). The pump beam remains approximately undistorted.

1.1 Optical Parametric Amplifiers

Why are we concerned with OPAs? Development of high intensity, ultrashort laser sources in the mid-infrared is crucial for advancements in strong field physics and attosecond science [21–23]. Currently, the most common generation and amplification methods are the OPAs based on the second-order nonlinearity with optical phase matching gratings [24–26]. In this section, we describe the fundamental physics behind OPAs, both with second- and third-order nonlinearity. First, second order OPAs, based on $\chi^{(2)}$ nonlinearity, are a parametric difference-frequency generation (DFG) process [1]. The process is schematically depicted in Fig. 2.

As shown in Fig. 2, optical waves at frequencies ω_1 and ω_2 interact in a second-order ($\chi^{(2)}$) medium. The process conserves energy, producing an output wave at the difference frequency, $\omega_3 = \omega_1 - \omega_2$. As such, it is called a parametric process. One of the input waves, say the one with frequency ω_1 is considered the strong pump, remaining approximately undistorted (constant). Coupled wave equations can be obtained for the waves at frequencies ω_2 and ω_3, as done in Ref. [1]. Along with conservation of energy, momentum must be conserved, where each wave has its associated wavevector $k_{1,2,3}$. As a result, in the coupled wave equations, there is an associated phase mismatch, $\Delta k = k_1 - k_2 - k_3$. Solving these coupled wave equations yields exponential growth, and hence amplification. However, for appreciable gain, the phase mismatch must vanish, $\Delta k = 0$ must be satisfied.

Recently, the potential for single cycle infrared pulse generation by difference frequency

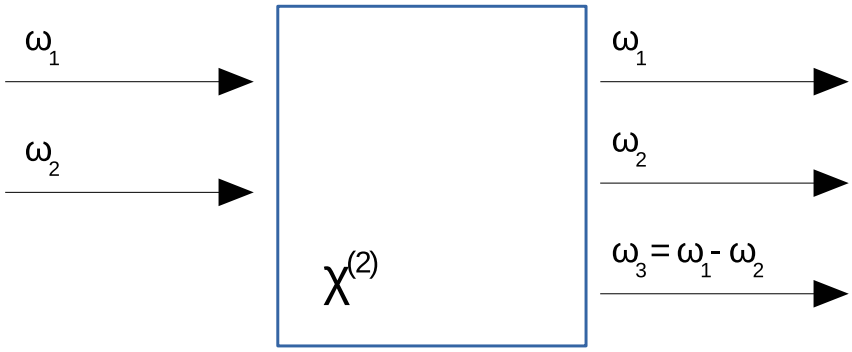

Figure 2: Schematic of difference frequency generation.

generation has been demonstrated [27]. State of the art OPAs supply amplification factors of up to 3 orders of magnitude with amplified pulses in the ten μJ energy range depending on seed wavelength, corresponding to 5-10% of the pump energy.

Although OPAs are currently the leading technology for ultrashort mid-infrared pulse amplification, their development is challenging. For their efficient operation a series of stringent conditions must be met which are intrinsically linked to the nonlinear crystal properties, e.g. phase-matching must be enforced. Amplification of single-cycle pulses either requires thin crystals−reducing the efficiency−or low dispersion across a spectrum covering the frequencies of the three interacting waves. Moreover, many second-order nonlinear crystals absorb light in the mid-infrared, and moderate damage thresholds also present a limitation.

Next, we consider FWOPAs, the $\chi^{(3)}$ analogue to the OPA process. Schematically, the process is described by four-wave mixing.

In Fig. 3, optical waves at frequencies ω_1, ω_2, and ω_3 interact in a third-order ($\chi^{(3)}$) medium. The process is also parametric, conserving energy, producing an output wave at the frequency, $\omega_4 = \omega_1 + \omega_2 - \omega_3$. In degenerate FWM, $\omega_1 = \omega_2$ are equal and considered to be the strong pump waves. In that case, the parametric process becomes $\omega_4 = 2\omega_1 - \omega_3$. Typically, ω_1 is called the pump wave, $\omega_1 \equiv \omega_p$, ω_3 the signal wave, $\omega_3 \equiv \omega_s$, and ω_4 the idler wave, $\omega_4 \equiv \omega_i$. This terminology will be used when comparing KIA to FWM in Chapter 2. Again, the strong pump is assumed to remain approximately undistorted (constant). Coupled wave equations can be obtained for the waves at frequencies ω_s and ω_i, as shown in Section 2.6. However, in that section, in order to correspond with KIA theory, the waves are treated more generally. Thus, the explicit phase mismatch is not shown in those equations. The explicit phase mismatch is obtained in the coupled wave equations by a simple transformation of the waves, factoring out their wavevectors $k_{s,i}$; see for example, Ref. [1]. The resulting phase mismatch is defined by $\Delta k = 2k_p - k_s - k_i$. As before, for optimal amplification, $\Delta k = 0$ is required. Below, this will be shown to be equivalent to

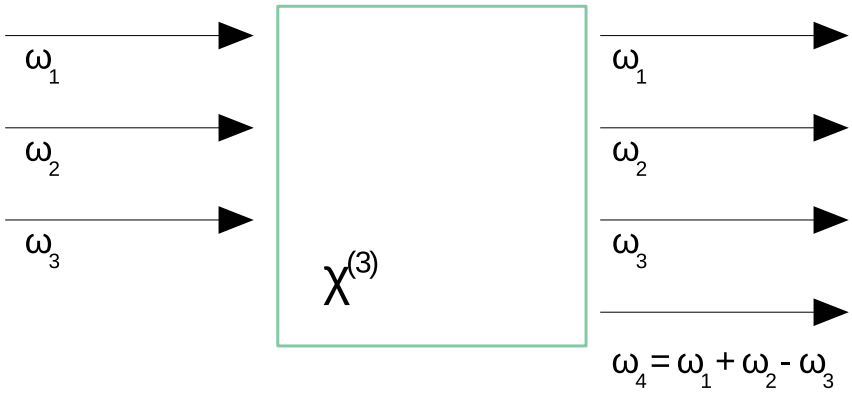

Figure 3: Schematic of four-wave mixing.

seeding at the optimal non-collinear angle, which will be a frequency-dependent angle derived in Chapter 2.

Next, we explore how to treat OPAs using quantum optics, the result of which will be a special case of the general quantum optical theory of KIA that is developed in Chapter 6

1.2 Discussion on quantum OPAs

We begin with OPAs based on second-order nonlinearity; specifically, a difference frequency generation process. A $\chi^{(2)}$ nonlinear medium is pumped by a strong wave of frequency ω_1, interacting with a signal wave of frequency ω_2. The difference frequency $\omega_3 = \omega_1 - \omega_2$ is generated, (see Fig. 2); for $\omega_3 \neq \omega_2$, we have non-degenerate parametric down conversion. That is, the pump photon is converted to a photon of frequency ω_2 and a photon with difference frequency $\omega_3 = \omega_1 - \omega_2$. The Hamiltonian for this process is described by [28]

$$\hat{H} = \hbar\omega_2\hat{a}^\dagger\hat{a} + \hbar\omega_3\hat{b}^\dagger\hat{b} + \hbar\omega_1\hat{c}^\dagger\hat{c} + i\hbar\Omega^{(2)}\left(\hat{a}\hat{b}\hat{c}^\dagger - \hat{a}^\dagger\hat{b}^\dagger\hat{c}\right), \tag{3}$$

where $\hbar$ is the reduced Planck's constant, $\Omega^{(2)}$ is a constant proportional to $\chi^{(2)}$, $\hat{a}$, $\hat{b}$, $\hat{c}$, and $\hat{a}^\dagger$, $\hat{b}^\dagger$, $\hat{c}^\dagger$ are the annihilation and creation operators for modes a (wave with frequency ω_2), b (wave with frequency ω_3), and c, the pump, respectively. To proceed, the parametric approximation is employed, where the pump is assumed to be a strong, coherent state; which treats the pump classically. As a result, we replace the pump mode operators by c-numbers, $\hat{c} \to \gamma e^{-i\omega_1 t}$ and $\hat{c}^\dagger \to \gamma^* e^{i\omega_1 t}$. Note that since we assume the pump to be a coherent state, the average number of photons in the pump is given by $< \hat{n}_c >= |\gamma|^2$. We make this approximation in Eq. (3) and after neglecting an irrelevant constant term in the

Hamiltonian, we obtain

$$\hat{H}_{PA} = \hbar\omega_2 \hat{a}^\dagger \hat{a} + \hbar\omega_3 \hat{b}^\dagger \hat{b} + i\hbar\Omega^{(2)} \left(\gamma^* e^{i\omega_p t} \hat{a}\hat{b} - \gamma e^{-i\omega_p t} \hat{a}^\dagger \hat{b}^\dagger \right). \tag{4}$$

Next, we move to the interaction picture by making the transformation $\hat{a}(t) = \hat{a}e^{-i\omega_2 t}$, and $\hat{b}(t) = \hat{b}e^{-i\omega_3 t}$. The interaction Hamiltonian becomes

$$\hat{H}_I = i\hbar\Omega^{(2)} \left(\gamma^* \hat{a}\hat{b} e^{i(\omega_1 - \omega_2 - \omega_3)t} - \gamma \hat{a}^\dagger \hat{b}^\dagger e^{-i(\omega_1 - \omega_2 - \omega_3)t} \right). \tag{5}$$

By enforcing $\omega_1 = \omega_2 + \omega_3$, we have non-degenerate parametric down conversion, and the Hamiltonian of Eq. (5) becomes time-independent,

$$\hat{H}_I = i\hbar\Omega^{(2)} \left(\gamma^* \hat{a}\hat{b} - \gamma \hat{a}^\dagger \hat{b}^\dagger \right). \tag{6}$$

The associated time-evolution operator of this Hamiltonian may be readily obtained as $\exp\left(-i\hat{H}_I t/\hbar\right)$. Alternatively, with the commutation relations, $\left[\hat{\mu},\, \hat{\nu}^\dagger\right] = \delta_{\mu,\nu}$, $[\hat{\mu},\, \hat{\nu}] = 0 = \left[\hat{\mu}^\dagger,\, \hat{\nu}^\dagger\right]$, for general modes μ and ν, the resulting Heisenberg equation of motion for mode a is found to be

$$\frac{d\hat{a}}{dt} = \frac{1}{i\hbar} \left[\hat{a},\, \hat{H}_I \right] = -\Omega^{(2)} \gamma \hat{b}^\dagger. \tag{7}$$

The solution of Eq. (7) is

$$\hat{a}(t) = \hat{a}(0) \cosh\left(|\gamma| \Omega^{(2)} t \right) + i e^{i\theta} \hat{b}^\dagger(0) \sinh\left(|\gamma| \Omega^{(2)} t \right), \tag{8}$$

where $e^{i\theta} = \gamma/|\gamma|$. The solution of Eq. (8) has been extensively studied and gives rise to, for example, 2-mode squeezed light [28].

An analogous parametric process occurs for $\chi^{(3)}$ nonlinear materials, which relates more to the work done in this thesis. In other words, instead of non-degenerate difference frequency generation, consider degenerate four-wave mixing, where two pump photons, $\omega_1 = \omega_2 = \omega_p$, are converted to a signal photon, $\omega_3 = \omega_s$, and an idler photon $\omega_4 = 2\omega_p - \omega_s = \omega_i$, see Fig. (3). Again, using the parametric approximation for the pump, transforming to the interaction picture, and enforcing the parametric process $2\omega_p = \omega_s + \omega_i$, we obtain

$$\hat{H}_I = i\hbar\Omega^{(3)} \left(\gamma^{*2} \hat{a}\hat{b} - \gamma^2 \hat{a}^\dagger \hat{b}^\dagger \right), \tag{9}$$

Comparing to Eq. (6), we see they are equivalent with the replacement $\Omega^{(2)}\gamma \to \Omega^{(3)}\gamma^2$. Therefore, the analogous solution for the evolution of the annihilation operator for mode a is easily obtained,

$$\hat{a}(t) = \hat{a}(0) \cosh\left(|\gamma|^2 \Omega^{(3)} t \right) + i e^{i\theta} \hat{b}^\dagger(0) \sinh\left(|\gamma|^2 \Omega^{(3)} t \right). \tag{10}$$

Eq. (10) is derived because it will be shown to be a special case of the more general solution arising from the quantum optical theory of KIA developed in Chapter 6. Now that OPA theory has been introduced, we return to KIA theory and outline the work done in the following chapters.

1.3 Outline of this work

We return to the more general perspective of KIA, described schematically as a type of degenerate four wave mixing process in Fig. 4.

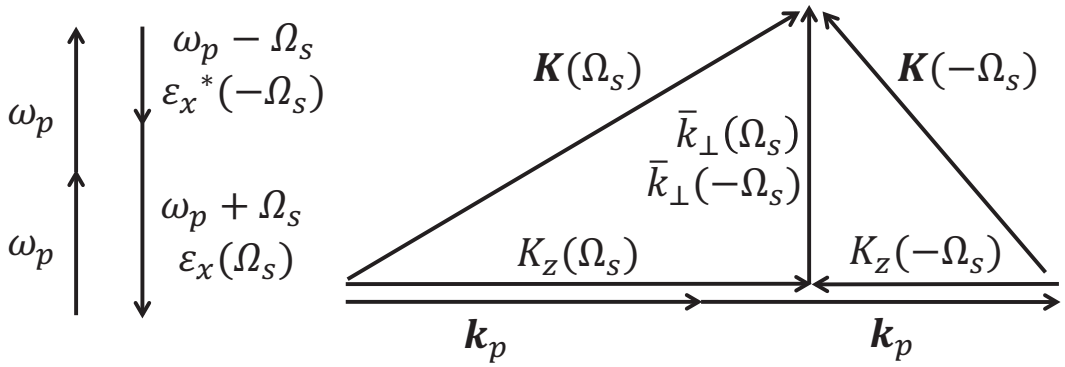

Figure 4: Schematic of KIA. Left: parametric four wave mixing of the type $2\omega_p - (\omega_p \pm \Omega_s) = \omega_p \mp \Omega_s$ where ω_p is the pump frequency and $-\omega_p < \Omega_s < \omega_p$ is the seed frequency. Right: transverse wavevectors exist for which unstable behavior occurs. All parameters shown will be described in the chapter. Gain is maximum for the transverse wavevector $\bar{k}_\perp(\Omega_s)$, see Eq. (55). The instability evolves as $\varepsilon_x(\Omega_s) = \exp\left[i(\omega_p + \Omega_s)t - i\mathbf{K}(\Omega_s)\cdot\mathbf{x}\right]$ and $\varepsilon_x^*(-\Omega_s) = \exp\left[-i(\omega_p - \Omega_s)t + i\mathbf{K}(-\Omega_s)\cdot\mathbf{x}\right]$. Here, $\mathbf{K}(\Omega_s) = (0, \bar{k}_\perp(\Omega_s), K_z(\Omega_s))$, see Eq. (70).

Note the the terminology used to describe the process is slightly different from typical four wave mixing theory, and lends to a more general approach seen in the next chapter, but the underlying physics is the same. In a Kerr nonlinear material parametric four wave mixing processes of the type $\omega_p + \omega_p - (\omega_p \pm \Omega_s) = \omega_p \mp \Omega_s$ occur. Two photons of the pump frequency, ω_p, are converted into fields $\varepsilon_x(\Omega_s)$ and $\varepsilon_x^*(-\Omega_s)$ with photon energies shifted to the red and blue side of ω_p by $\Omega_s = \omega_s - \omega_p$. Interference between the red and blue side of the pulse produces instability. For a wide range of seed frequencies in the interval $-\omega_p < \Omega_s < \omega_p$ there exist transverse wavevectors $k_\perp$ for which exponential growth occurs. The transverse wavevector for maximum amplification, $\bar{k}_\perp(\Omega_s)$, (see Eq. (55)) is finite, so interaction and hence emission with respect to the pump pulse should be noncollinear for optimal amplification. Phase matching and momentum conservation are

automatically fulfilled at maximum gain, since the instability wavevector, $\mathbf{K}(\Omega_s)$, fulfills the relation $\mathbf{K}(\Omega_s) = 2\mathbf{k}_p + \mathbf{K}(-\Omega_s)$, see Fig. 4.

Theoretical and experimental analyses have shown that the Kerr instability has promising properties as an amplification mechanism of ultrashort infrared pulses. The amplification bandwidth extends over a wide frequency range between the second harmonic of the pump pulse and the mid-infrared wavelength regime. Experimentally, amplification of more than a factor of 1000 was demonstrated in an Yttrium aluminium garnet (YAG) crystal, with a pump frequency of 800 nm and a seed frequency ranging from 600 nm to 2 μm [20]. This experiment has shown promising features of this amplification technique. As discussed in chapter 4, theoretically, it is predicted that by optimizing pump wavelength and material, amplification of mid-infrared one- to two-cycle pulses up to sub-mJ energies is possible.

The outline for this work is as follows: in the next chapter, the full vectorial perturbation equations beginning from Maxwell's equations for a Kerr nonlinear medium are developed, and the resulting equations of motion are solved. A brief description of the optical properties of two Kerr nonlinear materials used for the quantitative analysis is given. Subsequently, it is proven that for such materials of interest, vectorial effects are negligible across the instability regime and the scalar theory gives an accurate account of KIA. Furthermore, unification of FWM, modulation instability, and filamentation instability is demonstrated by means of our general KIA theory.

Following this, in Chapter 3, we explore the theory of plane wave KIA. That is, we consider the seed to be a plane wave to be amplified. This is of course an idealization, as plane waves can only be approximately realized in reality. However, many of the key ideas of KIA can still be quantified using plane wave theory, together with the aforementioned two materials. Chapters 1−3 are based on a chapter in a book to be published [29].

As we are interested specifically in amplification of ultrashort pulses, the analysis must be extended to allow for finite seed pulses. In Chapter 4, we explore the effects of generalizing the seed beam to a finite pulse, specifically a Gaussian beam. Using the same two materials as above, the effect of a finite seed beam is quantitatively analyzed. Chapter 4 is based on the work done in [19].

The Kerr instability gain profile is Bessel-Gaussian to leading order in the transverse domain. Therefore, the efficiency of KIA should be improved for amplifying Bessel-Gauss seeds compared to Gaussian seeds. This is explored in chapter 5.

Finally, in Chapter 6, the quantum optical theory of KIA is developed.

2 Kerr Instability Amplification

2.1 Vectorial perturbation equations

In the following, the equations of motion of the vector Kerr instability are derived, and then solved by means of linear stability analysis. The wavevector solution we obtain exhibits an instability regime which will be explored.

As mentioned at the outset, the nonlinear polarization vector for an isotropic Kerr nonlinear medium is given by Eq. (2),

$$\mathbf{P}^{(3)} = \epsilon_0 \chi^{(3)} \left(\mathbf{E} \cdot \mathbf{E}\right) \mathbf{E}. \tag{11}$$

Here, we assume $\chi^{(3)}$ to be instantaneous and an effective scalar quantity. The finite response of the Kerr nonlinearity becomes important when part of $\chi^{(3)}$ comes from the Raman nonlinearity. In that case, the theory needs to be extended to account for the delayed Raman response. To avoid undue complexity here, we derive the vectorial theory without the Raman nonlinearity, which is a reasonable approximation as long as pump and seed wavelengths are far away from the material bandgap [31]. The pump electric field (plane wave) can be perturbed weakly to have the form

$$\mathbf{E} = \hat{\mathbf{x}} E_p e^{i\omega_p t - i k_p z} + \boldsymbol{\varepsilon} + \text{c.c.}, \tag{12}$$

where E_p, ω_p, and k_p are the pump electric field amplitude, angular frequency, and wavevector, respectively, and $\boldsymbol{\varepsilon} = (\varepsilon_x, \varepsilon_y, \varepsilon_z)$ is a weak perturbation, $|\boldsymbol{\varepsilon}| \ll E_p$. We assume a plane wave pump so that E_p is constant; k_p will be defined below. The goal is to perform a stability analysis on the pump beam, and to show that $\boldsymbol{\varepsilon}$ exhibits instability. Thus, controlled amplification is possible if the perturbation is taken to be a weak seed beam.
We insert Eq. (12) into Eq. (11) and linearize to order $\mathcal{O}(\boldsymbol{\varepsilon})$, and neglect higher harmonic terms to obtain

$$\begin{aligned}\mathbf{P}^{(3)} &= \epsilon_0 \chi^{(3)} \left(\hat{\mathbf{x}} E_p e^{i\omega_p t - i k_p z} + \boldsymbol{\varepsilon} + \text{c.c.}.\right)^3 \\ &\approx \frac{1}{3}\epsilon_0 n_n \left[3\hat{\mathbf{x}} E_p e^{i\omega_p t - i k_p z} + 2\boldsymbol{\varepsilon} + 4\hat{\mathbf{x}}\varepsilon_x + \left(\boldsymbol{\varepsilon}^* + 2\hat{\mathbf{x}}\varepsilon_x^*\right) e^{2i\omega_p t - 2 i k_p z}\right] + \text{c.c.},\end{aligned} \tag{13}$$

where $n_n = 3\chi^{(3)} E_p^2 = n_2 I_p$, n_2 is the nonlinear coefficient, typically in units of [cm^2/W] and $I_p = n_p E_p^2/(2Z_0)$ is the constant pump intensity, where n_p is the linear refractive index evaluated at frequency, ω_p, and Z_0 is the vacuum impedance, and * denotes the complex conjugate. We insert Eq. (13) into the general vectorial wave equation derived from Maxwell's equations

$$\left[\nabla^2 - \boldsymbol{\nabla}(\boldsymbol{\nabla}\cdot) - \frac{n^2 *}{c^2}\frac{\partial^2}{\partial t^2}\right] \mathbf{E} = \mu_0 \frac{\partial^2 \mathbf{P}^{(3)}}{\partial t^2}, \tag{14}$$

where $n^2 = 1 + \chi^{(1)}$ is the linear refractive index in the time domain (response function), $c = 1/\sqrt{\epsilon_0 \mu_0}$ is the vacuum speed of light, μ_0 is the vacuum permeability, and $*$ denotes convolution. After inserting Eq. (13), the wave equation for the pump field yields the wavevector solution

$$k_p = \frac{\omega_p}{c}\sqrt{n_p^2 + n_n}. \tag{15}$$

The remaining wave equation for the perturbation reads

$$\left[\nabla^2 - \boldsymbol{\nabla}(\boldsymbol{\nabla}\cdot) - \frac{n^2 *}{c^2}\frac{\partial^2}{\partial t^2}\right]\varepsilon = \frac{1}{3}\frac{n_n}{c^2}\frac{\partial^2}{\partial t^2}\left[2\boldsymbol{\varepsilon} + 4\hat{\mathbf{x}}\varepsilon_x + (\boldsymbol{\varepsilon}^* + 2\hat{\mathbf{x}}\varepsilon_x^*)\, e^{2i\omega_p t - 2ik_p z}\right]. \tag{16}$$

To proceed, we let $\boldsymbol{\varepsilon} = \mathbf{u}e^{i\omega_p t}$ and Fourier transform Eq. (16) over transverse coordinates and time, $(x, y, z, t) \to (k_x, k_y, z, \omega)$. The Fourier transform of the field is given by

$$\begin{aligned}\widetilde{\boldsymbol{\varepsilon}}(k_x, k_y, z, \omega) = \mathcal{F}[\boldsymbol{\varepsilon}] = \mathcal{F}[\mathbf{u}e^{i\omega_p t}] &= \frac{1}{(2\pi)^{3/2}}\int_{-\infty}^{\infty}\mathbf{u}e^{-i(\omega-\omega_p)t}e^{-ik_x x - ik_y y}dtdxdy \\ &= \widetilde{\mathbf{u}}(k_x, k_y, z, \Omega),\end{aligned} \tag{17}$$

where $\Omega = \omega - \omega_p$ is the frequency shift from ω_p. For the complex conjugate terms on the right-side of Eq. (16), we have

$$\widetilde{\mathbf{u}^*}(k_x, k_y, z, \Omega) = \widetilde{\mathbf{u}}^*(-k_x, -k_y, z, -\Omega) \equiv \widetilde{\mathbf{u}}^*_{(-)}, \tag{18}$$

which will be important when decoupling $\widetilde{\mathbf{u}}$ and $\widetilde{\mathbf{u}}^*_{(-)}$ below. Throughout the text the subscript $(-)$ means evaluated at $(-k_x, -k_y, z, -\Omega)$. Next, we turn our attention to taking the Fourier transform of the $\boldsymbol{\nabla}(\boldsymbol{\nabla}\cdot)$ operator in Eq. (16), which can be expressed as the symmetric matrix

$$\hat{G} = \begin{pmatrix} -k_x^2 & -k_x k_y & ik_x\frac{\partial}{\partial_z} \\ -k_x k_y & -k_y^2 & ik_y\frac{\partial}{\partial_z} \\ ik_x\frac{\partial}{\partial_z} & ik_y\frac{\partial}{\partial_z} & \frac{\partial^2}{\partial_z^2} \end{pmatrix}. \tag{19}$$

Using Eqs. (17)$-$(19) we obtain the vectorial wave equation in Fourier space

$$\left[\frac{\partial^2}{\partial z^2} - k_\perp^2 - \hat{G} + k_v^2\right]\widetilde{\mathbf{u}} = -\frac{1}{3}k_n^2\left[-4\left(\hat{\mathbf{y}}\widetilde{u}_y + \hat{\mathbf{z}}\widetilde{u}_z\right) + \left(\widetilde{\mathbf{u}}^*_{(-)} + 2\hat{\mathbf{x}}\widetilde{u}^*_{x(-)}\right)e^{-2ik_p z}\right], \tag{20}$$

where $k_\perp^2 = k_x^2 + k_y^2$, $k_v^2 = c^{-2}\omega^2\left[n^2(\omega) + 2n_n\right]$, and $k_n^2 = c^{-2}\omega^2 n_n$ have been defined. The $z-$equation of Eq. (20) can be used to eliminate the $\widetilde{u}_z-$dependence in the $x-$ and

$y-$equations. It is found to be approximately

$$k_z^2 \widetilde{u}_z \approx i \frac{\partial}{\partial_z} \left(k_x \widetilde{u}_x + k_y \widetilde{u}_y \right), \tag{21}$$

where $k_z^2 = k_v^2 - k_\perp^2$. The fact that $n_n/n^2 \ll 1$ was used in obtaining Eq. (21). This approximation is only questionable for metamaterials at frequencies for which $n \to 0$, which are not relevant for this work. The $\widetilde{u}_z-$dependence can now be eliminated in the other two equations of Eq. (20) to obtain the set of coupled equations for $\widetilde{u}_x$, $\widetilde{u}_y$ and their complex conjugates. We insert Eq. (21) into Eq. (20) and obtain

$$\left[1 + \frac{1}{k_z^2} \frac{\partial^2}{\partial_z^2}\right] \left[(k_v^2 - k_y^2)\widetilde{u}_x + k_x k_y \widetilde{u}_y\right] = -k_n^2 \widetilde{u}^*_{x(-)} e^{-2ik_p z} \tag{22a}$$

$$\left[1 + \frac{1}{k_z^2} \frac{\partial^2}{\partial_z^2}\right] \left[(k_v^2 - k_x^2)\widetilde{u}_y + k_x k_y \widetilde{u}_x\right] = -\frac{1}{3} k_n^2 \left[-4\widetilde{u}_y + \widetilde{u}^*_{y(-)} e^{-2ik_p z}\right], \tag{22b}$$

It is convenient to express Eqs. (22) as a 2×2-matrix equation for the transversely-polarized vector $\widetilde{\mathbf{u}}_\perp = (\widetilde{u}_x, \widetilde{u}_y)$ as

$$\hat{A} \left(\frac{\partial^2}{\partial_z^2} + k_z^2\right) \widetilde{\mathbf{u}}_\perp = -k_n^2 k_z^2 \begin{pmatrix} \widetilde{u}^*_{x(-)} \\ \frac{1}{3}\widetilde{u}^*_{y(-)} \end{pmatrix} e^{-2ik_p z}, \tag{23}$$

where

$$\hat{A} \equiv \begin{pmatrix} k_v^2 - k_y^2 & k_x k_y \\ k_x k_y & k_v^2 - k_x^2 \end{pmatrix}. \tag{24}$$

We have neglected the first term on the right side of Eq. (22b). This approximation is justified since $k_n^2 \ll k_v^2$. As a result, the analysis is much simpler by increasing symmetry between the transversely-polarized fields. By multiplying Eq. (23) on the left by $\hat{A}^{-1} = \mathrm{adj}(\hat{A})/\det(\hat{A})$ we obtain

$$\left(\frac{\partial^2}{\partial_z^2} + k_z^2\right) \widetilde{\mathbf{u}} = -\frac{k_n^2}{k_v^2} \hat{M} \widetilde{\mathbf{u}}^*_{\perp(-)} e^{-2ik_p z}, \tag{25}$$

where

$$\hat{M} \equiv \begin{pmatrix} k_v^2 - k_x^2 & -\frac{1}{3}k_x k_y \\ -k_x k_y & \frac{1}{3}(k_v^2 - k_y^2) \end{pmatrix}. \tag{26}$$

We eliminate the exponential terms on the right-side of Eq. (25) by making the transforma-

tion $\widetilde{\mathbf{u}}_\perp = \widetilde{\mathbf{v}}_\perp e^{-ik_p z}$, with the result

$$\left[\left(\frac{\partial}{\partial_z} - ik_p\right)^2 + k_z^2\right]\widetilde{\mathbf{v}}_\perp = -\frac{k_n^2}{k_v^2}\hat{M}\widetilde{\mathbf{v}}^*_{\perp(-)}. \tag{27}$$

At this point, we obtain an equation for $\widetilde{\mathbf{v}}^*_{\perp(-)}$ by taking the complex conjugate of Eq. (27) and by the replacement $\Omega \to -\Omega$. The resulting equation reads

$$\left[\left(\frac{\partial}{\partial_z} + ik_p\right)^2 + k_{z(-)}^2\right]\widetilde{\mathbf{v}}^*_{\perp(-)} = -\frac{k_{n(-)}^2}{k_{v(-)}^2}\hat{M}_{(-)}\widetilde{\mathbf{v}}_\perp. \tag{28}$$

By using Eq. (27) in Eq. (28) we obtain

$$\left[\left(\frac{\partial}{\partial_z} - ik_p\right)^2 + k_z^2\right]\left[\left(\frac{\partial}{\partial_z} + ik_p\right)^2 + k_{z(-)}^2\right]\widetilde{\mathbf{v}}_\perp = \frac{k_n^2 k_{n(-)}^2}{k_v^2 k_{v(-)}^2}\hat{L}\widetilde{\mathbf{v}}_\perp, \tag{29}$$

where $\hat{L} \equiv \hat{M}\hat{M}_{(-)}$. Explicitly, $\hat{L}$ is written as

$$\begin{aligned}\hat{L} &= \begin{pmatrix} (k_v^2 - k_x^2)(k_{v(-)}^2 - k_x^2) + \frac{1}{3}k_x^2 k_y^2 & -\frac{1}{9}k_x k_y\left(3k_v^2 + k_{v(-)}^2 - 3k_x^2 - k_y^2\right) \\ -\frac{1}{3}k_x k_y\left(3k_{v(-)}^2 + k_v^2 - 3k_x^2 - k_y^2\right) & \frac{1}{9}(k_v^2 - k_x^2)(k_{v(-)}^2 - k_x^2) + \frac{1}{3}k_x^2 k_y^2 \end{pmatrix} \\ &\equiv \begin{pmatrix} l_{11} & l_{12} \\ l_{21} & l_{22} \end{pmatrix}. \end{aligned} \tag{30}$$

Eq. (29) is formally solved by diagonalizing $\hat{L}$ since the matrix elements contain wavevectors only and are independent of z. Thus, we make the transformation

$$\widetilde{\mathbf{v}}_\perp = \hat{U}\widetilde{\mathbf{w}}_\perp, \tag{31}$$

where $\hat{U}$ is a unitary matrix that shifts the coordinate axes such that $\hat{U}^{-1}\hat{L}\hat{U} = \hat{D}$ is a diagonal matrix with non-zero elements, given by the eigenvalues of $\hat{L}$. With this transformation, Eq. (29) becomes

$$\left[\left(\frac{\partial}{\partial_z} - ik_p\right)^2 + k_z^2\right]\left[\left(\frac{\partial}{\partial_z} + ik_p\right)^2 + k_{z(-)}^2\right]\widetilde{\mathbf{w}}_\perp = \frac{k_n^2 k_{n(-)}^2}{k_v^2 k_{v(-)}^2}\hat{D}\widetilde{\mathbf{w}}_\perp. \tag{32}$$

The solution of Eq. (32) will be in the form of plane waves

$$\widetilde{\mathbf{w}}_\perp(z) = \begin{pmatrix} e^{iK_x z} & 0 \\ 0 & e^{iK_y z} \end{pmatrix}\widetilde{\mathbf{w}}_\perp(0) \equiv e^{i\hat{K}z}\widetilde{\mathbf{w}}_\perp(0), \tag{33}$$

where K_x and K_y are the complex wavevectors for $\widetilde{w}_x$ and $\widetilde{w}_y$, respectively, and $\widetilde{\mathbf{w}}_\perp(0)$

denotes the initial condition of the field $\widetilde{\mathbf{w}}_\perp(z)$ at $z=0$. Notice from Eq. (31) that

$$\widetilde{\mathbf{w}}_\perp(0) = \hat{U}^{-1}\widetilde{\mathbf{v}}_\perp(0). \tag{34}$$

Thus, by means of Eqs. (31), (33) and (34) we have the formal solution

$$\widetilde{\mathbf{v}}_\perp(z) = \hat{U}e^{i\hat{K}z}\hat{U}^{-1}\widetilde{\mathbf{v}}_\perp(0) \equiv \hat{P}(z)\widetilde{\mathbf{v}}_\perp(0), \tag{35}$$

where $\hat{P}(z)$ is the $z-$dependent evolution matrix that propagates $\widetilde{\mathbf{v}}_\perp$ from its initial state at $z=0$ to z. The procedure for the solution of Eq. (29) is given by Eqs. (30)$-$(35). In order to proceed, the eigenvalues, $\lambda_{x,y}$, of $\hat{L}$ must be found. These will be used to obtain $\hat{D}$, and the eigenvectors will yield $\hat{U}$. We set

$$\det\left(\hat{L} - \lambda_{x,y}\hat{I}\right) = 0, \tag{36}$$

where $\hat{I}$ is the identity matrix. From Eq. (30) we see that the off-diagonal elements, $l_{12,21}$, are much weaker than the diagonal elements, $l_{11,22}$. To order $\mathcal{O}(l_{12}l_{21})$ we obtain

$$\lambda_x = l_{11} + \frac{l_{12}l_{21}}{l_{11}-l_{22}} \tag{37a}$$

$$\lambda_y = l_{22} - \frac{l_{12}l_{21}}{l_{11}-l_{22}}. \tag{37b}$$

By means of Eqs. (37), we obtain the matrices $\hat{D}$, $\hat{U}$, and $\hat{U}^{-1}$ as

$$\hat{D} = \begin{pmatrix} l_{11} + \frac{l_{12}l_{21}}{l_{11}-l_{22}} & 0 \\ 0 & l_{22} - \frac{l_{12}l_{21}}{l_{11}-l_{22}} \end{pmatrix} \tag{38a}$$

$$\hat{U} = \frac{1}{l_{11}-l_{22}}\begin{pmatrix} l_{11}-l_{22} & -l_{12} \\ l_{21} & l_{11}-l_{22} \end{pmatrix} \tag{38b}$$

$$\hat{U}^{-1} = \frac{1}{l_{11}-l_{22}}\begin{pmatrix} l_{11}-l_{22} & l_{12} \\ -l_{21} & l_{11}-l_{22} \end{pmatrix} \tag{38c}$$

Using Eqs. (38) in Eq. (35), we find the propagator matrix to be

$$\hat{P}(z) = \begin{pmatrix} e^{iK_xz} + \frac{l_{12}l_{21}}{(l_{11}-l_{22})^2}e^{iK_yz} & \frac{l_{12}}{l_{11}-l_{22}}\left(e^{iK_xz} - e^{iK_yz}\right) \\ \frac{l_{21}}{l_{11}-l_{22}}\left(e^{iK_xz} - e^{iK_yz}\right) & e^{iK_yz} + \frac{l_{12}l_{21}}{(l_{11}-l_{22})^2}e^{iK_xz} \end{pmatrix}. \tag{39}$$

The progagator $\hat{P}$ together with Eqs. (32) and (35) governs the evolution of the instability.

2.2 Solution of the equations of motion of the vector Kerr instability

To complete the solution, we must solve the differential equation (32). We do this by means of the ansatz of Eq. (33) to obtain wavevectors of the plane wave equation. The resulting equations are quartic in the complex wavevectors $K_{x,y}$ and depend on the reduced eigenvalues $\Lambda_{x,y} \equiv \lambda_{x,y}/k_v^2 k_{v(-)}^2$

$$\left[(K_{x,y} - k_p)^2 + k_z^2\right]\left[(K_{x,y} + k_p)^2 + k_{z(-)}^2\right] = \Lambda_{x,y} k_n^2 k_{n(-)}^2. \tag{40}$$

To make progress, the sign flipped functions $k_{z(-)}$, $k_{v(-)}$, and $k_{n(-)}$ need to be determined. To this end, these functions are split into even components which remain unchanged and odd components which change sign when $\Omega \to -\Omega$. First, we write the general linear refractive index, $\eta(\omega) = \sqrt{n^2(\omega) + 2n_n}$ as

$$\begin{aligned}\eta(\omega) &= \eta_p + \Delta\eta(\Omega) \\ &= \eta_p + \eta_g(\Omega) + \eta_u(\Omega),\end{aligned} \tag{41}$$

where $\eta_p = \eta(\omega_p)$, and

$$\eta_g(\Omega) = \frac{1}{2}\left[\Delta\eta(\Omega) + \Delta\eta(-\Omega)\right] \tag{42a}$$

$$\eta_u(\Omega) = \frac{1}{2}\left[\Delta\eta(\Omega) - \Delta\eta(-\Omega)\right], \tag{42b}$$

are the even and odd functions, respectively, such that $\eta_g(-\Omega) = \eta_g(\Omega)$, and $\eta_u(-\Omega) = -\eta_u(\Omega)$. With these definitions, we are equipped to write similar splitting for k_v,

$$k_v = k_v(\omega_p) + D_u(\Omega) + D_g(\Omega), \tag{43}$$

where

$$D_u(\Omega) = \frac{1}{c}\left[\eta_p\Omega + \eta_g(\Omega)\Omega + \eta_u(\Omega)\omega_p\right] \tag{44a}$$

$$D_g(\Omega) = \frac{1}{c}\left[\eta_g(\Omega)\omega_p + \eta_u(\Omega)\Omega\right], \tag{44b}$$

where $D_u(\Omega)$ and $D_g(\Omega)$ are odd and even dispersion functions, respectively, such that $D_u(-\Omega) = -D_u(\Omega)$ and $D_g(-\Omega) = D_g(\Omega)$. Note that these functions are exact and no approximations, such as a Taylor expansion, have been made made. Even when summed to all orders, a Taylor expansion need not necessarily converge. This is particularly the case for far infrared frequencies $\omega = \omega_p + \Omega$ with $\Omega \approx< \omega_p$. In the limit of small detuning, where $\Omega \ll \omega_p$, and since $n^2 \gg 2n_n$, $\eta_u \approx n_p'\Omega$ and $\eta_g \approx n_p''\Omega^2/2$. Here, the primes on n_p denote differentiation of $n(\omega)$ with respect to ω evaluated at ω_p. Thus, to lowest order we obtain

for Eqs. (44), $D_u \approx \beta_1 \Omega$ and $D_g \approx \beta_2 \Omega^2/2$, where $\beta_1 = [dk/d\omega](\omega_p) = (n_p + n_p' \omega_p)/c$ and $\beta_2 = [d^2k/d\omega^2](\omega_p) = (2n_p' + n_p'' \omega_p)/c$ are the group velocity, and group velocity dispersion terms, respectively.

Finally, the sign-flipped functions are determined as

$$k_{v(-)} = k_v(\omega_p) - D_u(\Omega) + D_g(\Omega), \tag{45}$$

and, treating n_n as constant,

$$k_{n(-)}^2 = \frac{n_n}{c}(\omega_p - \Omega)^2. \tag{46}$$

Now, we can readily use Eqs. (43) and (45) in (40) to obtain

$$\left(K_{x,y}^2 - \sigma^2 D_u^2 + k_\perp^2 - \kappa_\perp^2\right)^2 - 4k_p^2 \left(K_{x,y} + \sigma D_u\right)^2 - \Lambda_{x,y} k_n^2 k_{n(-)}^2 = 0, \tag{47}$$

where we have defined

$$\kappa_\perp^2 = \left(k_p^2 - D_u^2\right)\left(\sigma^2 - 1\right), \tag{48}$$

and

$$\sigma = \frac{k_v(\omega_p) + D_g}{k_p}. \tag{49}$$

The dominant solution for $K_{x,y}$ is given by the second term of Eq. (47), $K_{x,y} \approx -\sigma D_u$, which was verified numerically, see appendix A. With this approximation we can then use

$$\left(K_{x,y}^2 - \sigma^2 D_u^2\right) \approx -2\sigma D_u \left(K_{x,y} + \sigma D_u\right). \tag{50}$$

in Eq. (47). Using this approximation significantly simplifies the equations by reducing them to quadratic equations for $K_{x,y}$

$$\left(k_p^2 - \sigma^2 D_u^2\right)\left(K_{x,y} - \sigma D_u\right)^2 - \sigma D_u \Delta k_\perp^2 \left(K_{x,y} - \sigma D_u\right) - \Delta k_\perp^4 = -\Lambda_{x,y} k_n^2 k_{n(-)}^2, \tag{51}$$

where $\Delta k_\perp^2 = \kappa_\perp^2 - k_\perp^2$ has been used to be concise. Note that when $k_p^2 = \sigma^2 D_u^2$, which occurs at $\omega \approx 2\omega_p$ and $\omega \approx 0$, Eq. (51) reduces to a linear equation which exhibits no unstable solutions. As we are seeking such unstable solutions, we assume $k_p^2 \neq \sigma^2 D_u^2$ and must avoid frequencies that are double that of the pump and higher. As we are interested in frequencies on the red side of the pump in the near- to mid-infrared regime, it poses no issue for the purposes of this work, provided the pump frequency is chosen appropriately relative to ω such that $\omega \approx 0$ is not realized. In section 3.2, this will become clear when two example materials are discussed.

Eq. (51) exhibits the solutions $K_{x,y} = K_u(\Omega) \pm K_g(\Omega; \Lambda_{x,y})$

$$K_u(\Omega) = -\sigma D_u \left(1 - \frac{1}{2}\frac{\Delta k_\perp^2}{k_p^2 - \sigma^2 D_u^2}\right) \tag{52a}$$

$$K_g(\Omega; \Lambda_{x,y}) = \frac{1}{2}\frac{k_p\sqrt{\Delta k_\perp^4 - \Lambda_{x,y}\delta_\perp^4}}{k_p^2 - \sigma^2 D_u^2}, \tag{52b}$$

where we have defined

$$\delta_\perp^2 = \frac{k_n k_{n(-)}}{k_p}\sqrt{k_p^2 - \sigma^2 D_u^2}, \tag{53}$$

which is a transverse width whose significance will be seen below. The wavevector solution exhibits instability when the argument under the square root in $K_g(\Omega; \Lambda_{x,y})$ becomes negative. As a result, exponential growth is possible with intensity gain

$$g(\Omega; \Lambda_{x,y}) = -2\mathrm{Im}\left[K_g(\Omega; \Lambda_{x,y})\right]. \tag{54}$$

Now that the full wavevector solutions for $K_{x,y}$ have been obtained, the propagator, $\hat{P}(z)$ given by Eq. (39) can be specified. The propagator describes how $\widetilde{\mathbf{v}}_\perp(z)$ evolves from its arbitrary initial state of $\widetilde{\mathbf{v}}_\perp(0)$, given by Eq. (35). The difference between scalar instability theory and the vectorial instability theory here lies within the transverse asymmetries of $\Lambda_{x,y}$ contained in $K_{x,y}$ and $\hat{P}(z)$, which couples the $x-$ and $y-$polarizations of the initial fields. We can ignore the K_y solution since to leading order $\Lambda_x \approx 9\Lambda_y$, which renders $g(\Omega; \Lambda_y)$ negligible compared to $g(\Omega; \Lambda_x)$. We consider, then, only the gain $g(\Omega; \Lambda_x) \equiv g(\Omega)$. From Eq. (52b), it is clear that the gain is maximized for the transverse wavevector $k_\perp = \bar{k}_\perp(\Omega)$

$$\bar{k}_\perp(\Omega) = \begin{cases} \kappa_\perp(\Omega) & \text{if} \quad \kappa_\perp^2 \geq 0 \\ 0 & \text{if} \quad \kappa_\perp^2 < 0 \end{cases} \tag{55}$$

From Eq. (48) we see that $\kappa_\perp^2 \propto \sigma^2 - 1 \approx 2(\eta_g + \eta_u\Omega/\omega_p)/n_p$. Thus, depending on the material and the pump wavelength, η_g and $\eta_u\Omega/\omega_p$ may have equal or opposite signs. As a result, $\kappa_\perp^2 < 0$ is possible, which terminates the instability regime, which is why $\bar{k}_\perp$ must be piece-wise defined. In line with this, the maximum gain $g(\Omega, k_\perp = \bar{k}_\perp(\Omega)) = \bar{g}(\Omega)$ is written as

$$\bar{g}(\Omega) = \begin{cases} k_p\frac{\left[(1+r_0)\delta_\perp^4 - (\kappa_\perp^2 - \bar{k}_\perp^2)^2\right]^{1/2}}{k_p^2 - \sigma^2 D_u^2} & \text{otherwise} \\ 0 & \text{if} \quad \kappa_\perp^2 < 0, \quad \kappa_\perp^4 > \delta_\perp^4(1 + r_0), \end{cases} \tag{56}$$

where $r_0 \approx \Lambda_x - 1$; r_0 is the leading-order asymmetry term arising from the vectorial nature

of KIA. Since $g(k_\perp^2 = \bar{k}_\perp^2 \pm \sqrt{1+r_0}\delta_\perp^2) = 0$, the (squared) transverse wavevector half-width over which instability gain occurs as a function of Ω is given by $\sqrt{1+r_0}\delta_\perp^2(\Omega)$, see Eq. (53). The spatio-spectral coupling given by $k_\perp^2 = \bar{k}_\perp^2 \pm \sqrt{1+r_0}\delta_\perp^2(\Omega)$ defines the range of frequencies over which the instability exists. Note that r_0 weakly disrupts the transverse symmetry, where otherwise this relation would be completely transversally symmetric.

Note that even if r_0 were non-negligible, it is always possible to eliminate the transverse asymmetry by seeding along the line $\mathbf{k}_\perp = (k_x = 0, k_y)$ such that $r_0 = 0$ automatically. In essence, vectorial effects reduce the noncollinear interaction from being conically symmetric to symmetric along the line $k_x = 0$ only. Before proceeding with a more quantitiative analysis using real example bulk dielectrics and their optical properties, it will be shown that the wavevector solution obtained in Eq. (52) is a generalization to both temporal and spatial Kerr instability processes.

2.3 Limiting cases of the wavevector solution

In the following we demonstrate that the solution of Eq. (52) is a generalization to both modulation instability (temporal) [6] and filamentation instability (spatial) [5] in appropriate limits. First, we neglect vectorial effects by letting $\Lambda_{x,y} = 1$ and $K_{x,y} \to K$. Then, in the limits of $\mathbf{k}_\perp = 0$ and $\Omega = 0$, Eq. (52) reduces to modulation instability, and filamentation instability, respectively. For $\Omega/\omega_p \ll 1$ and $n_n \ll 1$ we can approximate $D_u \approx \beta_1\Omega$, $D_g \approx \beta_2\Omega^2/2$, $\sigma \approx 1$, $k_p^2 - (\sigma D_u)^2 \approx k_p^2$, $\delta_\perp^2 \approx k_n^2(\omega_p)$. By using the approximation below Eq. (55) we find $\sigma^2 - 1 \approx (k_n(\omega_p)/k_p)^2 + 2D_g/k_p$ and obtain

$$g \approx \sqrt{\left(\frac{k_n^2(\omega_p)}{k_p}\right)^2 - \left(\frac{k_n^2(\omega_p)}{k_p} + \beta_2\Omega^2 - \frac{k_\perp^2}{k_p}\right)^2}. \tag{57}$$

By setting $\Omega = 0$ in Eq. (57), a relation for the filamentation instability is obtained in agreement with [5], namely

$$g \approx \frac{1}{k_p}\sqrt{k_n^2(\omega_p)^2 - (k_n^2(\omega_p) - k_\perp^2)^2}. \tag{58}$$

Next, by setting $k_\perp = 0$ in Eq. (57) and by introducing the fiber nonlinear coefficient $\gamma = n_2\omega_p/(2n_pcA_{\text{eff}})$ we can express the nonlinear term as $k_n^2(\omega_p)/k_p = 2\gamma P_p$. Here $I_p = P_p/A_{\text{eff}}$, A_{eff} is the effective fiber pulse area, and P_p the pump peak power. The equation resulting from Eq. (57) agrees with the gain for modulation instability in fibers [6],

$$g \approx \sqrt{(\beta_2\Omega^2)^2 + 4\gamma P_p\beta_2\Omega^2}. \tag{59}$$

Finally, note that we have defined the total refractive index, $(n_p^2 + n_n)^{1/2}$, differently to Ref. [6], where $n_p + n_n$ is used; as a result $2\gamma n_p$ corresponds to γ defined in Ref. [6].

In order to explore the general solution of Eq. (52) further, an example of a real bulk

dielectric that one might use in a KIA experiment, with all its optical properties, must be considered. First, we define the optical properties of the two example materials chosen for the rest of the analysis that follows. Then, using one of the materials, we show that vectorial effects are negligible over the whole instability regime, justifying the use of the scalar theory for the subsequent analysis.

2.4 Optical properties of CaF_2 and KBr

The materials of interest in this work are bulk dielectric crystals, transparent into the infrared, have relatively small linear index and flat dispersion compared to their nonlinear index, and a high as possible damage threshold. These properties will be discussed more in Chapter 3. The materials chosen are two dielectric bulk crystals, calcium fluoride (CaF_2), and potassium bromide (KBr). Two different pump wavelengths $\lambda_p = 0.85, 2.1\,\mu$m are chosen in each case. The CaF_2 and KBr crystals have transmission windows from $0.3 - 8\,\mu$m and $0.25 - 25\,\mu$m, respectively [32]. In all figures, the linear and nonlinear indices for CaF_2 are given by Ref. [33], and $n_2 = 2\times10^{-16}$ cm^2/W [34], respectively. The linear and nonlinear indices for KBr are given by Ref. [35], and $n_2 = 6\times10^{-16}$ cm^2/W [36], respectively. Finally, the peak pump intensities used are $I_p = 50$ TW/cm^2 and $I_p = 8$ TW/cm^2 for CaF_2 and KBr, respectively. These intensities are chosen carefully and are valid for the damage threshold of each material in question, see Chapter 4 for more detail. Next, the role of vectorial effects on KIA is discussed in CaF_2.

2.5 Vectorial effects in KIA

Here, it is demonstrated that vectorial effects are negligible in the regime where instability gain is possible in materials of interest for us. The material chosen here is CaF_2. KBr exhibits the exact same qualitative features of vectorial effects as in CaF_2. Vectorial effects are negligible as long as $1 + r_0 = \Lambda_x \approx 1$. This approximation is valid as long as the leading order asymmetric term from Eq. (37a), $\Lambda_x \approx l_{11}/k_v^2 k_{v(-)}^2$, is small, namely if

$$|r_0| = \left| \frac{k_x^2 \left(k_v^2 + k_{v(-)}^2 \right)}{k_v^2 k_{v(-)}^2} \right| \ll 1. \tag{60}$$

This condition is valid for most materials, as the instability regime will have ceased before the transverse asymmetry significantly affects the instability gain, see Fig. 5. Clearly, the frequencies at which maximum gain occurs is far away from where $|r_0|$ is significant compared to unity (see the dashed white line), even for maximized asymmetry, where $k_\perp = k_x$. Therefore, even if the asymmetry is as prominent as possible, the instability regime ceases before vectorial effects alter the scalar theory. Next, we discuss in detail the relationship between KIA and four-wave mixing (FWM) using scalar theory for simplicity and clarity.

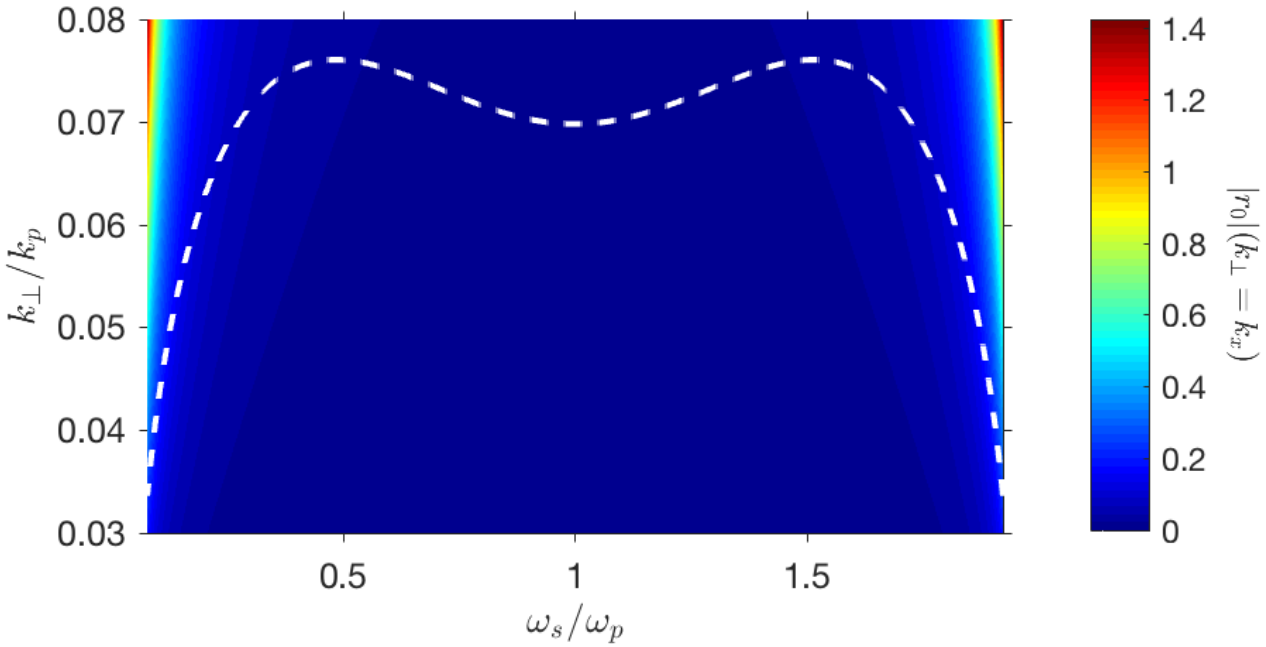

Figure 5: The asymmetric vectorial term, $|r_0|$ (see Eq. (60)), is plotted in CaF_2 with peak pump intensity $I_p = 50$ TW/cm^2. For other parameters used, see section 3.2. We plot along the line $k_y = 0$ where the vectorial asymmetry is maximized at $k_\perp = k_x$. The dashed white line indicates $\bar{k}_\perp$ at which maximum gain $\bar{g} = g(\bar{k}_\perp)$ occurs, see Eq. (56).

2.6 Unification of KIA and FWM

The goal of this section is to show that KIA and FWM are mathematically equivalent and are thus two representations of the same physical process. The KIA approach is more general, as it does not rely on splitting the electric field of the instability into carrier and envelope. As a result, it yields a general expression for the FWM gain over the whole spectral and transverse wavevector range. This gain can be applied to any beam form, such as non-collinear Gaussian beams or Bessel-Gaussian beams, for the wave equations developed do not assume any form for the perturbation. The theory of FWM emerges from the theory of KIA by splitting the electric field into envelope and carrier. Once this is done, in order to proceed, certain approximations are made, such as the paraxial approximation and a Taylor expansion of the wavevector in a sum over dispersive terms.

To obtain the scalar wave equations of KIA, we take Eq. (27), and let the matrix, $\hat{M}$, given by Eq. (26) tend to the scalar value $\hat{M} \to k_n^2/k_v^2$, and the perturbation field vector tend to the scalar $\widetilde{\mathbf{v}}_\perp \to \widetilde{v}_x$. As well, we conjugate the resulting equation and obtain the set of scalar wave equations for the perturbation field and its conjugate as

$$\left[\left(\frac{\partial}{\partial_z} - ik_p\right)^2 + k_z^2\right]\widetilde{v}_x = -k_n^2\widetilde{v}^*_{x(-)} \tag{61a}$$

$$\left[\left(\frac{\partial}{\partial_z} + ik_p\right)^2 + k_{z(-)}^2\right]\widetilde{v}^*_{x(-)} = -k_{n(-)}^2\widetilde{v}_x. \tag{61b}$$

The purpose of this section is to prove that the wave equations derived for FWM are equivalent to Eqns. (61) in the appropriate generalization. We start with the FWM ansatz for the electric field as

$$E = E_p e^{i\omega_p t - ik_p z} + E_s(\mathbf{x}, t)e^{i\omega_s t} + E_i(\mathbf{x}, t)e^{i\omega_i t} + \text{c.c.}, \tag{62}$$

where subscripts p, s, i, stand for the strong plane wave pump, weak signal, and weak idler beams, respectively. Notice we keep E_s and E_i as general functions, consistent with ε in KIA theory; no signal and idler center wavevectors have been introduced. We insert Eq. (62) into the third order nonlinear polarization function (Eq. (11) in the scalar limit), to obtain

$$\begin{aligned} P^{(3)} \approx \frac{n_n}{\mu_0 c^2}\left[E_p e^{i\omega_p t - ik_p z} + 2\left(E_s e^{i\omega_s t} + E_i e^{i\omega_i t}\right) + e^{2i\omega_p t - 2ik_p z}\left(E_s^* e^{-i\omega_s t} + E_i^* e^{-i\omega_i t}\right)\right] \\ + \text{c.c.}, \end{aligned} \tag{63}$$

where we have neglected third harmonic generation and assume $E_p \gg E_{s,i}(z = 0)$. We insert Eq. (63) into the scalar version of the nonlinear wave equation, Eq. (14),

$$\left[\nabla^2 - \frac{\partial^2}{\partial t^2}\frac{n^2*}{c^2}\right]E = \mu_0\frac{\partial^2 P^{(3)}}{\partial t^2}; \tag{64}$$

the first term on the right side of Eq. (63) results in the wavevector solution $k_p = c^{-1}\omega_p\sqrt{n_p^2 + n_n}$ as in KIA theory.

For the remaining terms on the right side of Eq. (63), we take the Fourier transform of Eq. (64) of the coordinates (x, y, t) to obtain the coupled equations for the signal and idler fields

$$\left[\frac{\partial^2}{\partial_z^2} + k_z^2\right]\widetilde{E_s}(\omega - \omega_s) = -k_n^2\widetilde{E_i^*}(\omega - \omega_s)e^{-2ik_p z} \tag{65a}$$

$$\left[\frac{\partial^2}{\partial_z^2} + k_z^2\right]\widetilde{E_i}(\omega - \omega_i) = -k_n^2\widetilde{E_s^*}(\omega - \omega_i)e^{-2ik_p z}, \tag{65b}$$

where $k_z^2 = k_v^2 - k_\perp^2$ and $k_n^2 = c^{-2}\omega^2 n_n$ are defined as before (see below Eq. (20)). As FWM

is a parametric process, we have used the energy conservation relation $2\omega_p = \omega_s + \omega_i$ in Eq. (63), which couples the signal and idler fields with the corresponding conjugates. To proceed, we let $\widetilde{E_{s,i}}(\omega - \omega_{s,i}) = \widetilde{A_{s,i}}(\omega - \omega_{s,i})e^{-ik_p z}$ to eliminate the exponential factors of Eqs. (65a) and (65b). Further, $\widetilde{E^*_{s,i}}(\omega - \omega_{s,i}) = \widetilde{E_{s,i}}^*(\omega_{s,i} - \omega)$ is used. As well, $\omega - \omega_s = \omega - \omega_p - (\omega_s - \omega_p) \equiv \Omega - \Omega_s$, and $\omega - \omega_i = \omega - 2\omega_p + \omega_s = \Omega + \Omega_s$. Using the above, and taking the complex conjugate of Eq. (65b) and letting $\Omega \to -\Omega$ results in the coupled equations

$$\left[\left(\frac{\partial}{\partial_z} - ik_p\right)^2 + k_z^2\right]\widetilde{A_s}(\Omega - \Omega_s) = -k_n^2\widetilde{A_i}^*(\Omega_s - \Omega) \tag{66a}$$

$$\left[\left(\frac{\partial}{\partial_z} + ik_p\right)^2 + k_{z(-)}^2\right]\widetilde{A_i}^*(\Omega_s - \Omega) = -k_{n(-)}^2\widetilde{A_s}(\Omega - \Omega_s). \tag{66b}$$

If we let $\widetilde{A_s}(\Omega - \Omega_s) \to \widetilde{v}(\Omega)$ and $\widetilde{A_i}^*(\Omega_s - \Omega) \to \widetilde{v}^*(-\Omega)$, we obtain

$$\left[\left(\frac{\partial}{\partial_z} - ik_p\right)^2 + k_z^2\right]\widetilde{v}(\Omega) = -k_n^2\widetilde{v}^*(-\Omega) \tag{67a}$$

$$\left[\left(\frac{\partial}{\partial_z} + ik_p\right)^2 + k_{z(-)}^2\right]\widetilde{v}^*(-\Omega) = -k_{n(-)}^2\widetilde{v}(\Omega), \tag{67b}$$

which are precisely the coupled equations, Eqs. (61). Thus, it can be concluded that the derivation of FWM and KIA start from the same set of equations. Usually, in FWM theory the signal and idler wavevectors are explicitly introduced in the ansatz requiring the paraxial approximation and Taylor expansion of the wavevectors to proceed. As a result, an explicit wavevector mismatch, $\Delta\mathbf{k} = 2\mathbf{k}_p - \mathbf{k}_s - \mathbf{k}_i$. is obtained. Here, we kept the signal and idler electric fields general. As a result, the wavevector mismatch does not show up explicitly; nevertheless, optimum amplfication takes place when the sum over wavevectors is conserved; see also see Fig. 1.

Therefore, we have established that KIA is a generalization but mathematically equivalent to FWM. In the next chapter, we will quantitatively analyze general plane wave KIA theory using real example materials to illustrate how KIA can be used as an amplification technique.

3 Amplification of Plane Waves

3.1 General treatment

In this Chapter, the theory of plane wave KIA is developed. Granted, amplification of plane waves is an idealization, as plane waves can only be approximately realized in reality. However, many of the key ideas of KIA can still be explored using plane waves, which is the purpose of this Chapter. Furthermore, all the parameters and their definitions used in scalar KIA theory, both plane wave and finite pulse, are tabulated in appendix B for quick reference. In this section, we will initially use the vectorial theory for generality, but scalar theory will follow for the rest of the Chapter.

Consider as the initial condition a seed plane wave, inclined along k_y, $k_x = 0$, and with the assumption that $K_y \approx 0$ as compared to K_x, that is, $\widetilde{\mathbf{v}}_\perp(0) = (\widetilde{v}_x(0), 0)$, with

$$\widetilde{v}_x(0) = (2\pi)^{3/2} E_s \delta(k_x)\, \delta\left(k_y - \bar{k}_{\perp s}\right) \delta(\Omega - \Omega_s), \tag{68}$$

where E_s is the constant seed electric field amplitude, $\Omega_s = \omega_s - \omega_p$ is the seed frequency, and $\bar{k}_{\perp s} = \bar{k}_\perp(\Omega_s)$. After propagating a material length $z = l$, we have from Eqs. (39) and (35)

$$\widetilde{\mathbf{v}}_\perp(l) = \begin{pmatrix} 1 \\ \frac{l_{21}}{l_{11} - l_{22}} \end{pmatrix} \widetilde{v}_x(0) e^{iK_x l}. \tag{69}$$

As we are seeding at $k_x = 0$ and $l_{21} \propto k_x$, $\widetilde{v}_y(l)$ will vanish upon inverse Fourier transforming back to $\varepsilon_y(l)$. After inverse Fourier transforming, what remains is $\boldsymbol{\varepsilon}_\perp = (\varepsilon_x(\mathbf{x}, t), 0)$, where

$$\varepsilon_x(\mathbf{x}, t) = E_s e^{\bar{g}(\Omega_s) l/2} e^{-i\mathbf{K}_s \cdot \mathbf{x}} e^{i\omega_s t}, \tag{70}$$

and $\mathbf{K}_s = K(\Omega_s) = (0, \bar{k}_{\perp s}, K_{zs})$ is the seed wavevector, where $K_{zs} = K_z(\Omega_s) = k_p + \sigma(\Omega_s) D_u(\Omega_s)$, and $\mathbf{x} = (x, y, z = l)$. Optimum amplification occurs when the seed propagation axis lies along the line $k_y = \bar{k}_{\perp s}$ inclined with respect to the pump wavevector with half-angle $\theta_s = \theta(\Omega_s)$

$$\theta_s = \arctan\left(\frac{\bar{k}_{\perp s}}{K_{zs}}\right). \tag{71}$$

It should be mentioned that in the scalar limit where $r_0 \approx 0$, optimum amplification can take place along a cone around the pump wavevector as $k_x = 0$ need not be enforced. This is related to but, in general, not the same as the conical emission angle. Conical emission grows out of noise and occurs after filamentation has drastically modified the pump pulse. Seeded amplification assumes the pump pulse to be approximately undistorted and occurs over distances significantly shorter than the self-focusing distance necessary for filamentation [7].

The above analysis is immediately reduced to the scalar KIA theory by looking at the limit where $\Lambda_x \to 1$ (or $r_0 \to 0$), and $\widetilde{\mathbf{v}}_\perp(l) \to \widetilde{v}_x$. For the rest of the work, we will be considering this limit, as justified in section 2.5.

As mentioned in Chapter 1, the KIA process is phase-matched automatically, unlike conventional three or four-wave mixing processes, see Fig. (1). We have $\mathbf{v}_\perp \propto e^{-i\mathbf{K}(\Omega_s)\cdot\mathbf{x}}$ and $\mathbf{v}^*_{\perp(-)} \propto e^{i\mathbf{K}(-\Omega_s)\cdot\mathbf{x}}$. Since $\bar{k}_\perp(-\Omega_s) = \bar{k}_\perp(\Omega_s)$ and $K_z(-\Omega_s) = -K_z(\Omega_s)$, the left- and right-sides of Eq. (27) are phase-matched. Outside the instability regime, in the conventional regime of four-wave mixing, $K_g(\Omega_s)$ becomes real and $K_g(-\Omega_s) = K_g(\Omega_s)$; thus, phase-matching is no longer automatic.

In the following, the scalar theory of plane wave KIA in our aforementioned bulk dielectrics, CaF_2 and KBr, is quantitatively analyzed.

3.2 Scalar plane wave KIA in CaF_2 and KBr

We begin by considering CaF_2 to show how its optical properties affect plane wave KIA in a quantitative way. Then, the same analysis is done in KBr for comparative purposes.

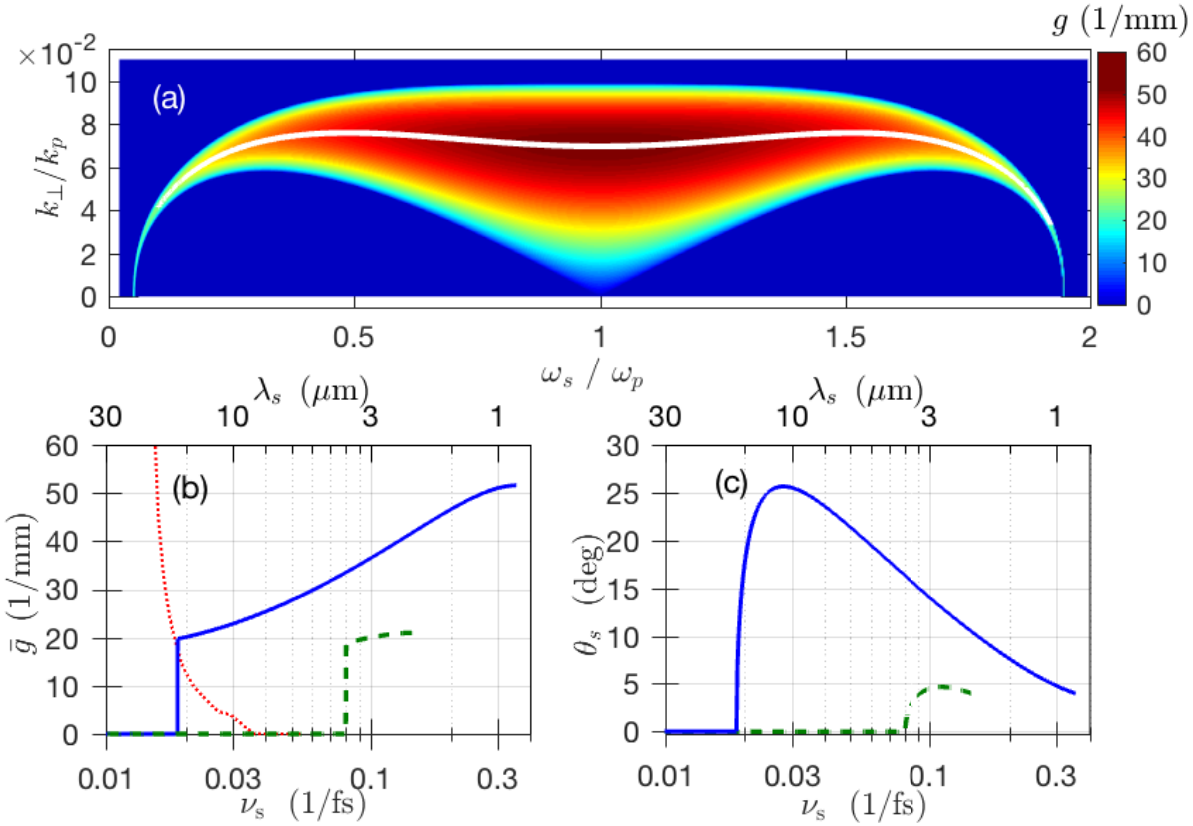

Figure 6: Plane wave amplification in bulk CaF_2 crystal. (a) Kerr instability gain, g versus ω_s/ω_p and $k_\perp/k_p$ (transverse over pump wavevector); pump wavelength $\lambda_p = 0.85\,\mu$m. The white line indicates $\bar{k}_\perp$ at which maximum gain $\bar{g} = g(\bar{k}_\perp)$ occurs, see Eq. (56). (b) $\bar{g}$ versus seed frequency $\nu_s = \omega_s/(2\pi)$ (bottom) and seed wavelength λ_s (top); red dotted line represents absorption. (b)-(c) $\lambda_p = 0.85, 2.1\,\mu$m corresponds to blue full, green dashed curves, respectively. (c) angle of inclination between pump and seed beam θ_s at which maximum amplification takes place versus ν_s and λ_s, see Eq. (71).

In Fig. 6(a) the intensity gain profile, g, from Eq. (54) is plotted versus ω_s/ω_p and $k_\perp/k_p$. The solid white line represents $\bar{k}_\perp$. The pump wavelength is $\lambda_p = 2\pi c/\omega_p = 0.85\,\mu$m and pump intensity is $I_p = 50$ TW/cm^2. Amplification occurs over a wide spectral range from $0.45 - 15\,\mu$m. The gain ceases along two curves which are defined by the relation discussed above Eq. (60). In Fig. 6(b) the maximum gain $\bar{g}$ is shown on the infrared side versus seed frequency ν_s (bottom axis) and seed wavelength λ_s (top axis). The two pump wavelengths $\lambda_p = 0.85, 2.1\,\mu$m correspond to the solid blue and dashed green curves, respectively, in 6(b) and (c). Maximum gain reaches a global maximum when pump and seed frequencies are equal and decreases with longer wavelengths. Further, $\bar{g}$ increases with pump frequency. For $\lambda_p = 0.85\,\mu$m the gain is still significant at $\lambda_s = 15\,\mu$m. Amplification, $e^{\bar{g}l}$, by more than 4 orders of magnitude can be obtained in a $l = 0.5$ mm long crystal. Note that gain and absorption balance each other at $\lambda_s = 20\,\mu$m. At this wavelength, the medium becomes transparent in the presence of the pump beam.

For $\lambda_p = 2.1\,\mu$m, the gain exists over a narrow spectral range. This is evident from Fig. 6(c), where the angle for maximum amplification, Eq. (71), is plotted for the same two pump wavelengths. At $\lambda_p = 2.1\,\mu$m, θ_s reaches a maximum near the pump wavelength and then decreases to zero rapidly. This property arises from the functional form of the angle θ_s, due to linear dispersion of $n(\omega)$. We observe that $\tan^2\theta_s \propto \kappa_\perp^2 \propto \sigma^2 - 1 \approx 2(n_g + n_u\Omega_s/\omega_p)/\eta_p$. The two terms, η_g and $\eta_u\Omega_s/\omega_p$, can have opposite or equal signs, depending on the material and pump wavelength, as mentioned above Eq. (55),. In this particular case, they are of opposite sign and comparable magnitude, so that for decreasing ν_s, $\kappa_\perp^2$ becomes negative. From Eqs. (55) and (56) we see that then $\bar{k}_\perp = \bar{g} = 0$ so that both gain and θ_s become zero. A similar behavior can be seen for $\lambda_p = 0.85\,\mu$m, but it is stretched out over a wider spectral range.

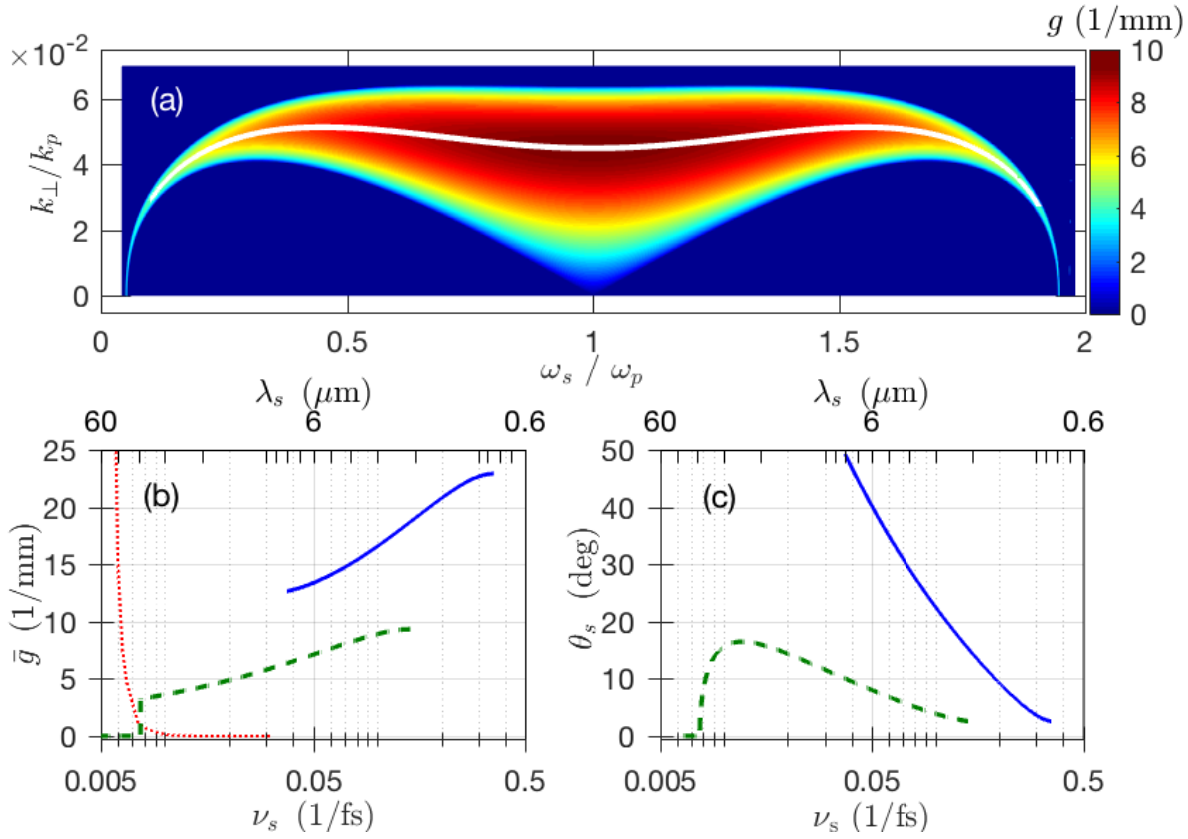

Figure 7: Plane wave amplification in bulk KBr crystal. Panels (a)-(c) correspond to those in Fig. 6. In (a) the pump wavelength is $\lambda_p = 2.1\,\mu$m; all other parameters and definitions in panels (a)-(c) are the same as given in the caption of Fig. 6.

In Fig. 7, the results for KBr crystals are shown for a pump intensity $I_p = 8$ TW/cm^2. The same line styles as in Fig. 6 are used. The gain in Fig. 7(a) is plotted for $\lambda_p = 2.1\,\mu$m. Unlike in CaF_2, using $\lambda_p = 2.1\,\mu$m works well in KBr. Gain exists over a transmission window twice as long as in CaF_2, see also Fig. 7(b). The maximum gain is still substantial near the edge of the transmission window, see the dotted red line. Amplification of more than

four orders of magnitude can be achieved over a crystal length $l = 2$ mm. For $\lambda_p = 0.85\,\mu$m, the gain exists in a narrower spectral range, up to $8\,\mu$m. The reason is clear from Fig. 7(c). For $\lambda_p = 0.85\,\mu$m, the angle rapidly increases for increasing λ_s.

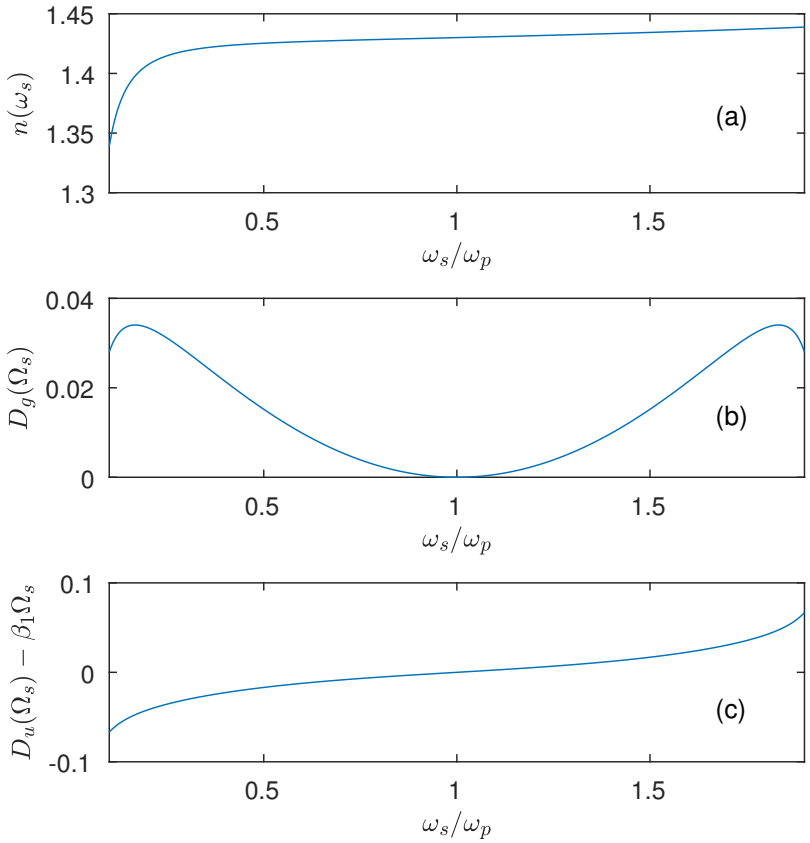

Figure 8: a) Refractive index of CaF_2 and exact dispersion functions b) D_g and c) $D_u - \beta_1\Omega_s$ versus seed over pump frequency; for definition see Eq. (44); $\omega_p = 0.85\mu$m.

As mentioned above for CaF_2, this comes from the fact that both terms in $\sigma^2 - 1$ have the same sign. Here, the gain ceases when the denominator in Eq. (51) approaches zero for $k_p = \sigma D_u$, as described above Eq. (52). By contrast for $\lambda_p = 2.1\,\mu$m, the signs are different and we see similar behavior as in Fig. 6(c). Linear dispersion strongly influences KIA and is a crucially important design parameter. The ultrawide frequency range and the large noncollinear angles encountered in Figs. 6 and 7 emphasize the necessity of our theoretical framework that does not rely on dispersion expansion and paraxial approximation, as discussed below Eqs. (44).

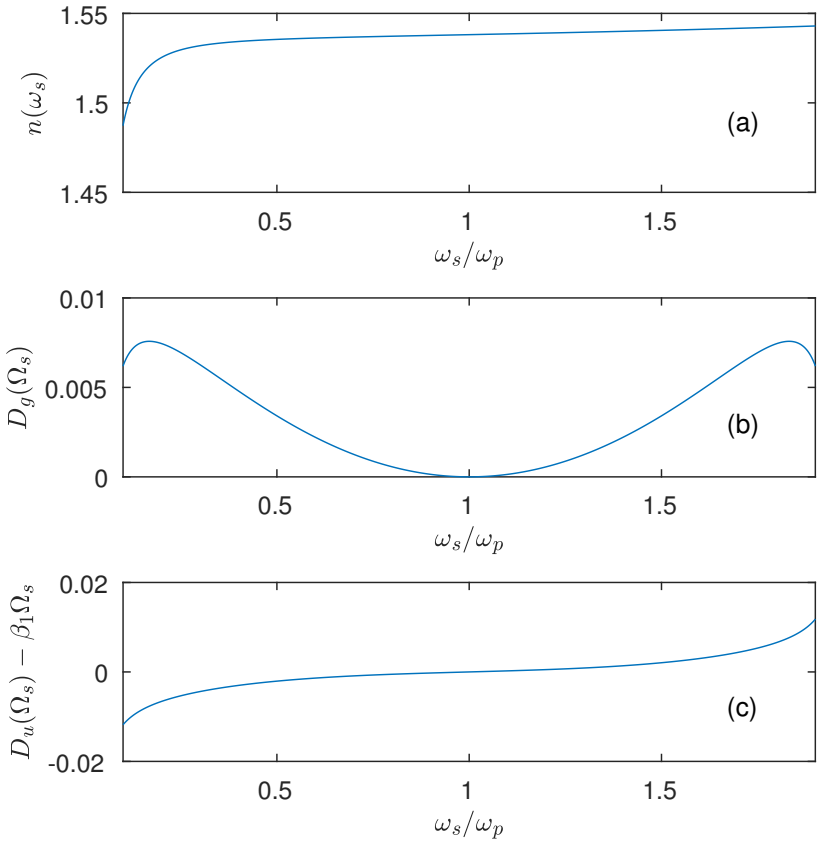

Figure 9: a) Refractive index of KBr and exact dispersion functions b) D_g and c) $D_u - \beta_1\Omega_s$ versus seed over pump frequency; for definition see Eq. (44); $\omega_p = 2.1\mu$m.

As mentioned in section 2.2, remember that the exact even and odd dispersion functions, D_g and D_u, defined in Eq. (44) are valid for an arbitrary frequency range. In Figs. 8 and 9, refractive index n, and D_g, $D_u - \beta_1\Omega_s$ are plotted versus seed frequency ω_s normalized to pump frequency ω_p for CaF_2 and KBr, respectively. We omit the dominating group velocity term, $\beta_1\Omega_s$, from the odd dispersion function in order to reveal the higher order structure.

Whereas in our work D_g and D_u are defined exactly, all other existing theories rely on a Taylor expansion of the dispersion functions about ω_p. Figures 8 and 9 demonstrate that Taylor expansion works well for seed frequencies close to the pump frequency. For the exploration of KIA, D_g and D_u are needed over the whole spectral range. In particular, near the wings of the curves in panels (b) and (c) convergence of the Taylor series becomes impractical at best, if not questionable. Although not relevant for this work, this is particularly true for materials with rapidly changing refractive index, such as metamaterials.

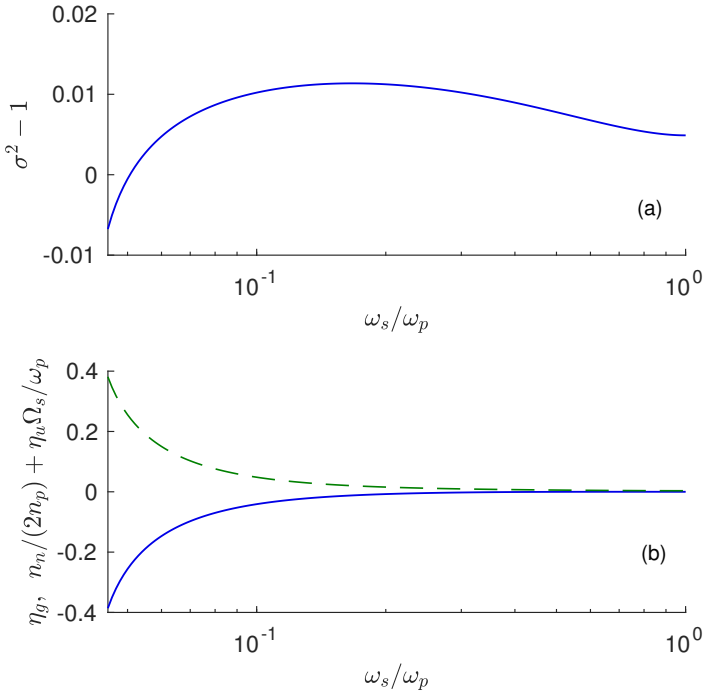

Figure 10: For CaF_2, (a) $\sigma^2 - 1$ and (b) η_g (solid blue curve) and $n_n/(2n_p) + \eta_u\Omega_s/\omega_p$ (dashed green curve); $\omega_p = 0.85\mu$m.

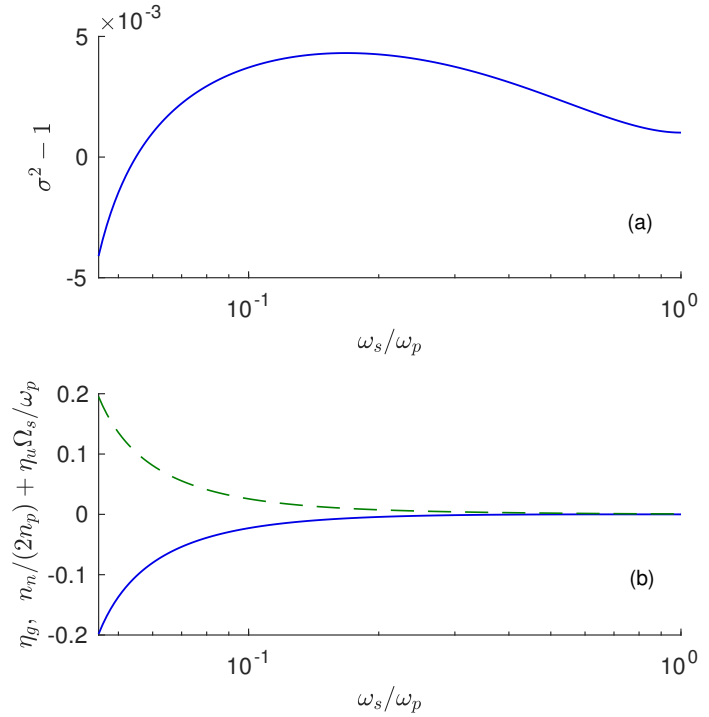

Figure 11: For KBr, (a) $\sigma^2 - 1$ and (b) η_g (solid blue curve) and $n_n/(2n_p) + \eta_u\Omega_s/\omega_p$ (dashed green curve); $\omega_p = 2.1\mu$m.

Next, we plot the dispersive function $\sigma^2 - 1$, where σ is defined by Eq. (49) in Figs. 10 and 11. As mentioned in section 2.2, the $\sigma^2 - 1$ term can change sign from positive to negative at specific wavelengths. The transverse wavevector (and hence noncollinear angle; see Eq.(71)) corresponding to maximum instability gain, $\bar{k}_\perp^2$, depends on $\kappa_\perp^2 \propto \sigma^2 - 1$, see Eqs. (55) and (56). Specifically, we have $\sigma^2 - 1 \approx (2/n_p)\,(n_n/(2n_p) + \eta_g + \eta_u \Omega_s/\omega_p)$. We plot $\sigma^2 - 1$ and its constituents η_g and $n_n/(2n_p) + \eta_u \Omega_s/\omega_p$ for both materials in Figs. 10 and 11.

In panels (a) of Figs. 10 and 11, the sign change of $\sigma^2 - 1$ occurs around $\omega_s/\omega_p \approx 0.05 - 0.055$. The instability gain hinges on small differences between the two curves, which is why it is essential to use the exact even and odd refractive indices η_g and η_u defined by Eqs. (44b) and (44a) of the main work.

Although very instructive, as mentioned above, plane wave KIA is ideallistic as plane waves do not exist in reality since they require infinite energy. Further, as we are interested in amplification of ultrashort pulses, the analysis must be extended to allow for finite seed pulses. This is done in the following chapter.

4 Amplification of Gaussian Beams

4.1 Theory

In extension of our plane wave analysis in the previous chapter, we explore KIA of finite Gaussian pulses in a noncollinear setup with seed and pump pulses inclined at the optimum gain angle θ_s. Our analysis relies on the assumption of a plane wave pump. This is justified, as long as the pump pulse is wider than the seed pulse so that its intensity varies weakly over the seed pulse. The seed pulse is assumed to be inclined at θ_s along x with a Gaussian spatial and temporal profile and field strength E_s. The spatial and temporal $1/e^2$-widths are $\mathrm{w}_x(0) = \mathrm{w}_x = 2/\Delta_x$, $\mathrm{w}_y(0) = \mathrm{w}_y = 2/\Delta_y$ and $\tau = \tau(0)$, respectively. The initial Gaussian seed pulse in the Fourier domain is given by

$$\tilde{v}_x(0) = \frac{2^{3/2} E_s f(\Omega)}{\Delta_x \Delta_y \Delta_\omega} \exp\left(-\left(\frac{k_x - \bar{k}_{\perp s}}{\Delta_x} \right)^2 - \left(\frac{k_y}{\Delta_y} \right)^2 \right), \tag{72}$$

where $f = \exp(-(\Omega - \Omega_s)^2/\Delta_\omega^2)$ with $\Delta_\omega(0) = \Delta_\omega = 2/\tau$. As the transverse wavevector of maximum amplification $\bar{k}_\perp(\Omega)$ varies as a function of frequency, (transverse) beam center and amplification maximum move increasingly apart with growing $|\Omega - \Omega_s|$. In the strong amplification limit the transverse beam center will align with the amplification maximum, resulting in an angular chirp [37]. That is, different frequency components have slightly different transverse wavevector centers. The amplified pulse spectrum can be approximately evaluated in an analytical way by Taylor expanding the gain g about $\bar{k}_\perp(\Omega)$. To leading order, this results in a Gaussian intensity amplification profile, where

$$g \approx \bar{g} - g_2 \, (k_x - \bar{k}_\perp)^2, \;\; g_2 = 2 k_p \bar{k}_\perp^2 \left[\delta_\perp^2 (k_p^2 - (\sigma D_u)^2) \right]^{-1}. \tag{73}$$

The gain only modifies the k_x pulse profile, due to the initial form of Eq. (72). Together with Eq. (52a), we obtain the Fourier beam amplitude after amplifier length l

$$\begin{aligned} \tilde{v}_x(\mathbf{k}_\perp, l, \Omega) = \tilde{v}_x(0) \exp\left(-i\sigma D_u l + \frac{1}{2} \bar{g} l \right) \exp\left(-\frac{i}{2} \alpha l k_y^2 \right) \\ \times \exp\left(-\frac{l}{2} (g_2 + i\alpha)(k_x - \bar{k}_\perp)^2 - i\alpha l \bar{k}_\perp (k_x - \bar{k}_\perp) \right), \end{aligned} \tag{74}$$

where $\alpha(\Omega) = \sigma D_u / (k_p^2 - (\sigma D_u)^2)$. Propagation in free space after the amplifier is not considered here.

Inverse Fourier transform with regard to $\mathbf{k}_\perp = (k_x, k_y)$ gives a complex shifted Gaussian beam

$$\tilde{v}_x(x, y, l, \Omega) = \frac{E_s \tau \mathrm{w}_x \mathrm{w}_y}{\sqrt{2 q_x q_y}} f(\Omega) \exp\left((\frac{\gamma}{2} - i\varkappa) l + i \bar{k}_{\perp s} x \right) \exp\left(-\frac{(x - x_c)^2}{q_x} - \frac{y^2}{q_y} \right) \tag{75}$$

with $\gamma = \bar{g} - g_2\,(\bar{k}_\perp - \bar{k}_{\perp s})^2$ and $\varkappa = \sigma D_u - (\alpha/2)(\bar{k}_\perp^2 - \bar{k}_{\perp s}^2)$; further, $q_x = \mathrm{w}_x^2 + 2(g_2 + i\alpha)l$, $q_y = \mathrm{w}_y^2 + 2i\alpha l$ are related to the $1/e^2$-beam widths via $\mathrm{w}_{x,y}^2(l) = |q_{x,y}|^2/\mathrm{Re}(q_{x,y})$, and the complex shift of beam center is given by $x_c = x_{cr} + ix_{ci} = \alpha l \bar{k}_{\perp s} + ig_2 l\,\left(\bar{k}_\perp - \bar{k}_{\perp s}\right)$. The subscript, s, denotes (Ω_s); otherwise the argument is (Ω).

From Eq. (75) the intensity spectrum follows as

$$|\tilde{v}_x(x,y,l,\Omega)|^2 = \frac{(E_s\tau \mathrm{w}_x \mathrm{w}_y)^2}{2|q_x q_y|}|f(\Omega)|^2 \exp\left(\Gamma l\right) \exp\left(-\frac{2(x-\xi_{cr})^2}{\mathrm{w}_x^2(l)} - \frac{2y^2}{\mathrm{w}_y^2(l)}\right). \tag{76}$$

Due to contributions from the imaginary parts in the exponent of (75) the shift of the beam center changes to $\xi_{cr} = x_{cr} + x_{ci}(\mathrm{Im}(q_x)/\mathrm{Re}(q_x))$; the gain changes to $\Gamma = \bar{g} - g_2\,(\bar{k}_\perp - \bar{k}_{\perp s})^2(\mathrm{w}_x^2/\mathrm{Re}(q_x))$. Taylor expansion of the gain about Ω_s yields $\Gamma(\Omega) = \Gamma_s + \Gamma_s'(\Omega - \Omega_s) + (1/2)\,\Gamma_s''(\Omega - \Omega_s)^2$. As a result, the amplified spectrum remains Gaussian. Integration over Ω by using the method of stationary phase results in a spectral $1/e^2$-width $\Delta_\omega(l) = 2/\tau_g(l)$. Here, $\tau_g(l) = (\tau^2 - \Gamma_s'' l)^{1/2}$ is the gain modified transform limited temporal $1/e^2$-duration which corresponds to the actual pulse duration $\tau(l)$ when the spectral chirp is neglected. Integration over transverse coordinates (see also Chapter 5 for comparison) yields the amplified seed pulse energy

$$\frac{W_s(l)}{W_s(0)} = \frac{\mathrm{w}_x}{\sqrt{\mathrm{Re}[q_x(\Omega_s)]}}\frac{\tau}{\tau_g(l)} \exp\left(\Gamma_s l + \frac{(\Gamma_s' l)^2}{2\tau_g^2(l)}\right), \tag{77}$$

where $W_s(0) = (\pi/2)^{3/2} I_s \tau \mathrm{w}_x \mathrm{w}_y$ and I_s are the initial seed pulse energy and intensity. Finally, spatio-temporal profiles and $\tau(l)$ are determined numerically from (75).

KIA operates in the limit where the amplified seed intensity is small compared to the pump peak intensity, so that nonlinear terms in Eq. (16) (including the $\boldsymbol{\nabla}(\boldsymbol{\nabla}\cdot\boldsymbol{\varepsilon})$ term) are negligible. This is fulfilled for $I_s(l) = I_p/10$; see Ref. [20]. The corresponding amplified seed pulse energy is $W_s(l) = (\pi/2)^{3/2} I_s(l)\tau(l)\mathrm{w}_x(l)\mathrm{w}_y(l)$, from which together with Eq. (77) the initial pulse energy and intensity are obtained. Next, we apply this theory quantitatively to the materials, CaF_2 and KBr.

4.2 Quantitative results in CaF_2 and KBr

For KIA in CaF_2 and KBr a material length $l = 8/\bar{g}(\omega_s)$ is assumed corresponding to a plane wave amplification factor of $\exp(8) \approx 3000$; l is changed with ω_s to make the plane wave amplification factor constant for all frequencies.

Efficient amplification requires the seed pulse to stay close to the pump pulse center over l. This requirement sets a lower limit for pump pulse duration and width, and thereby for the minimum pump energy.

There are four factors that cause an increase in pump energy requirements: i) the inclination between pump and seed pulse axes, resulting in a walk-off ξ_{cr} between beam centers; ii) widening of the seed beam widths $\mathrm{w}_{x,y}(l)$ due to diffraction and transverse spectral gain

narrowing; iii) a temporal walk-off, $\Delta\beta_1 l$, caused by the difference $\Delta\beta_1 = \beta_{1s} - \beta_1$ between seed group velocity $\beta_{1s} = [dK_u/d\Omega](\Omega_s)$ and pump group velocity β_1 defined below Eq. (44); and iv) lengthening of the seed pulse duration $\tau(l)$ due to spectral gain narrowing and dispersive effects.

These 4 conditions determine the required pump pulse parameters as $\mathrm{w}_p = r(\mathrm{w}_x(l) + 0.5|\xi_{cr}|)$ and $\tau_p = r(\tau(l) + 0.5|\Delta\beta_1|l)$; the factor 1/2 comes from the assumption that pump and seed beam centers are aligned at half of the material length; we chose the factor by which the pump beam is wider than the final shifted seed beam as $r = 3$ [20]. As a result, the minimum pump energy for KIA to operate efficiently is $W_p = (\pi/2)^{3/2} I_p \tau_p \mathrm{w}_p^2$ assuming a radially symmetric transverse pump beam.

A number of other processes need to be considered that can potentially limit KIA. Self focusing needs to be controlled. Critical self-focusing can be avoided by making the pump beam radius wide enough. We determine w_p from the requirement that the material length $l = l_{sf}/5$, where $l_{sf} = \mathrm{w}_p(n_p/(2n_n))^{1/2}$ is the distance for critical self focusing [1]. The initial seed beam width w_x is determined from a solution of

$$l_{sf}\sqrt{\frac{2n_n}{n_p}} = \mathrm{w}_p = r(\mathrm{w}_x(l) + 0.5|\xi_{cr}|) \tag{78}$$

with $\mathrm{w}_x(l)$ defined below Eq. (75); we assume $\mathrm{w}_y = \mathrm{w}_x$.

Small-scale self-focusing is a consequence of the Kerr instability. It amplifies noise superimposed onto the pump beam which ultimately results in filamentation [38]. The breakup develops at $\bar{k}_\perp(\omega_p)$ where the gain is maximum. By using $\bar{g}(\omega_s)l = 8$, we obtain the gain for the pump noise $\bar{g}(\omega_p)l = 8\bar{g}(\omega_p)/\bar{g}(\omega_s)$. For example, for $\omega_s/\omega_p = 0.2$ we find $\bar{g}(\omega_p)/\bar{g}(\omega_s) \approx 1.5$ from Figs. 12 and 13 (see below). As a result, the peak pump signal to noise ratio has to be $> e^{12} \approx 10^5$ to avoid pump beam breakup during KIA.

Pump pulse lengthening is a consequence of the interplay between nonlinear phase modulation and group velocity dispersion. Their influence is measured through nonlinear length $l_n = 2k_p/k_n^2 = 2n_p c/(n_n\omega_p)$ and dispersive length $l_d = 2\tau_p^2/\beta_2$ of the pump pulse. In the limit of strong KIA the nonlinear length is shorter than the material length. As a result, $l_d \gg l$ to avoid pump pulse stretching through the combined action of nonlinear phase modulation and dispersion.

Material damage and ionization limit the pump peak intensity to the material damage threshold intensity $I_{th} = (2/\pi)^{1/2} F_{th}/\tau_p$. We use damage threshold fluence values F_{th} from the literature. Ionization becomes important around the damage intensity which results in pump pulse absorption and defocusing through the free electron lens [7]; for a more detailed discussion, see section 4.5. Recently, KIA factors of > 1000 have been demonstrated in yttrium alluminum garnet (YAG) crystal with $\tau_p = 140$fs and $I_p = 8\mathrm{TW/cm}^2$ which is comparable to the parameters used below [20]. Damage fluence for YAG is $F_{th} \approx 1.4\,\mathrm{J/cm}^2$. Ionization did not present a limiting factor, not even at intensities close to the damage threshold.

Contributions from the frequency-dependence of the Kerr nonlinearity are small. In the wavelength range of interest here; far away from the bandgap, the electronic part of n_2 undergoes little variation [39]. The Raman response times of $\approx 0.5 - 1$ ps are longer than the seed and pump pulse durations used in the analysis below which justifies neglect of the frequency dependence [40, 41].

The quantitative results for finite pulse KIA in CaF_2 and KBr for a material length $l = 8/\bar{g}(\Omega_s)$ are shown in Figs. 12 and 13, respectively. Pump peak intensities for CaF_2 and KBr are chosen as $I_p = 50$ TW/cm^2 and $I_p = 8$ TW/cm^2, respectively. Following the results of the plane wave analysis above, we chose $\lambda_p = 0.85\,\mu$m and $\lambda_p = 2.1\,\mu$m for CaF_2 and KBr, respectively. The damage threshold fluence of CaF_2 and KBr in the sub-ps pulse duration regime is $F_{th} = 6.7$ J/cm^2 and $F_{th} = 3.3$ J/cm^2 [42], respectively; for n_2 see caption. We assume single cycle initial seed pulses with $I_s(l) = I_p/10$. Initial seed pulse radius is determined from a solution of Eq. (78).

Seed pulse energy increase $W_s(l)/W_s(0)$ in Fig. 12(a) is close to the plane wave value $\exp(\bar{g}l) \approx 3000$ (black, dashed line) for $\omega_s/\omega_p \geq 0.5$ and drops from there; at $\omega_s/\omega_p = 0.2$ amplification is still more than a factor of 1000.

In Fig. 12(b) the $1/e^2$-pulse duration $\tau(l)$ (blue, full) is obtained from transverse space integration over the spatio-temporal intensity profile; the intensity profile is calculated as the absolute square of the Fourier transform of Eq. (75). The pulse duration $\tau(l)$ is compared to $\tau_g(l)$ (green, dashed) which is the corresponding transform limited (chirp free) pulse duration defined below Eq. (76). Comparison shows that up to $\omega_s/\omega_p \approx 0.3$ amplification of single cycle pulses is possible and that the influence of dispersive effects is weak; even at $\omega_s/\omega_p = 0.2$ amplification of two cycle pulses is still feasible. Below that the pulse duration rises quickly due to a mixture of gain and dispersive widening. The spectral chirp incurred during KIA is dominantly linear (see section 4.3), and can be compensated in a post compression stage. The resulting pulses are transform limited pulses with duration $\tau_g(l)$. Finally, the red dotted line indicates the shift between peak of seed and pump pulse due to group velocity mismatch.

Widening of the seed beam radius is not dramatic, as can be seen in Fig. 12(c). That is due to the fact that a large pump beam radius is required to avoid self-focusing. This results in a large seed beam radius, as in our above design considerations the seed radius increases proportional with the pump radius. In general, it is desirable to choose the seed beam radius as large as possible to optimize energy extraction from the pump beam. We find that (green, dashed) $\mathrm{w}_y(l) \approx \mathrm{w}_x(0) = \mathrm{w}_y(0)$ which is why the initial pulse radii are not plotted. Amplification moderately widens $\mathrm{w}_x(l)$ (blue, full), as defined below Eq. (75), and results in a beam asymmetry which is weak over most of the frequency range.

In Fig. 12(d) the minimum pump pulse energy needed for KIA to work and the corresponding amplified seed pulse energy are plotted versus ω_s/ω_p. Naturally, higher seed energies can be obtained when more pump energy is available. At $\omega_s/\omega_p = 0.2$ we find $W_p = 4$ mJ which is comfortably available in Ti:sapphire laser systems. The pump energy is larger than the final seed energy by a factor of about $400 - 500$.

The nonlinear length l_n (green dashed) is shorter than the amplifier length, see Fig. 12(e).

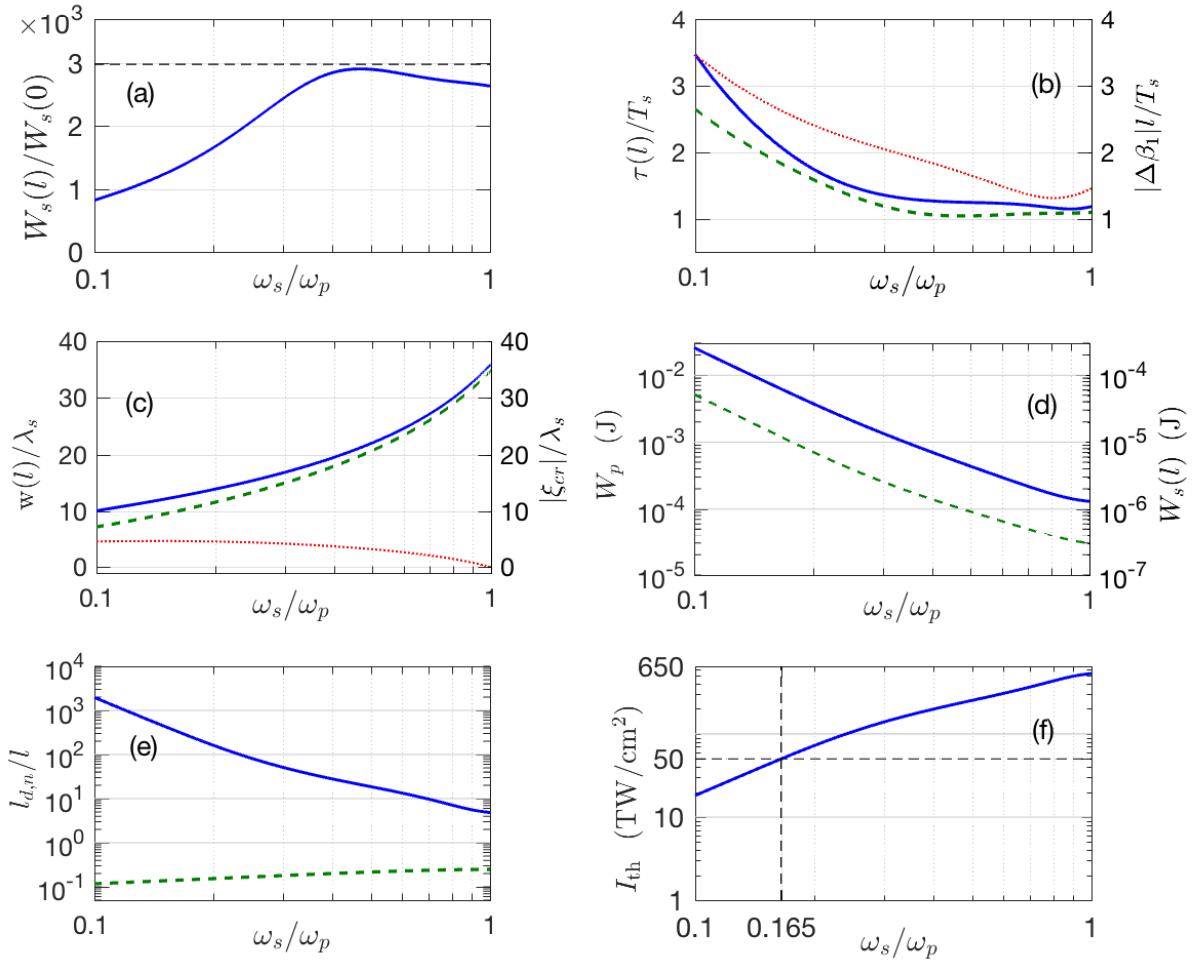

Figure 12: KIA of single cycle pulse $\tau(0) = T_s = 2\pi/\omega_s$ in CaF_2; $n_2 = 2 \times 10^{-16}$ cm^2/W; pump peak intensity $I_p = 50$ TW/cm^2, pump wavelength $\lambda_p = 0.85\,\mu$m, amplifier length $l = 8/\bar{g}$; pump beam radius and duration w_p, τ_p, see text above Eq. (78); initial seed beam radii, $w_x(0) = w_y(0)$, are determined from Eq. (78). (a) Seed pulse energy increase $W_s(l)/W_s(0)$ from Eq. (77) versus ω_s/ω_p (seed over pump frequency); black dashed line corresponds to the cw limit $\exp(\bar{g}l) = \exp(8) \approx 3000$. (b) amplified seed pulse duration $\tau(l)/T_s$ (blue full); transform limited amplified seed pulse duration $\tau_g(l)/T_s$ defined above Eq. (77) (green, dashed), and group velocity walk off between pump and seed, $|\Delta\beta_1|l/T_s$, versus ω_s/ω_p (red, dotted). (c) amplified seed beam radii $w_x(l)/\lambda_s$ (blue, full) and $w_y(l)/\lambda_s$ (green, dashed) versus ω_s/ω_p; initial beam radius is not plotted as $w_y(l) \approx w_x(0) = w_y(0)$; shift of seed beam center $|\xi_{cr}|$ defined below Eq. (76) (red dotted). (d) Minimum required pump energy W_p (blue, full), see text above Eq. (78), and corresponding seed energy $W_s(l)$ (green, dashed) versus ω_s/ω_p. (e) dispersive length l_d/l (blue, full) and nonlinear length l_n/l (green, dashed) versus ω_s/ω_p. (f) Damage threshold intensity I_{th} versus ω_s/ω_p; dashed lines indicate $I_p = I_{th}$.

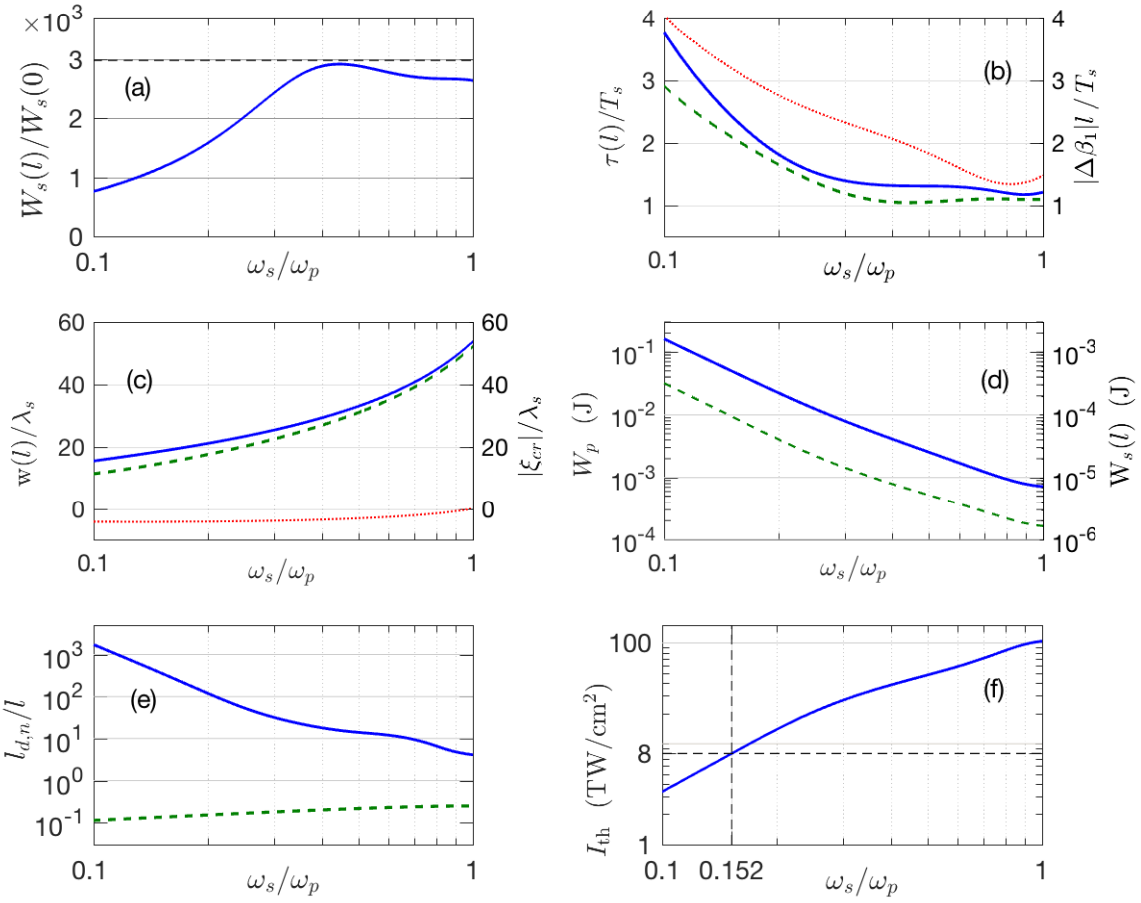

Figure 13: KIA of single cycle pulse $\tau(0) = T_s$ in KBr. Here $n_2 = 6 \times 10^{-16}$ cm^2/W, the pump peak intensity is $I_p = 8$ TW/cm^2 and the pump wavelength is $\lambda_p = 2.1\,\mu$m. Panels (a)-(f) correspond to those in Fig. 12. See the caption to Fig. 12 for a complete description.

The dispersive length l_d (blue, full) is between two to four orders of magnitude longer than the medium length so that no significant pump pulse distortions are expected through the interplay of Kerr nonlinearity and group velocity dispersion.

Finally, Fig. 12(f) shows the damage threshold intensity I_{th} for a pump pulse with pulse duration $\tau(l)$. The dashed line indicates the value of $\omega_s/\omega_p = 0.165$ at which $I_p = I_{th}$. As a result, we can conclude that amplification for a wavelength range between $\lambda_s = 0.85\,\mu$m and $\lambda_s \approx 5.2\,\mu$m is possible. The damage intensity presents a main limitation in extending KIA to even longer wavelengths. Note that towards higher ω_s damage does not present a problem as I_{th} increases quickly due to shorter required pump pulse durations.

The results for KBr in Fig. 13 are qualitatively similar to what was found for CaF_2 in Fig. 12; therefore we focus on a discussion of Fig. 13(d) and (f). The minimum required pump energy is $W_p \approx 20$ mJ at $\omega_s/\omega_p = 0.2$. This is in the range of what can be achieved by current state of the art Ho:YAG femtosecond amplifier systems operating at wavelengths $\lambda_p = 1.9 - 2.1\,\mu$m [24]. The corresponding seed amplified energy is $W_s \approx 50\,\mu$J. From 13(f) we find that KIA is possible to infrared wavelengths around $\lambda_s \approx 14\,\mu$m. For single-cycle KIA high I_p is necessary to minimize pulse widening.

4.3 Spatiospectral and Spatiotemporal quality of amplified pulses

It is instructive to look at the quality of the amplified pulses. In this respect, our two materials behave fairly similarly, which is why we show only the results for CaF_2 and $\lambda_p = 0.85\,\mu$m. For other parameters, see Fig. 12. In Fig. 14(a),(c) the spatio-spectral intensity profile $|\tilde{\varepsilon}_x(x, y = 0, z = l, \omega)|^2$ is plotted for $\omega_s/\omega_p = 0.2, 0.4$, respectively; Figures 14(b),(d) show the corresponding spatio-temporal profiles $|\varepsilon_x(x, y = 0, z = l, t)|^2$. Peak values are normalized to unity. The spectrum peak is shifted off $\omega/\omega_s = 1$ towards higher frequencies because the blue part of the seed spectrum is amplified more strongly. As for $\omega_s/\omega_p \leq 0.4$, $\bar{g}$ increases towards higher seed frequencies. Further, the spectrum exhibits some asymmetry which is not contained in the quadratic expansion of Γ below Eq. (76); accounting for it analytically would require expansion to third order. Since the maximum gain, $\bar{g}$ is experienced at finite transverse wavevector $\bar{k}_\perp(\Omega)$, the value of which is frequency dependent, the result is a Gaussian pulse in the space domain shifted by x_c, see Eq. (75). The real part of the shift ξ_{cr} manifests as an off-axis shift of the pulse center, see the white line in 14(a),(c). The shift changes slightly with frequency as a result of the angular chirp, i.e. each frequency experiences optimum amplification at a slightly different angle. The angular chirp needs to be compensated, otherwise the frequency dependent shift of the pulse center will continue growing during free space propagation [20], resulting in a degradation of the pulse quality. It can be estimated from the slopes in Figs. 6(c) and 7(c) that $d\theta_s/d\lambda_s = 0.1,\ 0.025$ rad/μm for CaF_2 and KBr, respectively. The imaginary part x_{ci} has an effect on the spatio-temporal pulse in 14(b), (d). An x-dependent group velocity component develops which skews the pulse in the $x - t$ plane. The pulse distortion becomes pronounced for $\omega_s/\omega_p \leq 0.2$ and is negligible for $\omega_s/\omega_p \geq 0.35$.

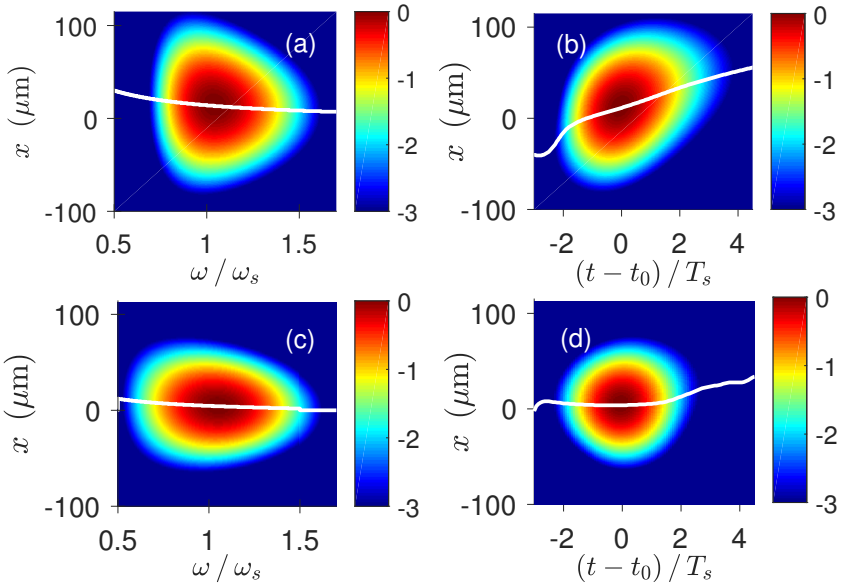

Figure 14: Spatio-spectral (a,c) and spatio-temporal (b,d) intensity profiles of seed pulses amplified in CaF_2 for $\omega_s/\omega_p = 0.2, 0.4$, respectively; parameters are the same as in Fig. 12. Peaks are normalized to unity; time is given with reference to time t_0 of the pulse peak and normalized to the optical cycle T_s. The white lines indicate the transverse pulse maximum.

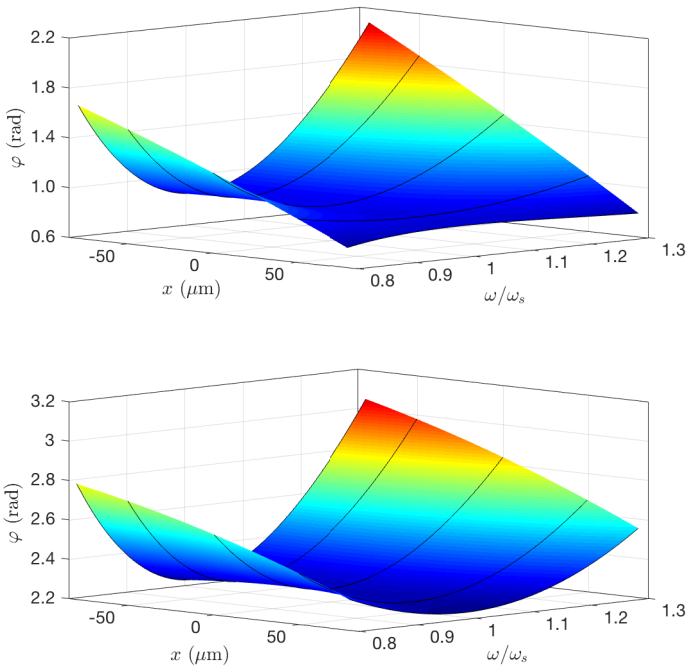

Figure 15: (a,b) Spectral phase corresponding to the amplified intensity spectrum (CaF_2) plotted in Fig. 14(a) and (c) for $\omega_s/\omega_p = 0.2, 0.4$, respectively. Carrier phases which are a linear function of space and frequency have been removed; only quadratic and higher polynomial dependencies can be observed.

In Fig. 15(a, b) we plot the corresponding spectral phase for the same seed frequencies, $\omega_s/\omega_p = 0.2, 0.4$, respectively. The spectral phase is calculated from the amplified pulse spectrum (75) and by subtracting the carrier phases which are a linear function of space and frequency. As a result, only quadratic and higher polynomial dependencies (first and higher order spectral chirp) can be observed in the plotted phase. As seen in Fig. 15 the phase exhibits a predominantly quadratic frequency dependence (linear chirp), with panel (a) demonstrating a slight cubic dependence, especially for $x \geq 50$ μm. In both cases, the higher order phase is weak, with higher order terms becoming increasingly important as ω_s gets smaller, consistent with Fig. 14.

4.4 KIA operation at lower peak intensity

In Figs. 16 and 17, we will briefly explore KIA operation at lower peak pump intensities, I_p.

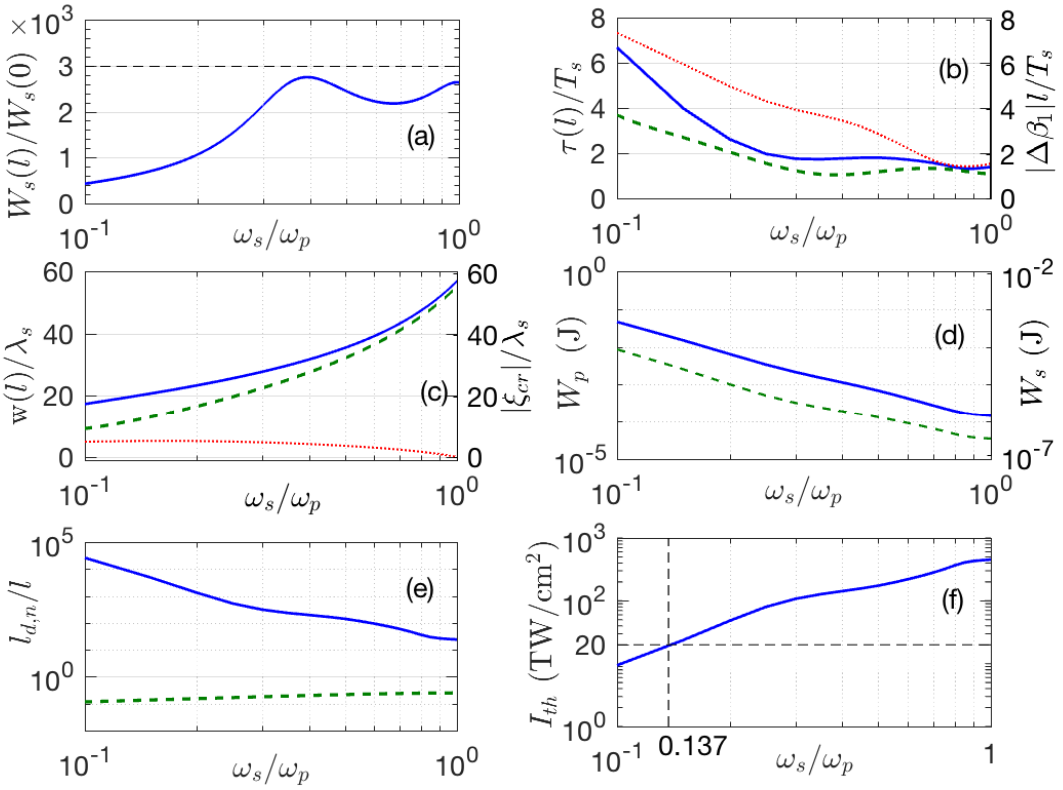

Figure 16: All parameters and definitions are the same as in Fig. 12 of the main work (CaF_2), except the pump intensity is reduced to $I_p = 20\,\mathrm{TW/cm^2}$.

The same parameters are used as in Figs. 12 and 13 of the main work for CaF_2 and KBr, except for about half the pump intensity $I_p = 20\,\mathrm{TW/cm^2}$ and $I_p = 4\,\mathrm{TW/cm^2}$, respectively. Lower pump peak intensities result in a lower nonlinear refractive index n_n. As a result,

longer material lengths, l, are needed to realize the same amplification factor. Larger l results in stronger temporal and spatial dispersive effects and, therefore, in longer and wider amplified seed pulses, compare Figs. 16(b, c) and 17(b, c) with Figs. 12(b, c) and 13(b, c), respectively.

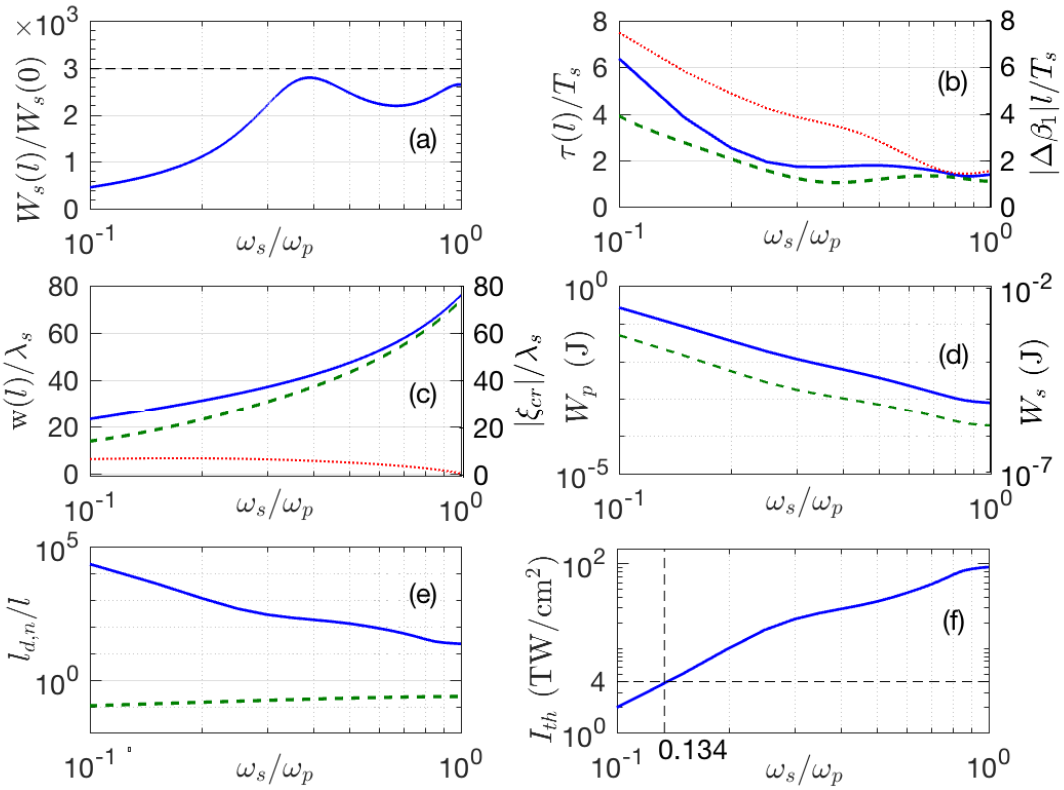

Figure 17: All parameters and definitions are the same as in Fig. 13 of the main work (KBr), except the pump intensity is reduced to $I_p = 4\,\mathrm{TW/cm^2}$.

As a result, direct single-cycle pulse amplification is no longer possible; the pulse durations $\tau(l)$ in Figs. 16 and 17 are about two cycles long (blue, full). However, the transform limited pulse duration $\tau_g(l)$ is still about $1 - 1.5$ cycles long (green, dashed). As seen in section 4.3, the spectral chirp is dominantly linear so that it can be compensated by standard methods. As a result, amplification of 1 to 1.5 cycle pulses should still be possible.

The second difference comes from the fact that we assume a fixed ratio between seed and pump pulse duration, because the seed pulse needs to remain close to the peak of the pump pulse and should experience a fairly flat pump pulse profile. As a result, the longer and wider amplified seed pulses require longer and wider pump pulses and therefore higher pump energies, compare Figs. 16(d) and 17(d) with Figs. 12(d) and 13(d), respectively.

By comparing Figs. 16(f) and 17(f) with Figs. 12(f) and 13(f), we find that for lower I_p the intersection of I_p with the damage threshold curve I_{th} moves to smaller frequencies ω_s/ω_p

by about 15%, so that the amplification range is extended. Therefore, to some extent damage and ionization problems can be resolved by using lower peak intensities. However, assume we maintain the original peak pump intensities of $50\,\mathrm{TW/cm^2}$ and $8\,\mathrm{TW/cm^2}$ for CaF_2 and KBr, respectively. Do these intensities ionize the materials, creating a plasma defocusing lens in the refractive index that hinders the amplification process? This is explored in the next section.

4.5 Plasma effects

In this section, we analyze the contribution from the free electron ionization to the refractive index. High intensity pump pulses cause ionization and the resulting plasma acts as a defocusing lens. As long as plasma defocusing is comparable to self-focusing, it will support KIA as it mitigates self-focusing and extends the distance for critical self-focusing discussed in the main manuscript. A defocusing lens much stronger than the self-focusing lens is not desirable, as it will rapidly reduce the pump peak intensity and throttle KIA gain.

The pump wavevector in the presence of free electrons is given by

$$k_p = \frac{\omega_p}{c}\left[n_p^2 - \Delta n_{pl}\right]^{1/2}, \tag{79}$$

where ω_p and n_p are the pump frequency and linear refractive index at the pump frequency, respectively, and

$$\Delta n_{pl} = \frac{\omega_{pl}^2}{\omega_p^2} \tag{80}$$

corresponds to the plasma induced change of the refractive index. The plasma frequency is given by

$$\omega_{pl}^2 = \frac{Ne^2}{\varepsilon_0 m^*}. \tag{81}$$

Here, m^* is the effective electron mass at the minimum bandgap of the material, e is the electron charge, and ϵ_0 is the vacuum permittivity. Further, N is the maximum density of ionized electrons (population in the conduction bands) after the laser pulse and at its pulse center. As ionization varies over the pulse profile, a refractive index profile is created that acts as a negative lens and defocuses the pump beam.

This has to be compared to the maximum Kerr nonlinear change of the refractive index Δn_{sf}

$$\Delta n_{sf} = n_2 I_p, \tag{82}$$

with n_2 and I_p the Kerr nonlinear index and peak pump intensity, respectively, which is

obtained from the wavevector (see below Eq. (15))

$$k_p = \frac{\omega_p}{c}\left[n_p^2 + \Delta n_{sf}\right]^{1/2}. \tag{83}$$

The maximum conduction electron density N (after the laser pulse and at pulse center) is calculated by solving the multi-band equations for CaF_2 and KBr [43]. The used bands and material parameters are from Ref. [44] for CaF2 and from Ref. [45] for KBr. Laser polarization is directed along the $\Gamma - X$ direction; $\omega_p/\omega_s = 6$ and pulse duration is $\tau_p = 12T_s$, representing a typical pump pulse duration needed for amplification of seed pulses at the long wavelength limit, see Figs. 12 and 13. For KIA in CaF_2 at pump frequency $\omega_p = 2.2 \times 10^{15}$ rad/s, we use peak pump intensity $I_p = 50$ TW/cm^2 in Fig. 12 and $I_p = 20$ TW/cm^2 in Fig. 16. The effective mass $m^* = m_e$ with m_e the free electron mass. The ionization calculations yield after the laser pulse $N = 2.1 \times 10^{19}$ cm^{-3} and $N = 6 \times 10^{17}$ cm^{-3}, respectively. This results in $\Delta n_{pl} \approx 1/80$ and $\Delta n_{pl} \approx 1/2700$, respectively. By comparison, the Kerr nonlinear index change for the two intensities is $\Delta n_{sf} = 1/100$ and $\Delta n_{sf} \approx 1/250$, respectively.

For KIA in KBr, the pump frequency is $\omega_p = 9 \times 10^{14}$ rad/s and we used $I_p = 8$ TW/cm^2 in Fig. 13 and $I_p = 4$ TW/cm^2 in Fig. 17 of the supplement. The effective mass is $m^* = 0.5m_e$; ionization yield after the laser pulse is $N = 1.2 \times 10^{18}$ cm^{-3} and $N = 6.5 \times 10^{16}$ cm^{-3}, respectively. This results in $\Delta n_{pl} \approx 1/100$ and $\Delta n_{pl} \approx 1/1850$, respectively. By comparison, the Kerr nonlinear index change for the two intensities is $\Delta n_{sf} = 1/200$ and $\Delta n_{sf} = 1/400$, respectively.

In both cases, defocusing is comparable to self-focusing at the highest intensities. This might present an advantage for KIA as the two lenses compensate each other. Whereas in CaF_2 $\Delta n_{pl}/\Delta n_{sf} \approx 1$, we find $\Delta n_{pl}/\Delta n_{sf} \approx 2$ in KBr. We would like to point to recent experiments which reveal that ionization theories have considerably overestimated ionization in dielectrics for the past 50 years [46]; this is currently a topic of active research [47, 48]. Therefore, theoretical predictions of ionization carry some degree of uncertainty.

There is another potential limitation. At the highest intensities, the plasma frequency becomes comparable to the longest seed frequencies that can be amplified. When the two are equal, the plasma becomes reflective for the seed pulse. To estimate this effect, the conduction electron density has to be taken at the pulse center and results in half the numbers given above.

Taking all of this into consideration, we conclude that plasma formation could become a problem at the highest intensities considered here. Whether this is really the case will have to be settled by experiment. Adverse effects from plasma generation can be easily defused by somewhat lowering peak intensities. At the lower pair of peak intensities KIA still works well, as demonstrated above, and plasma effects are considerably reduced. As mentioned in secion 4.4, the resulting compromise by moving towards lower peak intensities is a decrease in amplification bandwidth from single cycle towards two cycle pulses.

In summary, we have introduced a new concept for amplification of mid infrared pulses based on the Kerr instability. Our theoretical analysis of KIA in CaF_2 and KBr crystals

demonstrates the potential to amplify pulses in the wavelength range $\approx 1-14\,\mu$m. Whereas plane wave amplification in KBr extends to $40\,\mu$m, material damage limits finite pulse KIA to about $14\,\mu$m. There, seed pulse output energies in the $50\,\mu$J range appear feasible with a ratio of pump to seed pulse energy in the range 400-500. Our numbers are comparable to the performance of optical parametric amplifiers.

The biggest three advantages of KIA are the capacity for single cycle pulse amplification, that it is intrinsically phase-matched, and its simplicity and versatility. Kerr materials are more easily available than infrared materials with second order nonlinearity. Further, amplifier wavelength can be selected by simply changing the angle between pump and seed beam. The biggest drawback is an angular chirp acquired during amplification that needs to be controlled. There exist methods to that end, from a simple prism to more sophisticated techniques. [49].

The results shown here are promising, but most likely still far from optimum. There is a huge parameter space to be explored, such as all potential infrared crystals. Further, KIA can be optimized by determining favorable optical properties (e.g. the refractive index) from our theory and then designing corresponding synthetic materials.

The Kerr instability wavevector exhibits transverse symmetry. This is evident by the fact that Eq. (52) depends on transverse wavevectors via $k_\perp$ only, k_x and k_y do not need to be considered independently. This, and the fact that we consider the strong amplification regime where Taylor expansion of the gain to second order is sufficient results in the KIA gain profile to have a Bessel-Gaussian profile in real space. Therefore KIA should lend itself naturally to the amplification of Bessel-Gauss beams. This is explored in the next Chapter.

5 Amplification of Bessel-Gaussian Beams

5.1 Theory

The gain profile is a transversely-symmetric Gaussian profile in k-space when Taylor expanded to leading order, which is analogously done along k_x only as done in Chapter 4 (see Eq. (73)). Here, the amplification occurs in a ring in the $k_x - k_y$ plane with radius $\bar{k}_\perp$, as will be shown below (see Eq. (87)). As such, the gain profile in real space becomes Bessel-Gaussian, which is evident when converting from transverse Cartesian (k_x, k_y) to transverse polar $(k_\perp, \widetilde{\theta})$ coordinates. If the initial perturbation to the pump is transeversely symmetric, the Bessel-Gaussian profile of the amplified perturbation is maintained. As a result, we expect that if the inital seed is a Bessel-Gaussian beam, then the entire ring of maximum gain in k-space may be accessed, yielding more efficient amplification than for a Gaussian seed. Note that Bessel-Gaussian beams are a well-known solution to the paraxial wave equation and have various applications [50–53].

To quantitatively analyze Kerr instability amplification of Bessel-Gaussian beams, we assume the initial transverse profile of the seed beam to be Bessel-Gaussian in form

$$\varepsilon(0, r, t) = E_s e^{-t^2/\tau_s^2} e^{i\omega_s t} e^{-r^2/w_r^2} J_0\left(\bar{k}_{\perp s} r\right) \tag{84}$$

where E_s is the electric field amplitude, ω_s is the seed angular frequency, τ_s and w_r are the initial duration and waist of the beam, respectively; $J_0(\bar{k}_{\perp s} r)$ is a zeroth-order bessel function of the first-kind, and $\bar{k}_{\perp s} = \bar{k}_\perp(\omega_s)$ is the transverse seed wavevector that results in the maximum Kerr instability mentioned above, where $\bar{k}_\perp$ is defined by Eq. (55). The central core of $J_0(\bar{k}_{\perp s} r)$ has radius $\sim 2.4/\bar{k}_{\perp s}$, with the outer rings pushed out by successive zeroes of the Bessel function, which become increasingly faint as the Gaussian function decays with r. In the Fourier domain, the initial profile for the transformed field $\varepsilon(0, r, t) = v(0, r, t)e^{i\omega_p t}$, with ω_p the pump angular frequency, is given by

$$\begin{aligned}
\mathscr{F}\left[\varepsilon(0, r, t)\right] &= (2\pi)^{-3/2} \int_{-\infty}^{\infty} e^{-i\omega t} e^{i\omega_p t} dt \int_0^{2\pi} \exp\left[ik_\perp r \cos(\theta - \tilde{\theta})\right] d\theta \int_0^{\infty} r v(0, r, t) dr \\
&= (2\pi)^{-1/2} \int_{-\infty}^{\infty} e^{-i\Omega t} dt \int_0^{\infty} r v(0, r, t) J_0(r k_\perp) dr = \widetilde{v}(0, k_\perp, \Omega),
\end{aligned} \tag{85}$$

where $\Omega = \omega - \omega_p$, and we have converted from cartesian $(x, y; k_x, k_y)$ to radial $(r, \theta; k_\perp, \tilde{\theta})$ coordinates due to the radial symmetry of the initial seed. Inserting Eq. (84) into (85) and integrating [54] results in

$$\widetilde{v}(0, k_\perp, \Omega) = 2^{-3/2} E_s w_r^2 \tau_s f(\Omega) \exp\left[-\frac{w_r^2}{4}(k_\perp^2 + \bar{k}_{\perp s}^2)\right] I_0\left(\frac{w_r^2 \bar{k}_{\perp s} k_\perp}{2}\right), \tag{86}$$

where $f(\Omega) = \exp\left[-\tau_s^2(\Omega-\Omega_s)^2/4\right]$, $\Omega_s = \omega_s - \omega_p$, $k_\perp^2 = k_x^2 + k_y^2$ is the transverse wavevector squared, and I_0 is the modified zeroth-order Bessel function of the first kind. After interacting with the pump beam for a length $z = \ell$, the Fourier-transformed amplified seed profile is given by (see asymmetric version in Eq. (74))

$$\widetilde{v}(\ell, k_\perp, \Omega) = \widetilde{v}(0, k_\perp, \Omega) \exp\left[\frac{\bar{g}\ell}{2} - \frac{g_2\ell}{2}\left(k_\perp - \bar{k}_\perp\right)^2\right] \exp\left[-i\sigma D_u \ell - i\frac{\alpha\ell}{2}\left(k_\perp^2 - \bar{k}_\perp^2\right)\right] \quad (87)$$

where all parameters are the same as those in Chapter 4, see appendix B for a quick view of their definitions. We take the inverse Fourier transform over transverse coordinates of Eq. (87) by using the approximation,

$$I_0\left(w_r^2 \bar{k}_{\perp s} k_\perp/2\right) e^{g_2\ell\bar{k}_\perp k_\perp} \approx \frac{1}{w_r}\left[w_r^2 + 2g_2\ell\frac{\bar{k}_\perp}{\bar{k}_{\perp s}}\right]^{1/2} I_0\left[\left(\frac{w_r^2\bar{k}_{\perp s}}{2} + g_2\ell\bar{k}_\perp\right)k_\perp\right]. \quad (88)$$

Eq. (88) is valid since $k_\perp \geq 0$. As a result, we obtain the amplified profile

$$\widetilde{v}(\ell, r, \Omega) = \sqrt{\frac{Q_r}{2}}\frac{w_r}{q} E_s \tau_s f(\Omega) \exp\left[\frac{\Gamma}{2}\ell - i\varphi\right] \exp\left[-\frac{r^2}{q}\right] J_0\left[\frac{Q_r}{q}\bar{k}_{\perp s} r\right], \quad (89)$$

where $q = w_r^2 + 2\left(g_2 + i\alpha\right)\ell$, $Q_r = w_r^2 + 2g_2\ell\bar{k}_{\perp s}^{-1}\bar{k}_\perp$, $\Gamma = \bar{g} - g_2 w_r^2\left(w_r^2 + 2g_2\ell\right)|q|^{-2}\left(\bar{k}_\perp - \bar{k}_{\perp s}\right)^2$, and $\varphi = \sigma D_u\ell + 2^{-1}\alpha\ell w_r^2|q|^{-2}\left[w_r^2\left(\bar{k}_\perp^2 - \bar{k}_{\perp s}^2\right) + 4g_2\ell\bar{k}_\perp\left(\bar{k}_\perp - \bar{k}_{\perp s}\right)\right]$ are the modified beam waist squared, gain, and phase, respectively. We have used the fact that terms containing $\alpha^2\ell^2$ are negligible. We may obtain the total energy of the amplified seed beam, $W_s(\ell)$ via

$$W_s(\ell) = \frac{2\pi}{Z_0}\int_{-\infty}^{\infty} d\Omega \int_0^\infty r\left|\widetilde{v}(\ell, r, \Omega)\right|^2 dr, \quad (90)$$

where Z_0 is the impedance of free space. Integration over radial coordinates is done with the approximation $q \approx w_r^2 + 2g_2\ell \equiv q_r$ (since $q_r \gg q_i \equiv 2\alpha\ell$) in the argument of J_0 in Eq. (89). The seed energy is reduced to an integration over Ω

$$W_s(\ell) = W_s(0) w_r \bar{k}_{\perp s}\tau_s \int_{-\infty}^{\infty} \Lambda(\Omega) e^{\Gamma(\Omega)\ell} e^{-\Psi(\Omega)} I_0[\Psi(\Omega)] f^2(\Omega) d\Omega, \quad (91)$$

where $W_s(0) = \pi I_s \tau_s w_r/\bar{k}_{\perp s}$ is the initial seed energy, and I_s is the peak seed intensity. Note that $W_s(\ell)/W_s(0)$ gives the seed pulse energy amplification. Further, $\Psi(\Omega) = 4^{-1}q_r^{-3}(Q_r|q|\bar{k}_{\perp s})^2$ and $\Lambda(\Omega) = q_r^{-1}Q_r$. As in the previous chapter, in order to find an analytical expression for $W_s(\ell)$, $\Gamma(\Omega)$ is Taylor expanded about Ω_s to second order, resulting in $\Gamma(\Omega) \approx \Gamma_s + \Gamma_s'(\Omega - \Omega_s) + 2^{-1}\Gamma_s''(\Omega - \Omega_s)^2$, where the subscript ' indiciates differentiation with respect to Ω, and as usual, the subscript s denotes evaluation at the seed frequency. Using the above Taylor expansion, together with the approximations $\Lambda \approx \Lambda_s = 1$ and $e^{-\Psi(\Omega)} I_0[\Psi(\Omega)] \approx (2\pi\Psi_s)^{-1/2} = \left(2^{-1}\pi q_r \bar{k}_{\perp s}^2\right)^{-1/2}$, the integration over Ω may be performed

in Eq. (91), with the result

$$W_s(\ell) \approx W_s(0)\frac{\tau_s}{\tau_g}\frac{w_r}{\sqrt{q_r}}\exp\left[\Gamma_s\ell + \frac{(\Gamma_s'\ell)^2}{2\tau_g^2}\right], \tag{92}$$

where $\tau_g = \sqrt{\tau_s^2 - \Gamma_s''\ell}$ is the transform-limited, gain-modified $1/e^2$ temporal duration. A

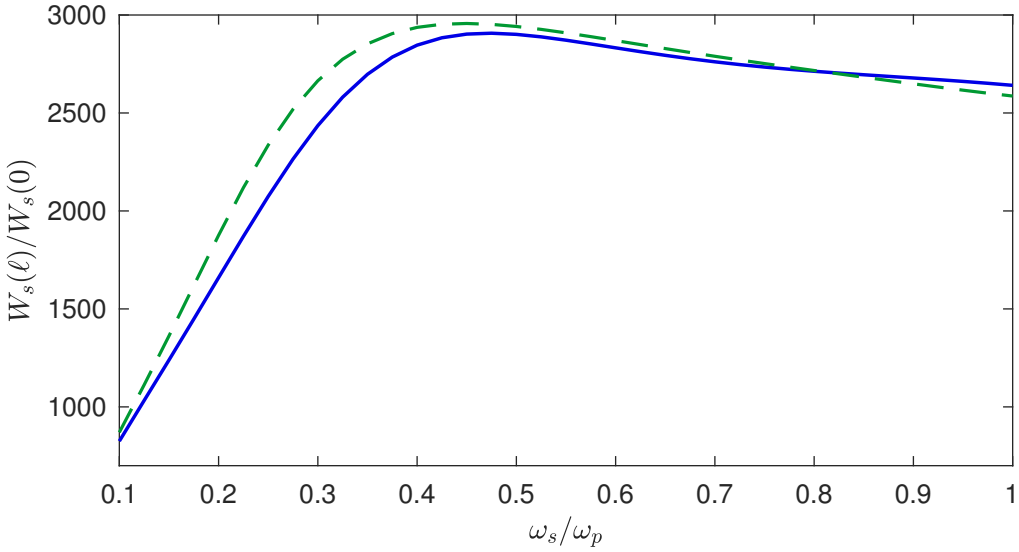

Figure 18: Comparing seed energy amplification in CaF_2 using both Eq. (91) (green dashed line) and Eq. (92) (blue solid line). Optical properties are as described in section 2.4. The pump wavelength and peak intensity are chosen to be 800 nm and 50 TW/cm^2, respectively. The propagation length is chosen to be $\ell = 8/\bar{g}$, and the initial seed beam waist $w_r = 5\ell\sqrt{2n_n/n}/3$ is chosen such that the desired (plane wave) amplification of $e^8 \approx 3000$ is obtained at $\ell_{sf}/5$, with ℓ_{sf} the critical self-focusing distance of the pump beam [1]; the factor of 1/3 arises from assuming the seed beam waist to be 1/3 of the pump beam waist (see Chapter 3). Finally, $\tau_s = 1/\nu_s$ for each seed frequency ν_s.

comparison between Eqs. (91) and (92) was done numerically, see Fig. 18. Over the entire range of seed frequencies considered, there is good agreement between the two curves, which justifies the use of Eq. (92). The actual pulse duration, $\tau_s(\ell)$, and the spatio-temporal profile of the amplified seed must be obtained numerically by means of Eq. (89). Note that $\tau_g(\ell) = \tau_s(\ell)$ if spectral chirp is neglected. Next, we compare amplification of Bessel-Gaussian and Gaussian seed beams quantitatively to explore the extent to which Bessel-Gaussian beams may present an advantage over ordinary Gaussian beams.

5.2 Comparing Gaussian and Bessel-Gaussian beams

The case of Gaussian seed beams was done in Chapter 4. For easier comparison of the results of the two cases, we summarize the results in Table 1. The main difference between these two initial profiles is the radial symmetry in Bessel-Gaussian beam, which means

that amplification takes place for a cone of wavevectors $\bar{k}_{\perp s}$ due to $J_0(\bar{k}_{\perp s}r)$ instead of only along the line $y = 0$ due to $\exp\left(i\bar{k}_{\perp s}x\right)$ for the Gaussian seed (see row 1). In k-space, this translates to amplification in a ring (independent of $\tilde{\theta}$) with radius $\bar{k}_{\perp s}$ for the Bessel-Gauss beam, whereas only at a point $(k_x = \bar{k}_{\perp s}, k_y = 0)$ for the Gaussian beam. Furthermore, the radial symmetry results in no shift in seed center, see x_c for the asymmetric Gaussian seed (see row 4, column 3). As a result, there is no walk-off between seed and pulse centers along the interaction length, so peak-to-peak amplification is maintained throughout the propagation. In the case of the Gaussian beam, the effecive area of the initial seed must account for x_c.

	Bessel-Gaussian	Gaussian
1. Initial profile $\varepsilon(0,x,y,t)$	$E_s \exp\left(-t^2/\tau_s^2 + i\Omega_s t\right) \times$ $\exp\left(-r^2/w_r^2\right) J_0\left(\bar{k}_{\perp s} r\right)$	$E_s \exp\left(-t^2/\tau_s^2 + i\Omega_s t\right) \times$ $\exp\left(-x^2/w_x^2 - y^2/w_y^2\right) \times$ $\exp\left(i\bar{k}_{\perp s} x\right)$
2. FT initial profile $\widetilde{v}(0,k_x,k_y,\Omega)$	$2^{-3/2} E_s w_r^2 \tau_s f(\Omega) \times$ $I_0\left(w_r^2 \bar{k}_{\perp s} k_\perp/2\right) \times$ $\exp\left[-w_r^2\left(k_\perp^2 + \bar{k}_{\perp s}^2\right)/4\right]$	$2^{-3/2} E_s w_x w_y \tau_s f(\Omega) \times$ $\exp\left(-w_y^2 k_y^2/4\right) \times$ $\exp\left[-w_x^2 (k_x - \bar{k}_\perp)^2/4\right]$
3. FT amplified profile $\widetilde{v}(\ell,k_x,k_y,\Omega)$	$\widetilde{v}(0,k_x,k_y,\Omega) \times$ $\exp\left(\bar{g}\ell/2 - i\sigma D_u \ell\right) \times$ $\exp\left[-g_2 \ell (k_\perp - \bar{k}_\perp)^2/2\right] \times$ $\exp\left[i\alpha\ell(k_\perp^2 - \bar{k}_\perp^2)/2\right]$	$\widetilde{v}(0,k_x,k_y,\Omega) \times$ $\exp\left(\bar{g}\ell/2 - i\sigma D_u \ell\right) \times$ $\exp\left[-g_2 \ell (k_x - \bar{k}_\perp)^2/2\right] \times$ $\exp\left[i\alpha\ell(k_\perp^2 - \bar{k}_\perp^2)/2\right]$
4. Spatiospectral profile $\widetilde{v}(\ell,x,y,\Omega)$	$w_r\sqrt{Q_r}/\sqrt{2q^2} \times$ $E_s \tau_s f(\Omega) \exp\left(\Gamma\ell/2 - i\varphi\right) \times$ $\exp\left(-r^2/q\right) J_0\left[Q_r \bar{k}_{\perp s} r/q\right]$	$w_x w_y/\sqrt{2q_x q_y} \times$ $E_s \tau_s f(\Omega) \exp\left(\gamma\ell/2 - i\varkappa\ell\right) \times$ $\exp\left[-\left(x - x_c\right)^2/q_x - y^2/q_y\right]$
5. Initial seed energy $W_s(0)$	$\pi I_s \tau_s w_r/\bar{k}_{\perp s}$	$(\pi/2)^{3/2} I_s \tau_s w_x w_y$
6. Energy amplification $W_s(\ell)/W_s(0)$	$\tau_s w_r/[\tau_g(\ell)\sqrt{q_r}] \times$ $\exp\left\{\Gamma_s \ell + (\Gamma'_s \ell)^2/[2\tau_g^2(\ell)]\right\}$	$\tau_s w_x/[\tau_g(\ell)\sqrt{(q_{xr})}] \times$ $\exp\left\{\Gamma_{xs} \ell + (\Gamma'_{xs} \ell)^2/[2\tau_g^2(\ell)]\right\}$
7. Final seed beam waists	$w_r(\ell) = \lvert q\rvert/\sqrt{q_r}$	$w_{x,y}(\ell) = \lvert q_{x,y}\rvert/\sqrt{(q_{xr,yr})}$
8. Required initial seed beam waists	$w_r(0) = \sqrt{\pi/2} w_p^2 \bar{k}_{\perp s}/9$	$w_x(0) = \left[\left(w_p/3 - \lvert\xi_{cr}\rvert/2\right)^2 - 2g_2\ell\right]^{1/2}$ $w_y(0) = w_p/3$

Table 1: Comparing Bessel-Gaussian and Gaussian initial seed profiles. In column 1, FT stands for Fourier-transformed. Subscripts s and r denote evaluated at seed frequency and real component of, respectively. Note that Γ_x in column 3 is Γ with q_x instead of q for clarity; see Chapter 4 or Appendix for more detail on parameters used in column 3.

The following reltaionship between pump and seed applies for both seed cases. A plane

wave pump requires infinite energy and is not realizable in practice. However, if the effective pump beam area is large enough compared to the effective seed beam area (by about a factor of 9 [20]), we may treat the pump as approximately constant. As well, the pump beam should be wide enough to avoid self-focusing as discussed in Chapter 3. The critical self-focusing length is given by $\ell_{sf} = w_p\sqrt{n_p/(2n_n)}$ [1]. Further, we desire amplification of roughly $e^8 \approx 3000$, so we set $\ell = 8/\bar{g}$. Putting this all together yields for the pump width, $w_p = 40\sqrt{2n_n/n_p}/\bar{g}$. In each case, we assume the seed to be Gaussian in time, see Table 1. Similar to above, and as in Chapter 3, we require the pump pulse duration to be a factor of 3 larger than the seed pulse duration. Thus, we require $\tau_p = 3\left(\tau_s(\ell) + |\Delta\beta_1|\ell/2\right)$, where $|\Delta\beta_1|$ is the group velocity walk-off between pump and seed beams, which, together with $\tau_s(\ell)$ is calculated numerically from Eq. (89). As a result, we have the minimum pump energy for KIA to operate efficiently as $W_p = (\pi/2)^{3/2} I_p \tau_p w_p^2$, for given peak pump intensity, I_p, assuming a radially symmetric Gaussian pump beam.

For the case of the Gaussian seed, we require the pump beam width to be a factor of 3 larger than each width of the seed. For the $y-$dimension, we require simply $w_y(\ell) \approx w_y = w_p/3$. For the $x-$dimension, we require $w_p = 3(w_x(\ell) + |\xi_{cr}|/2)$, where $\xi_{cr} = x_{cr} + x_{ci}q_{xi}/q_{xr}$, is the modified spatial walk-off of the intensity profile of the amplified seed (see below Eq. (75)). The factor $1/2$ comes from the assumption that the pump and seed beam centers are aligned at half of the material length. This relation may be rearranged to find the initial seed width for a given seed frequency. In summary, for both w_x and w_y we have

$$w_x = \left[\left(\frac{w_p}{3} - \frac{|\xi_{cr}|}{2}\right)^2 - 2g_2\ell\right]^{1/2} \tag{93a}$$

$$w_y = \frac{w_p}{3}, \tag{93b}$$

where we have $q_{xr}^2 \gg q_{xi}^2$. When $(w_p/3 - |\xi_{cr}|/2)^2 = 2g_2\ell$, the KIA regime is terminated for the Gaussian seed, as we require $w_x = 0$. The influence of the walk-off and the finite gain profile increase with increasing detuning from the pump $|\omega_s - \omega_p|$. Therefore, when $|\omega_s - \omega_p|$ becomes large enough, the KIA regime is terminated.

Now, we consider the case of the Bessel-Gaussian seed. The main advantage of the Bessel-Gaussian seed is the absence of the walk-off ξ_{cr} due to radial symmetry, so KIA may be achieved over a larger frequency range. As well, the initial effective seed beam area may be larger in the Bessel-Gaussian case since the pump beam area does not have to compensate for both the seed beam effective area and walk-off. A larger initial seed beam area relative to the same pump area results in larger amplified seed energy for given pump energy, increasing efficiency. Specifically, for a Gaussian pump beam, the effective area of the transverse intensity profile is given by $A_p = (\pi/2)w_p^2$. The effective area of the transverse intensity profile

of the amplified Bessel-Gaussian seed (see Eq. (89)) is given by $A_s = (2\pi)^{1/2}\bar{k}_{\perp s}^{-1} q_r^{-1/2} w_r^2/4$. By requiring $A_s = A_p/9$, the initial width w_r necessary for a given seed frequency may be obtained. The result is

$$w_r = \frac{\sqrt{\pi}}{9} w_p^2 \bar{k}_{\perp s} \left(1 + \sqrt{1+b}\right)^{1/2} \approx \sqrt{2\pi}\frac{w_p^2}{9}\bar{k}_{\perp s}, \tag{94}$$

where $b = 648 g_2 \ell/(\pi w_p^4 \bar{k}_{\perp s}^2) \ll 1$.

5.3 Quantitative analysis using CaF_2

As a numerical example of KIA for a Bessel-Gaussian seed pulse, we choose CaF_2 to compare to the work done in Chapter 3. For convenience, we display Fig. (20) in this section as well.

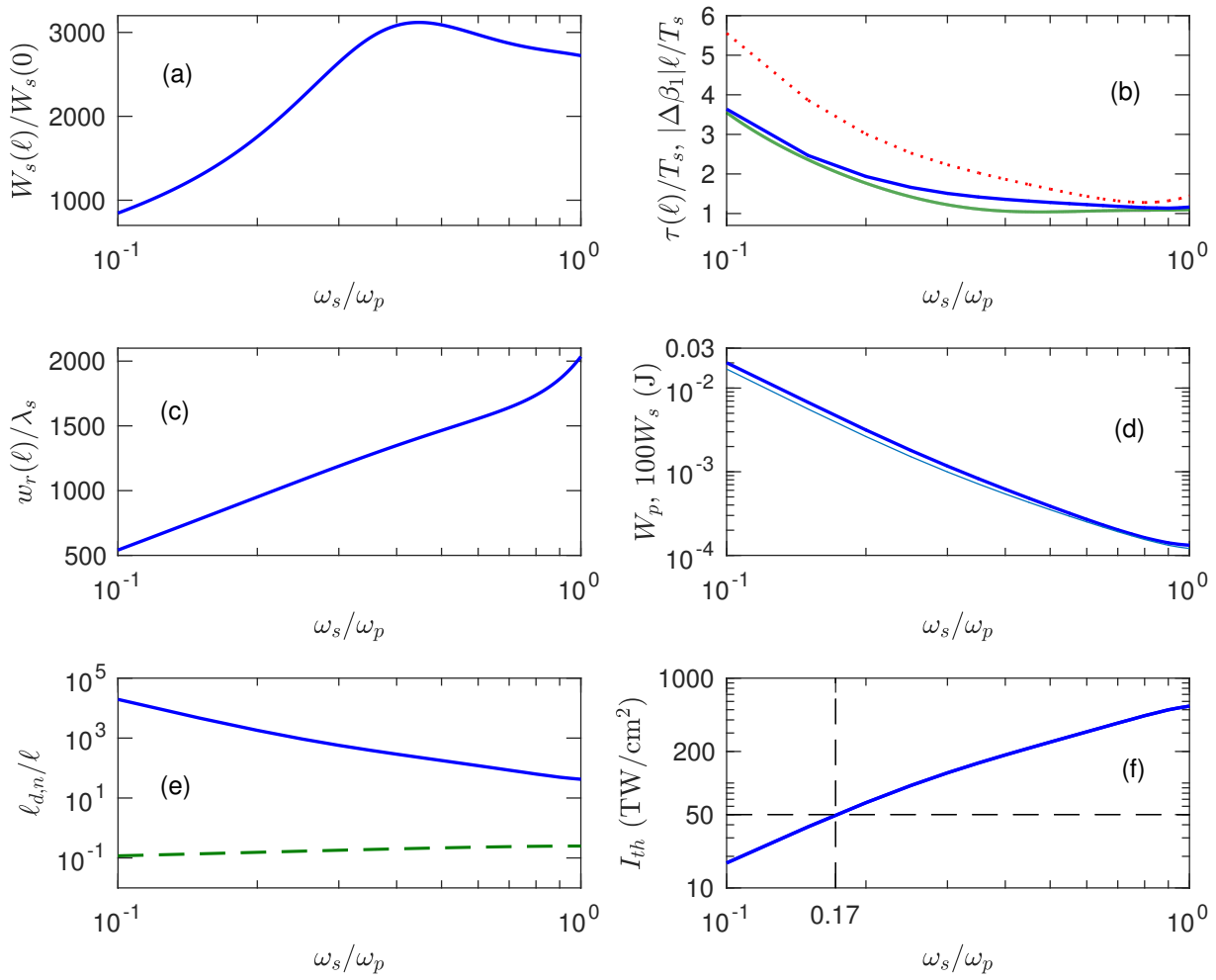

Figure 19: KIA of single cycle Bessel-Gaussian beam $\tau(0) = T_s = 2\pi/\omega_s$ in CaF_2; $n_2 = 2\times10^{-16}$ cm^2/W; pump peak intensity $I_p = 50$ TW/cm^2, pump wavelength $\lambda_p = 0.85\,\mu$m, amplifier length $l = 8/\bar{g}$; pump beam radius determined as in Fig. (18) and duration, τ_p, determined from the condition stated below Eqs. (93) initial seed beam radius, w_r is determined by Eq. (94). (a) Seed pulse energy increase $W_s(l)/W_s(0)$ from Eq. (92) versus ω_s/ω_p (seed over pump frequency). (b) amplified seed pulse duration $\tau(l)/T_s$ (blue full); transform limited amplified seed pulse duration $\tau_g(l)/T_s$ defined above Eq. (77) (green, dashed), and group velocity walk off between pump and seed, $|\Delta\beta_1|l/T_s$, versus ω_s/ω_p (red, dotted). (c) amplified seed beam radius $w_r(l)/\lambda_s$. (d) Minimum required pump energy W_p (blue, full), see text above Eq. (78), and corresponding seed energy (multiplied by 100) $W_s(l)$ (light blue, thin) versus ω_s/ω_p. (e) dispersive length l_d/l (blue, full) and nonlinear length l_n/l (green, dashed) versus ω_s/ω_p. (f) Damage threshold intensity I_{th} versus ω_s/ω_p; dashed lines indicate $I_p = I_{th}$.

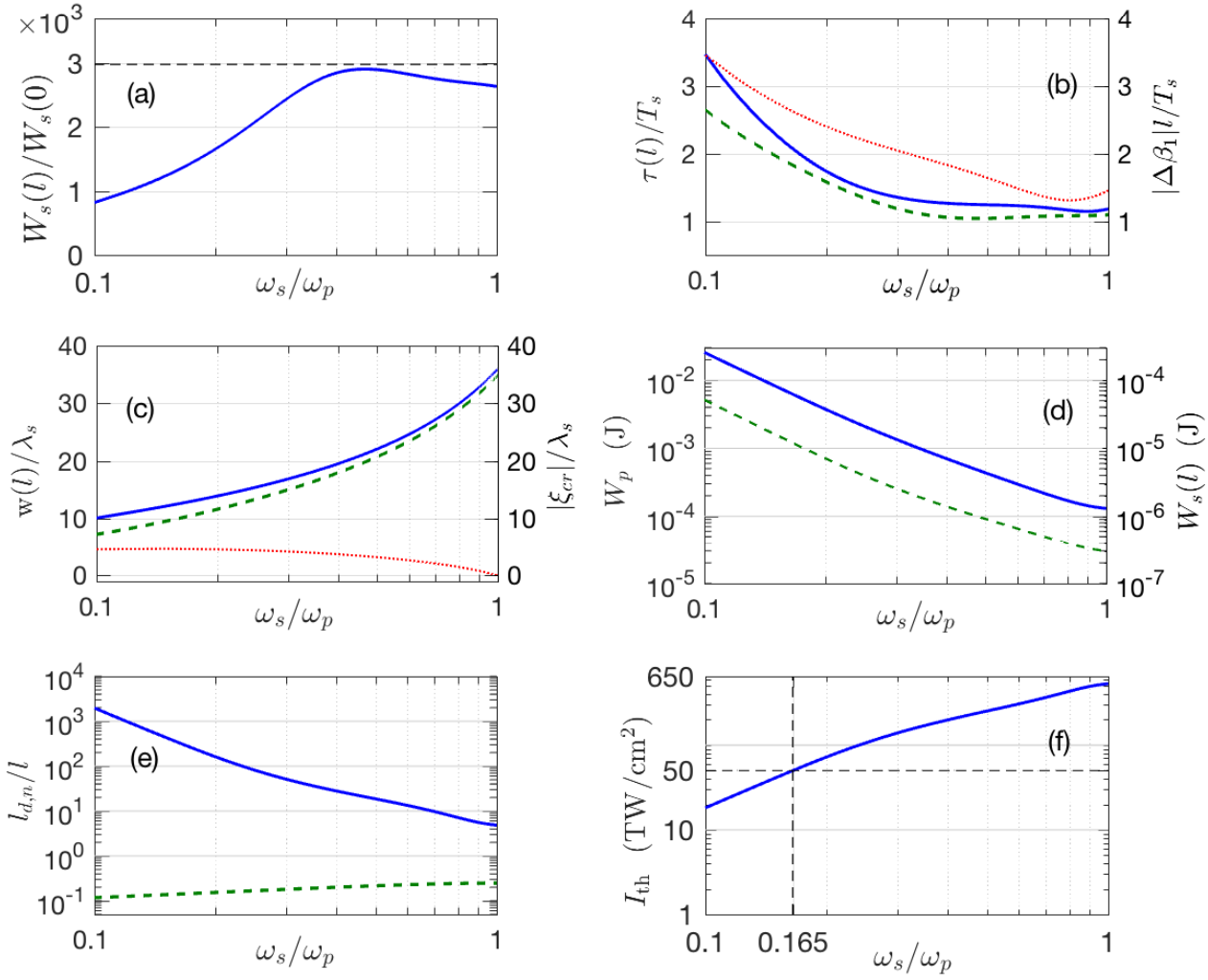

Figure 20: KIA of single cycle Gaussian beam in CaF_2, parameters identical to Fig. (19). Initial seed beam radii, $w_x(0) = w_y(0)$, are determined from Eq. (93). (a) Seed pulse energy increase $W_s(l)/W_s(0)$ from Eq. (77) versus ω_s/ω_p (seed over pump frequency); black dashed line corresponds to the cw limit $\exp(\bar{g}l) = \exp(8) \approx 3000$. (b) amplified seed pulse duration $\tau(l)/T_s$ (blue full); transform limited amplified seed pulse duration $\tau_g(l)/T_s$ defined above Eq. (77) (green, dashed), and group velocity walk off between pump and seed, $|\Delta\beta_1|l/T_s$, versus ω_s/ω_p (red, dotted). (c) amplified seed beam radii $w_x(l)/\lambda_s$ (blue, full) and $w_y(l)/\lambda_s$ (green, dashed) versus ω_s/ω_p; initial beam radius is not plotted as $w_y(l) \approx w_x(0) = w_y(0)$; shift of seed beam center $|\xi_{cr}|$ defined below Eq. (76) (red dotted). (d) Minimum required pump energy W_p (blue, full), see text above Eq. (78), and corresponding seed energy $W_s(l)$ (green, dashed) versus ω_s/ω_p. (e) dispersive length l_d/l (blue, full) and nonlinear length l_n/l (green, dashed) versus ω_s/ω_p. (f) Damage threshold intensity I_{th} versus ω_s/ω_p; dashed lines indicate $I_p = I_{th}$.

The results in Fig. (19) compared to Fig. (20) show that there are only a few noticeable differences. Firstly, comparing panel (b) in each figure, it's clear that the regular Gaussian beam is slightly more favourable for maintaining temporal duration of the amplified pulses deeper into the infrared. However, as discussed above, there is a limit to how far into the

infrared the regular Gaussian beam may be amplified due mainly to the spatial walk-off between the pump and seed. In panel (c) for each figure, it's clear that the Bessel-Gauss beam only requires one parameter to describe the transverse width of the beam, due to the symmety of Bessel beams. In the case of the Gaussian beam, we are required to specify in this case widths along both the $x-$ and $y-$directions, as well as the transverse walk-off that is present. In panel (d) for each figure, the efficiency of the Bessel-Gauss seed is clearly higher than the Gaussian case, around 1% as opposed to around 0.17% in the Gaussian case.

In summary, the main advantages of Bessel-Gaussian seed pulses is their radial symmetry, which can align with the amplification profile about a ring in k-space, allowing for pump-to-seed energy amplification that is more efficient than the Gaussian case by a factor of about $5-7$. Whereas in the Gaussian case, the efficiency is on the order of about $0.15-0.2\%$, in the Bessel-Gaussian case it is on the order of about 1%. However, in comparing Figs. (19) and (20), the regular Gaussian seed is slightly more favourable for maintaining pulse duration over its accessible amplification regime.
Spatial walk-off between the maxima of the pump and seed beams for the Gaussian seed pulse significantly reduces the initial width along the dimension of the walk-off. Eventually, when this walk-off, together with the finite amplification profile, matches the width available from the pump, amplification is no longer possible, see below Eq. (93). The symmetry of the Bessel-Gaussian profile results in no spatial walk-off, and hence amplification at longer wavelengths than in the Gaussian case is theoretically possible. Lastly, Bessel-Gauss beams are known to have favourable properties, such as being diffraction-free beams over limited propagation lengths [50]. We can conclude that it can be advantageous to use Bessel-Gaussian seed beams for KIA.

6 Quantum Optical Kerr Instability Amplification

In this chapter, the quantum optical theory of Kerr instability is developed. In section 6.1, the quantum optical analog of the linearized perturbation equations of Eq. (61) will be derived. A solution for the propagation of the annihilation and creation operators in the Heisenberg picture is obtained. Subsequently, a comparison to quantum OPA theory is made to establish the connection between Kerr instability and four-wave mixing quantum optically, similarly to the classical case.

In section 6.2, a coherent state is subjected to Kerr instability amplification and the resulting quantum state is explored. Then, in section 6.3, the photon statistics of each coupled mode is explored.

Finally, in sections 6.4 and 6.5, the theory of the generation of ultrashort pairs of photons from quantum vacuum is explored.

6.1 Quantized perturbation equations

In this section, the quantized Heisenberg equations of motion for the perturbation and its conjugate will be derived. We begin with the scalar wave equations from Eqs. (61),

$$\left[\left(\frac{\partial}{\partial_z} - ik_p\right)^2 + k_z^2\right]\widetilde{v}_x = -k_n^2\widetilde{v}_{x(-)}^* \tag{95a}$$

$$\left[\left(\frac{\partial}{\partial_z} + ik_p\right)^2 + k_{z(-)}^2\right]\widetilde{v}_{x(-)}^* = -k_{n(-)}^2\widetilde{v}_x. \tag{95b}$$

In Chapter 2, it was determined that the dominant wavevector solution for the perturbation equations was given by $K \approx \pm\sigma D_u$, as verified in appendix A. To proceed, we use the ansatz $\widetilde{v}_x = \widetilde{w}_x e^{-i\sigma D_u z}$. The second-order scalar wave equations may be transformed to first-order scalar wave equations by using the Slowly Evolving Wave Approximation (SEWA) [55]. Here, the SEWA states that $|2\sigma D_u \widetilde{w}_x| \gg |\partial\widetilde{w}_x/\partial_z|$ so we can neglect the second-order derivative in z and the propagation equations (95) become first-order.
In anticipation of quantizing the fields, we make the transformation $\widetilde{w}_x = \widetilde{a}e^{ik_p z + i\sigma D_u z}$. Further, due to nature of the coupling between $\widetilde{v}_x$ and $\widetilde{v}_{x(-)}^*$, the right side of both Eqs. (95a) and (95b) may be replaced by $-k_n k_{n(-)} e^{-2ik_p z}\widetilde{a}_{(-)}^*$ and $-k_n k_{n(-)} e^{2ik_p z}\widetilde{a}$, respectively. With all of the above, the resulting first-order propagation equations are written as

$$i\frac{\partial}{\partial_z}\widetilde{a} = \Delta k\widetilde{a} + \frac{\bar{g}}{2}e^{-2ik_p z}\widetilde{a}_{(-)}^* \tag{96a}$$

$$-i\frac{\partial}{\partial_z}\widetilde{a}_{(-)}^* = \Delta k_{(-)}\widetilde{a}_{x(-)}^* + \frac{\bar{g}}{2}e^{2ik_p z}\widetilde{a}, \tag{96b}$$

where $\Delta k = k_p + \sigma D_u - (k_\perp^2 - \kappa_\perp^2)/(2(k_p + \sigma D_u))$, and $\bar{g} = k_n k_{n(-)}/\sqrt{k_p^2 - \sigma^2 D_u^2}$ is the maximum intensity gain from the KIA process; all parameters are the same as derived in Chapter 2. Note that we consider the pump to be a classical coherent state, consistent with the parametric approximation as discussed in Chapter 1.

Typically, the Hamiltonian is sought [28,56,57], which is the generator for time evolution [56], which corresponds to seeking the time-dependent quantum optical formalism. In other words, it is typical to seek either the time-dependent wavefuntion in the Schrodinger picture, or time evolution of the relevant operator, in this case, the annihilation operator in the Heisenberg picture. However, since there is dispersion in the nonlinear material which strongly influences the instability, the usual time-dependent approach to quantizing the Kerr instability is not easily done. Alternatively, as is similarly done in Ref. [56], in order to quantize Eqs. (96), the momentum operator, $\hat{G}$, can be obtained, which is the generator for space propagation [56]. Using $\hat{G}$ in the Heisenberg equation of motion results in a propagation equation for the annihilation operator [56]. Formally, $\hat{G}$ is defined as the normally-ordered operator [56]

$$\hat{G}(z) = \int_T \int_A \left[\hat{D}^{(-)}(\mathbf{x},t)\hat{E}^{(+)}(\mathbf{x},t) + \text{H.c.}\right] dt d\mathbf{A}, \tag{97}$$

where integration is over the period, T, and cross-sectional area, A, discussed below Eq. (98). Further, $\hat{E}(\mathbf{x},t) = \hat{E}^{(+)}(\mathbf{x},t) + \hat{E}^{(-)}(\mathbf{x},t)$ is the total quantized electric field in a dielectric medium [56]. Further, $\hat{D}(\mathbf{x},t) = \epsilon_0 \hat{E}(\mathbf{x},t) + \hat{P}(\mathbf{x},t)$, where $\hat{P}(\mathbf{x},t)$ is the polarization operator of the medium, containing both linear ($\chi^{(1)}$) and nonlinear ($\chi^{(3)}$) terms, see the classical version in Eq. (1). The formal approach using Eq. (97) to find $\hat{G}$ applies the quantization procedure to the total electric field, and not just the perturbation. However, here we treat the pump classically, and linearize the perturbation, so using the approach in Eq. (97) is overly-cumbersome. Equivalently, we can find the operator, $\hat{G}$, such that we obtain the quantized version of the first-order propagation equation of Eq. (96a) via the Heisenberg equation of motion [56, 57]:

$$i\hbar \frac{\partial \hat{a}_\Omega}{\partial_z} = \left[\hat{a}_\Omega, \hat{G}(z)\right], \tag{98}$$

where $\hat{a}_\Omega(z) \equiv \hat{a}(\Omega, k_x, k_y, z)$ is the operator corresponding to the classical counterpart, $\widetilde{a}(\Omega, k_x, k_y, z)$, with $\Omega = \omega - \omega_p$. Here, $\hat{a}_\Omega(z)$ is in the (Ω, k_x, k_y) mode and $\hat{a}^\dagger_{-\Omega}(z) \equiv \hat{a}^\dagger(-\Omega, -k_x, -k_y, z)$ is the operator equivalent to $\widetilde{a}^*(-\Omega, -k_x, -k_y, z)$, in the $(-\Omega, -k_x, -k_y, z)$ mode. As is typically done [28, 56, 57], the quantization is performed in terms of discrete modes (Ω, k_x, and k_y). Here, analogous to Ref. [56], we quantize for a given period, T, and cross sectional area of length L, $A = L^2$. Therefore, instead of quantizing the field in a large box of volume $V = L^3$, and demanding $3-D$ spatial periodicity, we assume time periodicity T of the field, and transverse $2-D$ spatial periodicity with A. Then, instead of writing the field in terms of 3 spatial modes, we write it in terms 2 transverse spatial modes and 1 temporal mode, corresponding to a discrete Fourier analysis for $\omega = 2\pi j/T$ and $k_x = 2\pi l/L$,

and $k_y = 2\pi m/L$ for integers j, l, m. Note that T and A should be much larger than any other time or transverse area, and can be taken to be infinity when performing averages. Then, instead of sums over discrete modes, there are integrals over a continuum of modes, as will be shown below. In this analysis we choose to continue with the scalar approximation, neglecting the influence of polarization. Future work may be done to include a fully vectorial theory, but it is not done here.

Returning to the original ansatz of the perturbation on the pump electric field, the quantized version of the electric field of the perturbation, $\varepsilon(\mathbf{x}, t) \to \hat{\varepsilon}(\mathbf{x}, t)$, is written as

$$\hat{\varepsilon}(\mathbf{x}, t) = \sum_{\Omega, \vec{k}_\perp} \left[\frac{\hbar(\omega_p + \Omega)}{2\epsilon_0 c n (\omega_p + \Omega) A T} \right]^{1/2} \left[\hat{a}_\Omega(z) e^{i(\omega_p + \Omega)t + ik_x x + ik_y y} + \text{H.c.} \right] \equiv \hat{\varepsilon}^{(+)}(\mathbf{x}, t) + \hat{\varepsilon}^{(-)}(\mathbf{x}, t), \tag{99}$$

where the sum over Ω and $\vec{k}_\perp = (k_x, k_y)$ extends over the entire instability regime, which will be discussed further below. Eq. (99) is analogous to Ref. [56], except it is extended to include the transverse spatial dimensions. Recall that the pump is taken to be classical, as we assume it is in a strong, coherent state−i.e. the parametric approximation [28]. In order to find the momentum operator, and thus the Heisenberg equation of motion from Eq. (98), we use the equal-space (for equal z) commutation relations (ESCR),

$$\left[\hat{a}_\Omega(z), \hat{a}^\dagger_{\Omega'}(z) \right] = \delta_{\Omega, \Omega'}, \tag{100a}$$

$$[\hat{a}_\Omega(z), \hat{a}_{\Omega'}(z)] = \left[\hat{a}^\dagger_\Omega(z), \hat{a}^\dagger_{\Omega'}(z) \right] = 0, \tag{100b}$$

where, as in Eq. (98) and for the subsequent work below, Ω is short-hand notation for the mode $(\Omega, \vec{k}_\perp)$. Eqs. (100) must be enforced when evaluating Eq. (98) according to the proper quantization procedure [56, 57]. The momentum operator that yields the quantized version of Eq. (96a) when inserted into Eq. (98) and by using the ESCR is found to be

$$\hat{G}(z) = \hbar \sum_{\Omega, \vec{k}_\perp} \left[\Delta k_\Omega \hat{a}^\dagger_\Omega \hat{a}_\Omega + \frac{\bar{g}_\Omega}{4} \left(e^{-2ik_p z} \hat{a}^\dagger_\Omega \hat{a}^\dagger_{-\Omega} - \text{H.c.} \right) \right], \tag{101}$$

where $\Delta k_\Omega \equiv \Delta k(\Omega, k_x, k_y)$ is a wavevector mismatch, and $\bar{g}_\Omega \equiv \bar{g}(\Omega)$ is the maximum instability gain, both defined below Eqs. (96). Note that $\bar{g}_{-\Omega} = \bar{g}_\Omega$. The physical interpretation of Eq. (101) is the following: the first term is the number of photons in mode $(\Omega, \vec{k}_\perp)$ with momentum $\hbar \Delta k_\Omega$. The second and third terms are brought about by the maximum instability gain, $\bar{g}$. The second term creates a pair of photons, one in the $(\Omega, \vec{k}_\perp)$ mode and the other in the $(-\Omega, -\vec{k}_\perp)$ mode, with momentum $\hbar \bar{g}_\Omega e^{-2ik_p z}/4$. The third term destroys a pair of photons, one in the $(\Omega, \vec{k}_\perp)$ mode and the other in the $(-\Omega, -\vec{k}_\perp)$ mode, with momentum $\hbar \bar{g}_\Omega e^{2ik_p z}/4$. The total momentum operator is obtained by summing over all possible modes

$(\Omega, \vec{k}_\perp)$. The quantized version of Eq. (96a) for a single set of modes $(\Omega, \vec{k}_\perp)$ is found by inserting Eq. (101) into Eq. (98) and by using the ESCR of Eqs. (100),

$$i\frac{\partial}{\partial z}\hat{a}_\Omega = \Delta k_\Omega \hat{a}_\Omega + \frac{\bar{g}_\Omega}{2} e^{-2ik_p z}\hat{a}^\dagger_{-\Omega}. \tag{102}$$

The quantized version of Eq. (96b) is obtained by taking the Hermitian conjugate of Eq. (102) and letting $(\Omega, \vec{k}_\perp) \to (-\Omega, -\vec{k}_\perp)$,

$$-i\frac{\partial}{\partial z}\hat{a}^\dagger_{-\Omega} = \Delta k_{-\Omega}\hat{a}^\dagger_{-\Omega} + \frac{\bar{g}_\Omega}{2} e^{2ik_p z}\hat{a}_\Omega. \tag{103}$$

6.2 Kerr instability amplification of coherent and vacuum states

In this section, we first derive the evolution of $\hat{a}_\Omega(z)$ by solving Eqs. (102) and (103). As well, since the coherent state is an eigenstate of the annihilation operator, we show that a certain case of the two-mode squeezed [28] coherent state remains an eigenstate of $\hat{a}_\Omega(z)$. This is a generalization of the Two-Mode Squeezed Vacuum (TMSV) state in that it is grown out of a coherent state seed pulse in the $(\Omega, \vec{k}_\perp)$ mode. We derive this eigenstate in the photon number basis.

To begin, we insert $\hat{a}^\dagger_{-\Omega}$ from Eq. (102) into Eq. (103), a second-order propagation equation for $\hat{a}_\Omega$ alone is obtained. The solution is

$$\hat{a}_\Omega(z) = \left[\mu\hat{a}_\Omega(0) + \nu\hat{a}^\dagger_{-\Omega}(0)\right] e^{-ik_p z + iK_u z}, \tag{104}$$

$$\mu = \cosh\left(\frac{gz}{2}\right) - i\frac{k_p(k_\perp^2 - \kappa_\perp^2)}{g(k_p^2 - \sigma^2 D_u^2)}\sinh\left(\frac{gz}{2}\right), \tag{105}$$

$$\nu = -i\frac{\bar{g}}{g}\sinh\left(\frac{gz}{2}\right), \tag{106}$$

valid for the entire instability range, which is the regime of interest. That is, $k_\perp = \sqrt{k_x^2 + k_y^2}$ spans from $\sqrt{\kappa_\perp^2 - \delta_\perp^2}$ to $\sqrt{\kappa_\perp^2 + \delta_\perp^2}$, and Ω spans the entire spectral range from $-\omega_p$ to ω_p. All frequency-dependent functions are precisely the same as from the classical KIA theory derived in Section 2.2, see Eq. (55) for $\kappa_\perp$, Eq. (53) for $\delta_\perp^2$, and Eqs. (52) for odd dispersive terms, K_u, and intensity gain, $g = 2\mathrm{Im}(K_g)$. These Ω and $k_\perp$-dependent functions correspond to mode $(\Omega, \vec{k}_\perp)$; the indices on all functions are suppressed to ease notation. Note that

$$|\mu|^2 - |\nu|^2 = 1, \tag{107}$$

which will be used to simplify the results derived below.

6.2.1 Reduction to the Hamiltonian approach and comparison to quantum OPA theory

There is a set of transverse wavevectors that maximizes the instability, $k_\perp = \kappa_\perp$, where $g_\Omega(\kappa_\perp) = \bar{g}_\Omega$. To examine a limiting case of Eq. (104), we consider one of the transverse momenta fulfilling this relation to maximize the instability. As well, consider the plane wave limit for the single frequency, ω_s. In this dispersionless limit, there is an equivalence between propagation distance and propagation time; that is, $z = ct/n_s$, where $n_s = n(\omega_s)$. By multiplying the momentum operator, $\hat{G}$, by c/n_s, and replacing $z = ct/n_s$, we obtain the time-dependent Hamiltonian operator, $\hat{H} = c\hat{G}/n(\omega_s)$, found to be

$$\hat{H}(t) = \hbar\Delta\omega\hat{a}^\dagger_{\Omega_s}(t)\hat{a}_{\Omega_s}(t) + \hbar\frac{\omega_n}{2}\left(e^{-2i\frac{n_p}{n_s}\omega_p t}\hat{a}^\dagger_{\Omega_s}(t)\hat{a}^\dagger_{-\Omega_s}(t) - \text{H.c.}\right), \tag{108}$$

where $\Omega_s = \omega_s - \omega_p$, $\Delta\omega = \Omega_s + n_p/n_s\omega_p$, and $\omega_n = n_n\sqrt{\omega_p^2 - \Omega_s^2}/(2n_p n_s)$. The Heisenberg equation of motion may be found by means of inserting Eq. (108) into the limiting case of Eq. (98) for $\hat{H}$, and $z = ct/n(\omega_s)$,

$$i\hbar\frac{\partial}{\partial_t}\hat{a}_{\Omega_s}(t) = \left[\hat{a}_{\Omega_s}(t), \hat{H}(t)\right]. \tag{109}$$

The time evolution of the $\hat{a}_{\Omega_s}(t)$ is found by solving Eq. (109), analogously to Eq. (102). The result is

$$\hat{a}_{\Omega_s}(t) = \left(\cosh(r)\,\hat{a}_{\Omega_s}(0) - e^{i\phi}\sinh(r)\,\hat{a}^\dagger_{-\Omega_s}(0)\right)e^{-i\omega_s t - i\frac{n_p}{n_s}\omega_p t}, \tag{110}$$

where $r = |\omega_n|t$ and ϕ is a constant phase between the pump and perturbation which we have chosen to factor out explicitly here, as is customary for states related to two-mode squeezing [28]. Eq. (110) represents the two-mode squeezed state result, for example, see Ref. [28]. Note that the overall phase factor of $\omega_s t + n_p\omega_p t/n_s$ is contained in the solution of Eq. (110) because we used the full Hamiltonian for completeness in solving the Heisenberg equation of motion, instead of just the slowly varying interaction (second and third) terms of the Hamiltonian found in Eq. (109). If one considers only the slowly varying component contained within the brackets of Eq. (110), and make the identifications $\hat{a}_{\Omega_s}(0) \equiv \hat{a}^\dagger(0)$, $\hat{a}^\dagger_{-\Omega_s}(0) \equiv \hat{b}^\dagger(0)$, $|\omega_n| \equiv |\gamma|^2\Omega^{(3)}$, and $\phi \equiv \theta$, a comparison to the OPA result of Section 1.2 may be made. Specifically, the result of Eq. (110) is equivalent to Eq. (10). Therefore, it is clear that the solution from quantum optical Kerr instability found in Eq. (104) is the generalization to quantum optical Four-Wave Optical Parametric Amplification (FWOPA), extended to include the transverse spatial dimensions, and over a wide spectral range, $-\omega_p \leq \Omega < \omega_p$; analogous to the classical case. Therefore, there is a correspondence between Kerr instability amplification and OPAs in both the classical and quantum optical regimes.

6.2.2 General momentum operator approach

We continue with the general solution of Eq. (104), and seek the wavefunction in the number state basis that results from Kerr instability amplification of a coherent state in the $(\Omega, \vec{k}_\perp)$ mode and vacuum in the $(-\Omega, -\vec{k}_\perp)$ mode. It will be shown to have the form of a two-mode squeezed coherent state. As well, we may set the coherent state amplitude to zero to study Kerr instability amplification of the two-mode vacuum state. It will be shown to be a two-mode squeezed vacuum state.

To begin, we seek the state $|\alpha, \xi, z\rangle$ such that $\hat{a}_\Omega(z)|\alpha, \xi, z\rangle = \alpha_\Omega|\alpha, \xi, z\rangle$, where α_Ω is the eigenvalue for mode $(\Omega, \vec{k}_\perp)$, and ξ will be defined below. The state, $|\alpha, \xi, z\rangle$, is in the Schrodinger picture, where $\hat{a}_\Omega(z)$ corresponds to the Heisenberg picture. The unitary propagator, $\hat{U}(z)$, acts on the initial state $|\alpha, \xi, z = 0\rangle$ to create the Kerr amplified state after it propagates in the material a distance z. That is, $|\alpha, \xi, z\rangle = \hat{U}(z)|\alpha, \xi, z = 0\rangle$, where the propagator $\hat{U}(z)$ is satisfies the Schrodinger equation,

$$i\hbar\frac{\partial}{\partial_z}\hat{U}(z) = \hat{G}(z)\hat{U}(z), \tag{111}$$

where $\hat{G}(z)$ is the momentum operator of Eq. (101). Eq. (111) has the general solution

$$\hat{U}(z) = \exp\left[-\frac{i}{\hbar}\int_0^z \hat{G}(z')dz'\right]. \tag{112}$$

Using Eq. (112), transforming between Schrodinger and Heisenberg pictures is formally done by means of $\hat{a}_\Omega(z) = \hat{U}(z)\hat{a}_\Omega(0)\hat{U}^\dagger(z)$. At $z = 0$,

$$\hat{a}_\Omega(0)|\alpha, \xi, z = 0\rangle = \alpha_\Omega|\alpha, \xi, z = 0\rangle, \tag{113}$$

therefore, $|\xi(0)\rangle$ corresponds to a coherent state in the $(\Omega, \vec{k}_\perp)$ mode and vacuum in the $(-\Omega, -\vec{k}_\perp)$ mode initially. By applying $\hat{U}(z)$ to Eq. (113) and using its unitarity, where $\hat{U}^\dagger(z)\hat{U}(z) = \hat{I}$ ($\hat{I}$ is the identity operator), we obtain

$$\begin{aligned}\hat{U}(z)\hat{a}_\Omega(0)\hat{U}^\dagger(z)\hat{U}(z)|\alpha, \xi, z = 0\rangle &= \alpha_\Omega\hat{U}(z)|\alpha, \xi, z = 0\rangle \\ \rightarrow \hat{a}_\Omega(z)|\alpha, \xi, z\rangle &= \alpha_\Omega|\alpha, \xi, z\rangle.\end{aligned} \tag{114}$$

To proceed in the Schrodinger picture, we expand $|\alpha, \xi, z\rangle$ in the number state basis with the ansatz (found by inspection to be convenient),

$$|\alpha, \xi, z\rangle = \sum_{n,k} h_{n,k}(-\xi)^n\tilde{\alpha}^k|n + k, n\rangle, \tag{115}$$

where the indices n, k run from $0 \rightarrow \infty$, and we use the convention that $|n + k, n\rangle \equiv |n + k\rangle_\Omega|n\rangle_{-\Omega}$; the first part of the ket will always be mode $(\Omega, \vec{k}_\perp)$, and the second, $(-\Omega, -\vec{k}_\perp)$.

We have defined

$$\xi = \frac{\nu}{\mu} e^{i\varphi} \tag{116}$$

$$\tilde{\alpha} = \frac{\alpha}{\mu} e^{ik_p z - iK_u z}, \tag{117}$$

where ξ and $\tilde{\alpha}$ characterize the squeezed part and coherent part of the state, respectively. Further, $h_{n,k}$ and φ are to be determined[2]. Applying $\hat{a}_\Omega(z)$ from Eq. (104) on $|\alpha, \xi, z\rangle$ from Eq. (115) yields the recursion relation for $h_{n,k}$,

$$\sqrt{n+k}\; h_{n,k} = \sqrt{n}\; h_{n-1,k} + h_{n,k-1}, \tag{118}$$

which has the solution,

$$h_{n,k} = \mathcal{N} \frac{\sqrt{(n+k)!}}{\sqrt{n!}\; k!}, \tag{119}$$

where $\mathcal{N}$ is a constant to be determined by the normalization requirement $\langle \xi(z) | \xi(z) \rangle = 1$. It is found to be

$$\mathcal{N} = \frac{1}{|\mu|} \exp\left[-\frac{|\alpha|^2}{2} \right]. \tag{120}$$

Therefore, the eigenstate for the quantized KIA process is

$$|\alpha, \xi, z\rangle = \frac{1}{|\mu|} \exp\left[-\frac{|\alpha|^2}{2} \right] \sum_{n,k} \frac{\sqrt{(n+k)!}}{\sqrt{n!}\, k!} (-\xi)^n \tilde{\alpha}^k |n+k, n\rangle. \tag{121}$$

In the limit where the eigenvalue $\alpha = 0$, then $\tilde{\alpha} = 0$, and only the $k = 0$ term survives which corresponds to the two-mode vacuum state initially; $|\alpha = 0, \xi, z = 0\rangle \to |0\rangle$. In this limit, Eq. (121) becomes

$$|\alpha = 0, \xi, z\rangle \equiv |\xi, z\rangle = \frac{1}{|\mu|} \sum_n (-\xi)^n |n, n\rangle, \tag{122}$$

which has the form of the two-mode squeezed vacuum state (TMSV) [28]. In order to find φ which is contained in ξ (see Eq. (116)), we require consistency between the Heisenberg and Schrodinger pictures in calculating expectation values, as they must be equivalent. For example, we must have $\langle 0 | \hat{a}_\Omega(z) \hat{a}_{-\Omega}(z) | 0 \rangle = \langle \xi, z | \hat{a}_\Omega(0) \hat{a}_{-\Omega}(0) | \xi, z \rangle$. Using Eqs. (104)−(106),

[2]In this procedure, there is ambiguity as to the phase, φ, specifically, in the case of the perturbation being vacuum only (for $\alpha = 0$). Solving for the state $|\alpha, \xi, z\rangle$ alone is not enough to specify φ. It will be shown below in Eq. (123) how φ is specified.

and (122) in this relation, and using $\mu = |\mu|e^{i\psi}$ (see Eq.(105)), we obtain

$$e^{i\varphi} = -e^{-2i(k_p z - \psi)}, \tag{123}$$

$$\psi = \arctan\left[\frac{k_p(k_\perp^2 - \kappa_\perp^2)}{g(k_p^2 - \sigma^2 D_u^2)} \tanh\left(\frac{gz}{2}\right)\right]. \tag{124}$$

In the limit where instability is maximized, at transverse momentum $k_\perp = \kappa_\perp$, then $\psi = 0$ and $\xi = e^{-2ik_p z}\tanh(\bar{g}z/2)$, and we obtain the result, which has the familiar form of the TMSV, [28]

$$|\xi, z\rangle_{k_\perp=\kappa_\perp} = \mathrm{sech}(\bar{g}z/2)\sum_n (-1)^n e^{-2ink_p z}\tanh^n(\bar{g}z/2)|n, n\rangle. \tag{125}$$

The TMSV state will be explored later as a potential means to generate ultrashort photon pairs from vacuum using the more generalized form Eq. (122).
On the other hand, when $z = 0$, $\xi = 0$, $\tilde{\alpha} = \alpha$, only the $n = 0$ term survives, and Eq. (121) reduces to

$$|\alpha, \xi = 0, z = 0\rangle = e^{-\frac{|\alpha|^2}{2}}\sum_k \frac{\alpha^k}{\sqrt{k!}}|k, 0\rangle, \tag{126}$$

which, as mentioned below Eq. (113), is precisely a coherent state in the $(\Omega, \vec{k}_\perp)$ mode with average photon number $|\alpha|^2$, and vacuum in the $(-\Omega, -\vec{k}_\perp)$ mode. Eq. (126) is the initial quantum state that generalizes the classical solution described in Chapters 2−3. Eq. (121) thus couples the vacuum flucuations with the coherent seed (assuming $\alpha \neq 0$) and can be considered a two-mode squeezed coherent state, extended to include transverse dimensions and a broad spectral range.

6.3 Exploring the quantum state of Kerr instability for given two-mode state

Back to the general solution from Eq. (121), the average number of photons in the $(\Omega, \vec{k}_\perp)$ mode is found to be

$$\langle\hat{n}_\Omega\rangle = \langle\alpha, \xi, z|\hat{a}_\Omega^\dagger(0)\hat{a}_\Omega(0)|\alpha, \xi, z\rangle = |\nu|^2 + |\mu|^2|\alpha|^2. \tag{127}$$

In the limit where the instability is maximized, when $k_\perp = \kappa_\perp$, we have

$$\langle\hat{n}_\Omega\rangle_{k_\perp=\kappa_\perp} = \sinh^2\left(\frac{\bar{g}z}{2}\right) + |\alpha|^2\cosh^2\left(\frac{\bar{g}z}{2}\right), \tag{128}$$

which shows the coupling between vacuum flucuations and the coherent seed; the first term arises from vacuum, and the second is an amplification of the average photon number from the coherent seed. As for the $(-\Omega, -\vec{k}_\perp)$ mode, we have

$$\langle \hat{n}_{-\Omega} \rangle = \langle \alpha, \xi, z | \hat{a}^\dagger_{-\Omega}(0) \hat{a}_{-\Omega}(0) | \alpha, \xi, z \rangle = |\nu|^2 + |\nu|^2 |\alpha|^2. \tag{129}$$

In the limit where the instability is maximized, the result is

$$\langle \hat{n}_{-\Omega} \rangle_{k_\perp = \kappa_\perp} = \sinh^2 \left(\frac{\bar{g} z}{2} \right) + |\alpha|^2 \sinh^2 \left(\frac{\bar{g} z}{2} \right), \tag{130}$$

which is similar to Eq. (128), especially in the limit of large $\bar{g}z/2$. However, it's clear that they differ for small $\bar{g}z/2$, as they should, since, initially, there is vacuum in the $(-\Omega, -\vec{k}_\perp)$ mode, and a coherent state in the $(\Omega, \vec{k}_\perp)$ mode.

Since the general state of Eq. (121) is a two-mode squeezed state with a coherent state in mode $(\Omega, \vec{k}_\perp)$ and vacuum in mode $(-\Omega, -\vec{k}_\perp)$, it exhibits photon statistics like that of a two-mode squeezed coherent state, with the coherent state amplitude in mode $(-\Omega, -\vec{k}_\perp)$ set to 0. For example, see Ref. [59], with one of their coherent state amplitudes set to zero; $\beta = 0$. As mentioned in that work, the criteria for whether the two-mode photon statistics are classical or nonclassical can be found from the quantity

$$D_2 = \langle \hat{n}^{(2)}_\Omega \rangle + \langle \hat{n}^{(2)}_{-\Omega} \rangle - 2 \langle \hat{n}_\Omega \hat{n}_{-\Omega} \rangle, \tag{131}$$

where superscript (2) indicates squared and normally-ordered. That is, $\hat{n}^{(2)} = \hat{a}^{\dagger 2} \hat{a}^2$ for each mode. If $D_2 < 0$, the photon statistics are nonclassical (sub-Poissonian). If $D_2 = 0$, the statistics correspond to a coherent state (Poissonian). Finally, if $D_2 > 0$, the photon statistics correspond to chaotic, or thermal light (super-Poissonian), which can be described classically as well. For example, using Eq. (121), the normally-ordered expectation value of photon number squared in the $(\Omega, \vec{k}_\perp)$ mode, which will also be used below, is

$$\langle n^{(2)}_\Omega \rangle = |\alpha|^4 + 4|\mu|^2 |\nu|^2 |\alpha|^2 + 2|\nu|^2, \tag{132}$$

and Eq. (131) is found to be

$$D_2 = |\alpha|^4 - 2|\nu|^2 |\alpha|^2 - 2|\nu|^2. \tag{133}$$

First of all, notice in the TMSV limit, where $|\alpha| = 0$, then $D_2 \leq 0$ as $|\nu|^2 \geq 0$, implying that the TMSV is a case of nonclassical light in the non-trivial case of $z \neq 0$. However, it will be shown below that only making a measurement on one of the modes, and ignoring the other corresponds to thermal light for the measured mode, which is classical and super-Poissonian light. Therefore, it is the intermode coupling alone that contributes to the light becoming nonclassical, which is consistent with the remarks in Ref. [59]. In general, with Eq. (133)

we obtain the condition

$$|\alpha|^2 - |\nu|\left(|\nu| + \sqrt{|\nu|^2+2}\right) \begin{cases} < 0 & \text{for sub-Poissonian statistics} \\ = 0 & \text{for Poissonian statistics} \\ > 0 & \text{for super-Poissonian statistics} \end{cases}$$

In the limit of maximum KIA, we obtain

$$|\alpha|^2 - \sinh^2\left(\frac{\bar{g}z}{2}\right) - \sinh\left(\frac{\bar{g}z}{2}\right)\sqrt{2+\sinh^2\left(\frac{\bar{g}z}{2}\right)} \begin{cases} < 0 & \text{for sub-Poissonian statistics} \\ = 0 & \text{for Poissonian statistics} \\ > 0 & \text{for super-Poissonian statistics} \end{cases}$$

Therefore, by choosing $|\alpha|^2$ and $\bar{g}z/2$ appropriately in a given experiment, the regime of photon statistics can be controlled. As an aside, notice that $\sinh^2(\bar{g}z/2)$ is the average photon number obtained in the TMSV state in either mode as shown above, as shown in Eqs. (128) and (130).

The expectation values $\langle \hat{a}_\Omega(z)\rangle$ and $\langle \hat{a}^\dagger_\Omega(z)\rangle$ are found to be

$$\langle \hat{a}_\Omega(z)\rangle = \langle \alpha,\xi,z|\hat{a}_\Omega(0)|\alpha,\xi,z\rangle = |\mu|^2\tilde{\alpha} \tag{134a}$$

$$\langle \hat{a}^\dagger_\Omega(z)\rangle = \langle \alpha,\xi,z|\hat{a}^\dagger_\Omega(0)|\alpha,\xi,z\rangle = |\mu|^2\tilde{\alpha}^*. \tag{134b}$$

In the limit of maximum instability amplification, Eqs. (134) become

$$\langle \hat{a}_\Omega(z)\rangle = |\alpha|\cosh\left(\frac{\bar{g}z}{2}\right)\exp\left[i(k_p z + \sigma D_u z + \theta)\right] \tag{135a}$$

$$\langle \hat{a}^\dagger_\Omega(z)\rangle = |\alpha|\cosh\left(\frac{\bar{g}z}{2}\right)\exp\left[-i(k_p z + \sigma D_u z + \theta)\right], \tag{135b}$$

where $\alpha = |\alpha|e^{i\theta}$. Eqs. (135) represent an amplified coherent state. Summing over all modes, the average of the electric field of the perturbation, $\langle\hat{\varepsilon}(z)\rangle$, can be obtained from Eq.(99), by using Eqs. (134). In particular, $\hat{\varepsilon}(z)$ from Eq.(99) becomes

$$\hat{\varepsilon}(\mathbf{x},t) = \left(\frac{\hbar}{2\epsilon_0 c}\right)^{1/2}\frac{\sqrt{T}L}{(2\pi)^3}\int d\omega dk_x dk_y \sqrt{\frac{\omega_p+\Omega}{n(\omega_p+\Omega)}}\left[\hat{a}_\Omega(z)e^{i(\omega_p+\Omega)t}e^{i\vec{k}_\perp\cdot\vec{r}_\perp} + \text{H.c.}\right], \tag{136}$$

where we have taken the limit of large T and A,

$$\frac{1}{\sqrt{T}}\sum_{\Omega} \to \frac{\sqrt{T}}{2\pi}\int d\Omega \tag{137a}$$

$$\frac{1}{\sqrt{A}}\sum_{\vec{k}_\perp} \to \frac{L}{4\pi^2}\int d\vec{k}_\perp. \tag{137b}$$

Eq. (136) represents a continuous inverse Fourier transform over the coordinates $(\Omega, \vec{k}_\perp) \to (\vec{r}_\perp, t)$. Formally, using Eqs. (134), we may then write $\langle\hat{\varepsilon}(z)\rangle$ as

$$\langle\hat{\varepsilon}(\mathbf{x},t)\rangle = \left(\frac{\hbar}{2\epsilon_0 c}\right)^{1/2}\frac{\sqrt{T}L}{(2\pi)^3}\int d\Omega d\vec{k}_\perp \sqrt{\frac{\omega_p+\Omega}{n(\omega_p+\Omega)}}\left[|\mu_\Omega|^2\tilde{\alpha}_\Omega e^{i(\omega_p+\Omega)t}e^{i\vec{k}_\perp\cdot\vec{r}_\perp} + \text{H.c.}\right]. \tag{138}$$

Integration of Eq. (138) over transverse coordinates may be approximated in principle by the same method as in Chapter 4. That is, expanding $k_\perp$ as $k_\perp = \kappa_\perp + \Delta k_\perp$, where we assume strong amplification such that $\Delta k_\perp \ll \kappa_\perp$. We assume that we are in the classical regime, because in the strong amplification limit, there are many photons involved in amplification of the seed, up to even about 10% of the pump intensity as discussed in Chapter 4. Therefore, there is no appreciable benefit to repeating such cumbersome calculations that have already been performed in Chapter 4.

We proceed by examining the photon statistics further. The joint probability of finding N photons in mode $(\Omega, \vec{k}_\perp)$ and M photons in mode $(-\Omega, -\vec{k}_\perp)$ is found to be

$$P_{NM} = |\langle N, M|\alpha,\xi,z\rangle|^2 = \frac{e^{-|\alpha|^2}}{|\mu|^2}\frac{|\tilde{\alpha}|^{2(N-M)}}{(N-M)!}\binom{N}{M}|\xi|^{2M}. \tag{139}$$

For $k_\perp = \kappa_\perp$, Eq. (139) reduces to

$$P_{NM} = \frac{e^{-|\alpha|^2}|\alpha|^{2(N-M)}}{(N-M)!}(1-p)\binom{N}{M}p^M(1-p)^{N-M} \tag{140a}$$

$$p = \tanh^2(\bar{g}z/2), \tag{140b}$$

which is a coupling between a Poisson process of observing $N-M$ photons with average photon number $|\alpha|^2$, and a binomial process whereby there are M photons observed, given N trials with probability p. We plot various cases of Eq (140a) in Fig. 21 using 3-D bar graphs. In the top-left panel, for $\bar{g}z/2 = 1.5$, $p \approx 0.82$, and $\alpha = 0$, only terms $M = N$ survive, and we obtain

$$P_{NM} \to (1-p)p^M\delta_{N,M}, \tag{141}$$

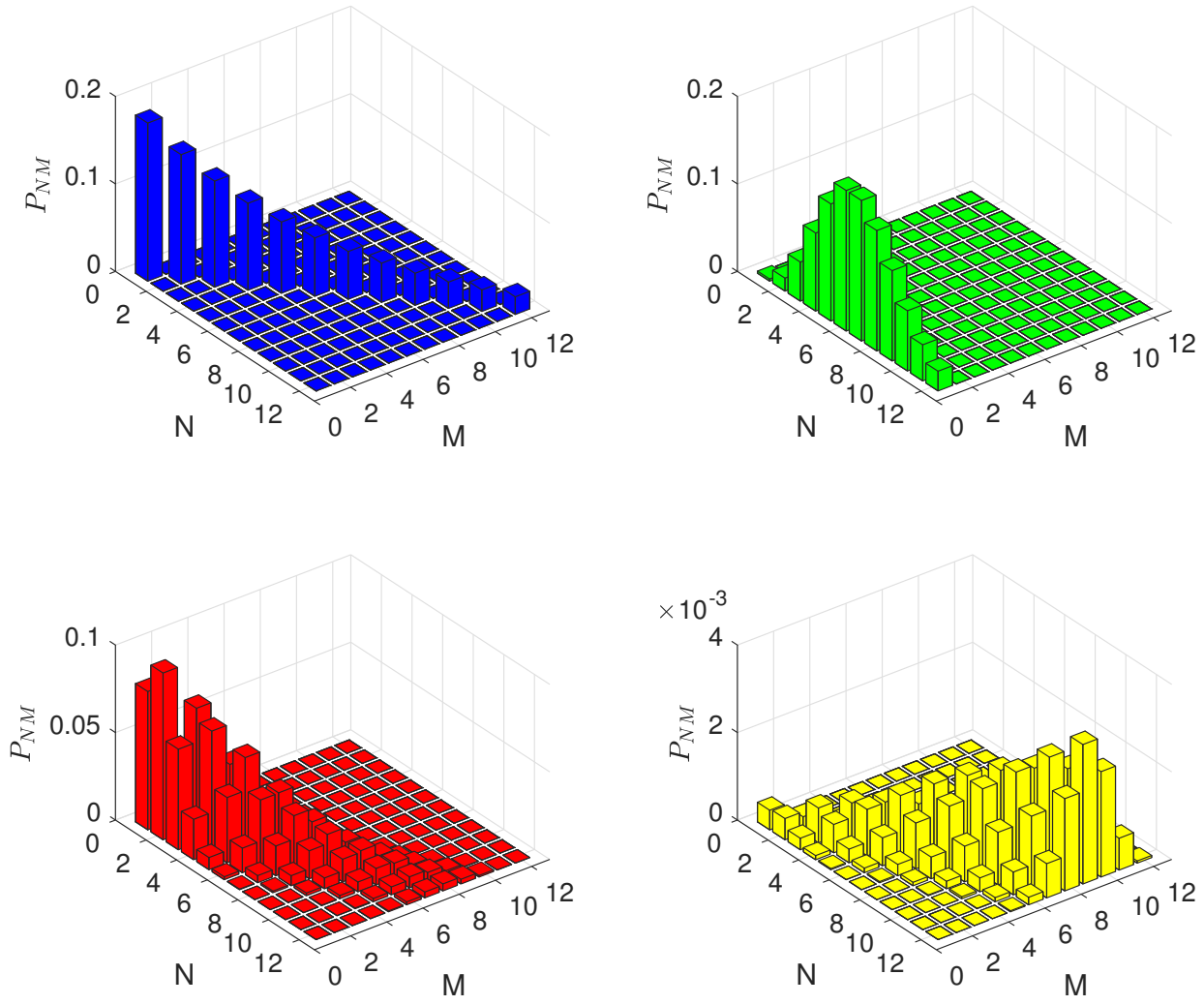

Figure 21: Bar graphs showing the joint probability of detecting N photons in the $(\Omega, \vec{k}_\perp)$ mode, and M photons in the $(-\Omega, -\vec{k}_\perp)$ mode from Eq. (140a). Top left: $\bar{g}z/2 = 1.5$, $p \approx 0.82$, and $\alpha = 0$. Top right: $z = 0$, $p = 0$ and $|\alpha|^2 = 6$. Bottom left: $\bar{g}z/2 = 0.75$, $p \approx 0.40$, and $|\alpha|^2 = 2.02$. Bottom right: $\bar{g}z/2 = 1.5$, $p \approx 0.82$, and $|\alpha|^2 = 6$.

which is precisely the joint probability in the TMSV state. In the limit of very small p, the binomial distribution in Eq. (139) can be replaced by a Poisson distribution, resulting in the approximation

$$P_{NM} \to \frac{e^{-|\alpha|^2}|\alpha|^{2N}}{N!}\frac{e^{-Np}(Np)^M}{M!}, \tag{142}$$

which is a product of two Poisson distributions, one for mode $(\Omega, \vec{k}_\perp)$ with N photons being observed at an average rate of $|\alpha|^2$, and one for mode $(-\Omega, -\vec{k}_\perp)$, with M photons being observed at an average rate of Np. According to the two-mode statistics criterion of Eq.(133), here $D_2 \approx -10$, corresponding to sub-Poissonian statistics. In the top right panel, we use $|\alpha|^2 = 6$, and $p = 0$, $(z = 0)$, for which only the term $M = 0$ survives, yielding

$$P_{NM} \to \frac{e^{-|\alpha|^2}|\alpha|^{2N}}{N!}\delta_{M,0}, \tag{143}$$

which is consistent with there being a coherent state in mode $(\Omega, \vec{k}_\perp)$ and vacuum in the $(-\Omega, -\vec{k}_\perp)$ mode. Further, here $D_2 = 6$, corresponding to super-Poissonian statistics, which differs from simply Poissonian statistics for a single-mode coherent state. In the bottom-left panel, we plot Eq. (140a) for $\bar{g}z/2 = 0.75$, $p \approx 0.40$, and $|\alpha|^2 \approx 2.02$, showing onset of the coupling between vacuum and coherent states. Here, we have set $|\alpha|^2 = \sinh^2\left(\frac{\bar{g}z}{2}\right) - \sinh\left(\frac{\bar{g}z}{2}\right)\sqrt{2 + \sinh^2\left(\frac{\bar{g}z}{2}\right)}$ so that $D_2 = 0$ precisely and we obtain Poissonian statistics for the two-mode radiation. In the bottom-right panel, we plot Eq. (140a) for $\bar{g}z/2 = 1.5$, $p \approx 0.82$, and $|\alpha|^2 = 6$, again showing the coupling between vacuum and coherent states, with the Poisson statistics beginning to emerge as the coherent state amplitude becomes larger. However, since $D_2 \approx -4$, we still have sub-Poissonian statistics as $|\alpha|^2$ is not large enough to dominate the statistics of the two-mode radiation. Still, the joint probability distribution is pushed out to larger values due to increased $|\alpha|^2$, with the probability of detecting small numbers of photons vastly decreasing.

The density operator for the general state $|\alpha, \xi, z\rangle$ is given by $\hat{\rho}(z) = |\alpha, \xi, z\rangle\langle\alpha, \xi, z|$. The reduced density operators for each mode are found by tracing over the other mode. That is, $\hat{\rho}_\Omega(z) = \mathrm{Tr}_{-\Omega}\hat{\rho}(z)$ and $\hat{\rho}_{-\Omega}(z) = \mathrm{Tr}_\Omega\hat{\rho}(z)$. Using these reduces density operators, the probability of finding M photons may be found for each mode separately, without making any measurement on the other mode. The results are

$$P^{(+)} = \langle M|\hat{\rho}_\Omega|M\rangle = \frac{e^{-|\alpha|^2}}{|\mu|^2}|\xi|^{2M}\frac{(-1)^M}{M!}\mathscr{U}\left(-M, 1, -\frac{|\alpha|^2}{|\nu|^2}\right) \tag{144a}$$

$$P^{(-)} = \langle M|\hat{\rho}_{-\Omega}|M\rangle = \frac{e^{-|\alpha|^2}}{|\mu|^2}|\xi|^{2M}\mathscr{M}\left(M + 1, 1, \frac{|\alpha|^2}{|\mu|^2}\right), \tag{144b}$$

where $\mathscr{M}$ and $\mathscr{U}$ are the confluent (Kummer's) hypergeometric functions of the first and second kind, respectively. Note that these hypergeometric functions have the limiting values $(-1)^M\mathscr{U}(-M, 1, 0) = M!$ and $\mathscr{M}(M + 1, 1, 0) = 1$, thus reducing $P^{(\pm)}$ to the identical TMSV probabilites when $\alpha = 0$ as will be seen below. As well, when $z = 0$, $(-1)^M|\xi|^{2M}\mathscr{U}\left(-M, 1, -\frac{|\alpha|^2}{|\nu|^2}\right)_{z=0} \to |\alpha|^{2M}$, and $\mathscr{M}\left(M + 1, 1, \frac{|\alpha|^2}{|\mu|^2}\right)_{z=0} \to e^{|\alpha|^2}\delta_{M,0}$, so the probabilities $P^{(+)}$ and $P^{(-)}$ reduce to Poisson statistics (coherent state) and vacuum $(\delta_{M,0})$,

respectively, as they should. In the limit of maximized instability, Eqs. (144) reduce to

$$P^{(+)} \to e^{-|\alpha|^2} \frac{\tanh^{2M}\left(\frac{\bar{g}z}{2}\right)}{\cosh^2\left(\frac{\bar{g}z}{2}\right)} \frac{(-1)^M}{M!} \mathscr{U}\left(-M, 1, -\frac{|\alpha|^2}{\sinh^2\left(\frac{\bar{g}z}{2}\right)}\right) \tag{145a}$$

$$P^{(-)} \to e^{-|\alpha|^2} \frac{\tanh^{2M}\left(\frac{\bar{g}z}{2}\right)}{\cosh^2\left(\frac{\bar{g}z}{2}\right)} \mathscr{M}\left(M+1, 1, \frac{|\alpha|^2}{\cosh^2\left(\frac{\bar{g}z}{2}\right)}\right). \tag{145b}$$

In Figure (22), various bar graphs are plotted for both $P^{(+)}$ and $P^{(-)}$.

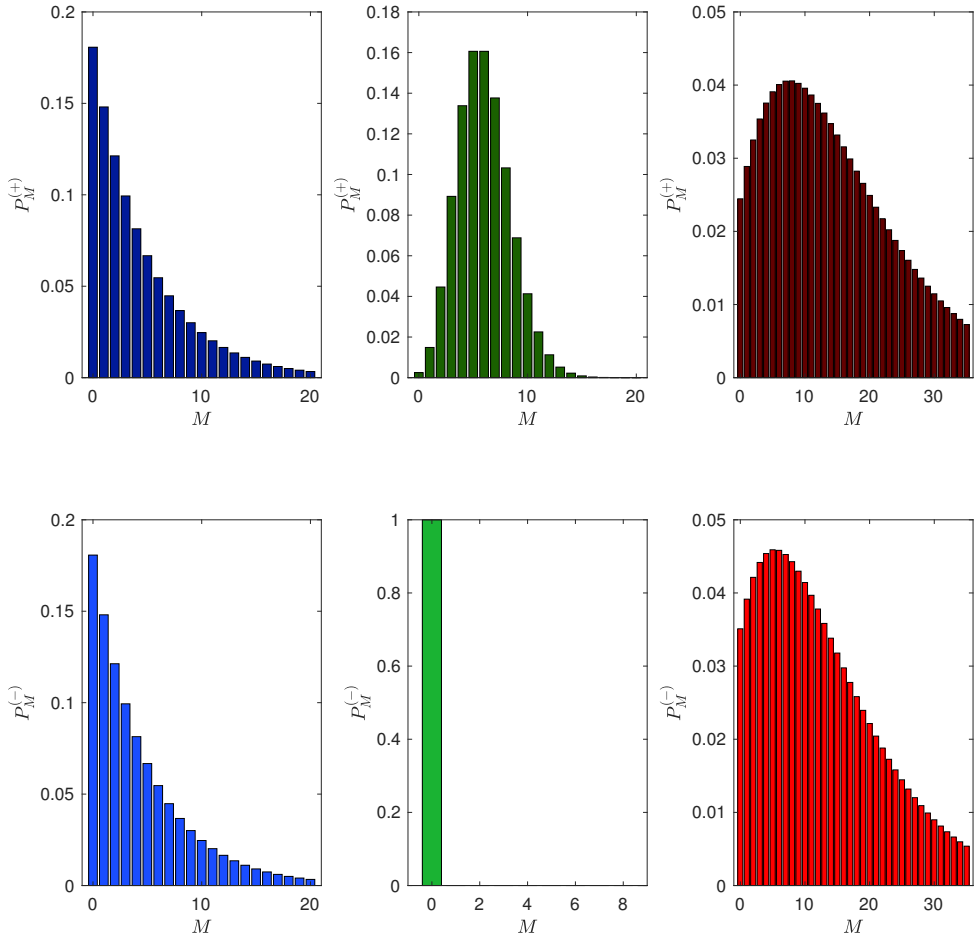

Figure 22: Bar graphs for the reduced proabilities for both $(\Omega, \vec{k}_\perp)$ (top row) and $(-\Omega, -\vec{k}_\perp)$ (bottom row) modes, using Eqs. (145). First column: $\alpha = 0$ and $\bar{g}z/2 = 1.5$. Second column: $z = 0$ and $|\alpha| = \sqrt{6}$. Third column: $|\alpha| = \sqrt{2}$ and $\bar{g}z/2 = 1.5$.

The top row (darker colours) of subplots correspond to $P^{(+)}$. The bottom row (lighter

colours) correspond to $P^{(-)}$. The first column corresponds to the TMSV limit where $\alpha = 0$ and $\bar{g}z/2 = 1.5$. Clearly, the left plots are identical, as they should be for the TMSV. These statistics are written as

$$P^{(+)}_{\alpha=0} = \frac{\tanh^{2M}\left(\frac{\bar{g}z}{2}\right)}{\cosh^{2}\left(\frac{\bar{g}z}{2}\right)} = P^{(-)}_{\alpha=0}. \tag{146}$$

Below, it will be shown that in this limit, Eqs. (146) correspond to statistics for thermal light. In the second column of Figure (22), $z = 0$ and $|\alpha| = \sqrt{6}$, where initially there is a coherent state in the $(\Omega, \vec{k}_\perp)$ mode, and vacuum in the $(-\Omega, -\vec{k}_\perp)$ mode. In this case, the probabilities reduce to

$$P^{(+)}_{z=0} \to e^{-|\alpha|^2}\frac{|\alpha|^{2M}}{M!} \tag{147a}$$

$$P^{(-)}_{z=0} \to \delta_{M,0}, \tag{147b}$$

corresponding to Poisson statistics (coherent state) for $P^{(+)}_{z=0}$, and simply vacuum for $P^{(-)}_{z=0}$. The far right column of Figure (22) corresponds to $|\alpha| = \sqrt{2}$ and $\bar{g}z/2 = 1.5$. Since the coherent state was initially in the $(\Omega, \vec{k}_\perp)$ mode, the statistics for detecting photons from $P^{(+)}$ are more spread out across larger values for M, whereas since initially there was vacuum in the $(-\Omega, -\vec{k}_\perp)$ mode, the more likely photon numbers for $P^{(-)}$ are condensed towards smaller values of M. As $|\alpha|$ increases, these differences become more exaggerated. Conversely, for a fixed $|\alpha|$, as z increases, the probabilities $P^{(+)}$ and $P^{(-)}$ become less distinguishable as the instability ensues.

6.4 Exploring the two-mode squeezed vacuum state

Now we focus our attention on the case where $\alpha = 0$, which is the general TMSV state, given by Eq. (122). This state arises from perturbations acting on the pump from vacuum flucuations which are amplified by the Kerr instability.

6.4.1 Thermal statistics and conical emission

As mentioned above, the reduced density operators are identical and the probability of detecting M photons in either mode, with no measurement made on the other mode, corresponds to thermal light. For $\alpha = 0$, we have

$$P^{(\pm)}_{\alpha=0} = (1 - |\xi|^2)|\xi|^{2M}. \tag{148}$$

From Eqs. (127) and (129), for $\alpha = 0$, we have $\langle \hat{n}_\Omega \rangle = \langle \hat{n}_{-\Omega} \rangle \equiv \langle \hat{n} \rangle = |\xi|^2/(1-|\xi|^2)$. Therefore, Eq. (148) may be re-written as

$$P^{(\pm)}_{\alpha=0} = \frac{\langle \hat{n} \rangle^M}{(\langle \hat{n} \rangle + 1)^{M+1}}, \tag{149}$$

which is a thermal (Bose-Einstein) distribution with average photon number $\langle \hat{n} \rangle$ in either mode. Therefore, thermal light is an example of super-Poissonian light, and can be described classically. Using Eq. (105) and (106), $\langle \hat{n} \rangle$ may be written explicitly as

$$\langle \hat{n} \rangle = \frac{\bar{g}^2}{g^2} \sinh^2 \left(\frac{gz}{2} \right). \tag{150}$$

For maximum instability, when $k_\perp = \kappa_\perp$, we have $\langle \hat{n} \rangle = \sinh^2(\bar{g}z/2)$, consistent with Eqs. (128) and (130) for $\alpha = 0$. Light emitted transversally from the pump at $\kappa_\perp$ corresponds to the vacuum noise being exponentially amplified along the half-angle $\tan\bar{\theta} = \pm\kappa_\perp/k_p$ (for light of frequency $\omega_p + \Omega$), which describes the onset of conical emission. It is said to be conical because of the transverse symmetry. The emission angle is dependent on the frequency of the light. In short, the onset of conical emission arises from vacuum fluctuations being amplified by Kerr instability, and the conically-emitted light behaves like a thermal light source. Associated with thermal light is an effective temperature, T_{eff}, of the light source, and it is connected to mean photon number of frequency $\omega_p + \Omega$ by Planck's law as [28]

$$\langle \hat{n} \rangle = \frac{\exp\left(-\frac{\hbar(\omega_p+\Omega)}{k_B T_{eff}} \right)}{1 - \exp\left(-\frac{\hbar(\omega_p+\Omega)}{k_B T_{eff}} \right)}. \tag{151}$$

Using $\langle \hat{n} \rangle = \sinh^2(\bar{g}z/2)$, this may be rearranged for T_{eff} as

$$T_{eff} = \frac{\hbar(\omega_p + \Omega)}{2k_B \ln\left[\coth\left(\frac{\bar{g}z}{2}\right)\right]}. \tag{152}$$

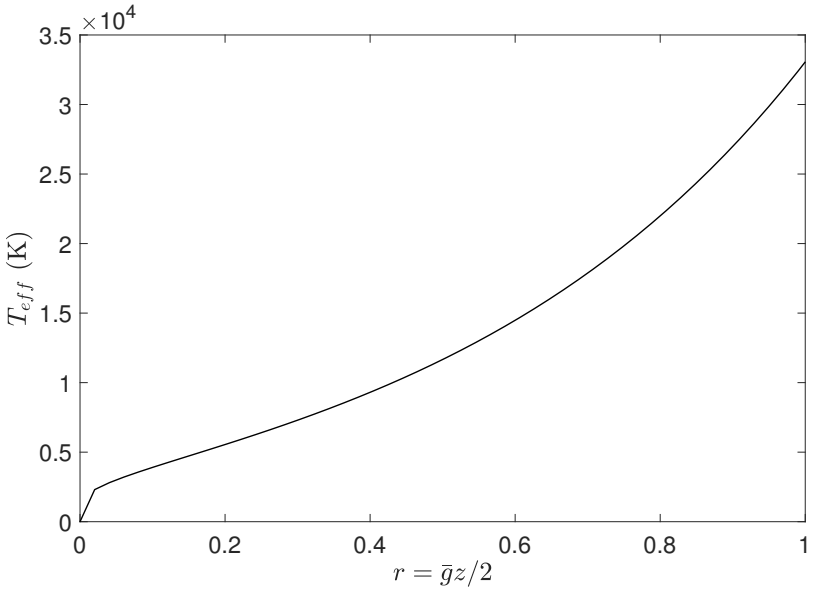

Figure 23: Calculating effective temperature T_{eff} from Eq. (152) as a function of $r = \bar{g}z/2$ for $\hbar(\omega_p + \Omega) = 1.54$ eV.

To illustrate some typical numbers for T_{eff} for realistic experimental parameters, we choose $\hbar(\omega_p + \Omega) = 1.54$ eV, corresponding to a wavelength of 800 nm, and plot T_{eff} as a function of $r = \bar{g}z/2$. As seen in Fig. (23), there is a regime from $r = 0$ to $r \approx 0.02$ where T_{eff} increases linearly with r. In that regime, T_{eff} increases rapidly from 0 K to about 2000 K, which is a typical temperature of standard incandescent lamps, and is considered "warm" light. Beyond this regime, T_{eff} quickly increases to over 10^4 K, which corresponds to, say, the surface temperature of a blue star.

6.4.2 Two-mode photon statistics

Returning to the two-mode case, and by means of Eqs. (105) and (106), and considering the set of values $k_\perp = \kappa_\perp$ for maximum instability, we obtain

$$|\xi|^2 = \tanh^2\left(\frac{\bar{g}z}{2}\right), \tag{153}$$

Using Eq. (153) in the joint probability two-mode version of Eq. (148) gives

$$P_{N,M} = \operatorname{sech}^2\left(\frac{\bar{g}z}{2}\right)\tanh^{2M}\left(\frac{\bar{g}z}{2}\right)\delta_{N,M}, \tag{154}$$

which corresponds to generation of photon pairs along the diagonal $N = M$ (see Fig. (21), top left panel). Optimizing Eq. (154) with respect to z, we find the optimal propagation

length to detect M photons in both modes to be

$$\bar{z} = \frac{2}{\bar{g}} \tanh^{-1}\left(\sqrt{\frac{M}{M+1}}\right). \tag{155}$$

Inserting Eq. (155) into Eq. (154) yields the maximum probability of detecting M photons

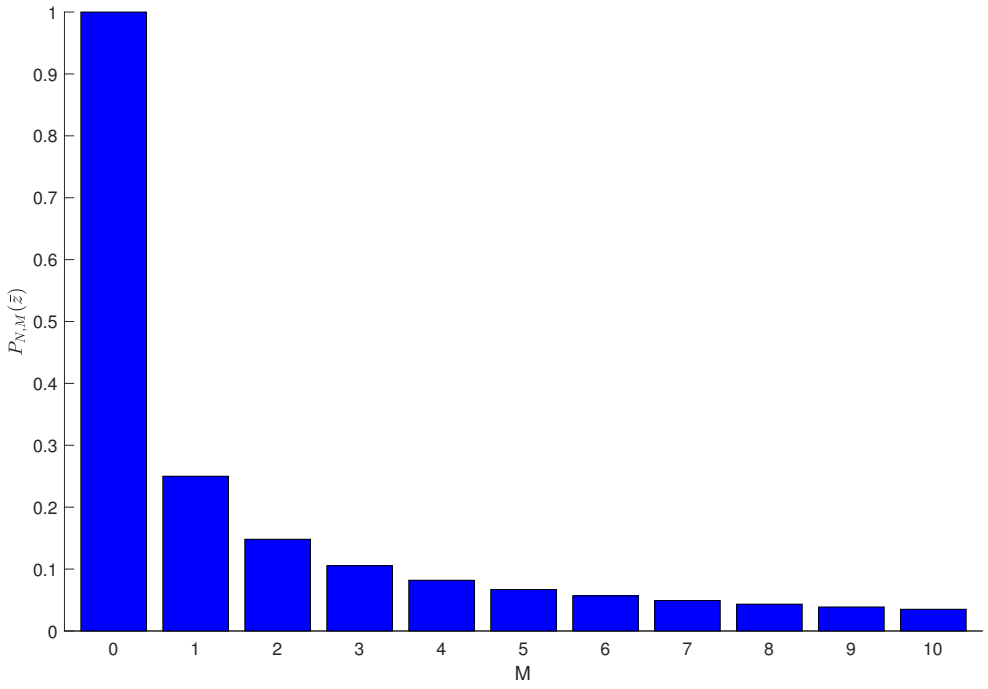

Figure 24: Bar graph showing the maximized probability of detecting M photon pairs, (only considering the plane $N = M$), see Eq. (156).

in either mode, (see Fig. (24)),

$$P_{N,M}(\bar{z}) = \frac{M^M}{(M+1)^{M+1}} \delta_{N,M}. \tag{156}$$

Trivially, if $z = \bar{z}(M = 0) = 0$, then there is no propagation, and hence no photons generated, which is why the maximum probability for $M = 0$ is listed as $P_{0,0} = 1$. As the photon number increases, the optimal probability decreases. For example, there is at best a probability of $P_{1,1} = 0.25$ to generate a single pair of photons.
In practice, if it is desired to generate a pair of a specific number of photons, $M = L$. We find $\bar{z}(M = L) = (2/\bar{g}) \tanh^{-1}\left(\sqrt{L/(L+1)}\right)$. If we insert $\bar{z}(M = L)$ into $P_{N,M}$, the probability of detecting $M = L$ will be optimized, but there will also be non-zero probabilities

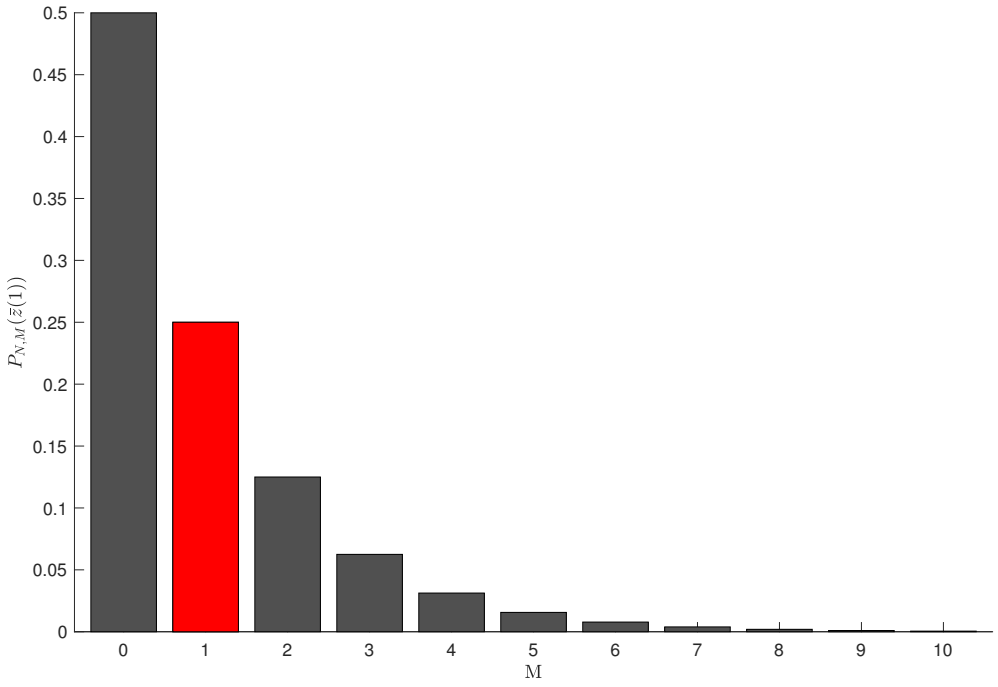

Figure 25: Bar graph showing the probability of detecting M photon pairs, given that the optimal propagation length, $\bar{z}(M=1)$, for generating a single photon pair was chosen (only considering the plane $N=M$), see Eq. (157).

of detecting other numbers of photons. That is,

$$P_{N,M}(\bar{z}(L)) = \frac{L^M}{(L+1)^{M+1}}\delta_{N,M}. \tag{157}$$

In Fig. (25), we show the example of $L=1$ corresponding to a single photon pair. Clearly, the probability of detecting the single pair is as high as possible at a probability of 0.25 (see also Fig. (24)), but there must be nonzero probabilities of generating pairs of other numbers of photons. Of course, it is most likely that no photons will be generated at all, with a probability of 0.5.

If it is desired to generate a single photon pair and avoid generating pairs of larger numbers of photons as much as possible, it is found that it is not optimal to use $z=\bar{z}$. For example, it's clear from Fig. (25) that there is still a probability of 0.125 that a double pair of photons will be generated even if there is a probability of 0.25 to generate a single photon pair. Therefore, we plot Eq. (154) with respect to the parameter $r=\bar{g}z/2$ (typically called the squeezing parameter) in order to quantify how to minimize the probabilities of generating other pairs of photons, as much as possible. Since we use the parameter r, the discussion is general and applies to any material of interest. In Fig. (26) we assume that a single photon pair being generated is desired and all other pairs are to be avoided as much as possible. As

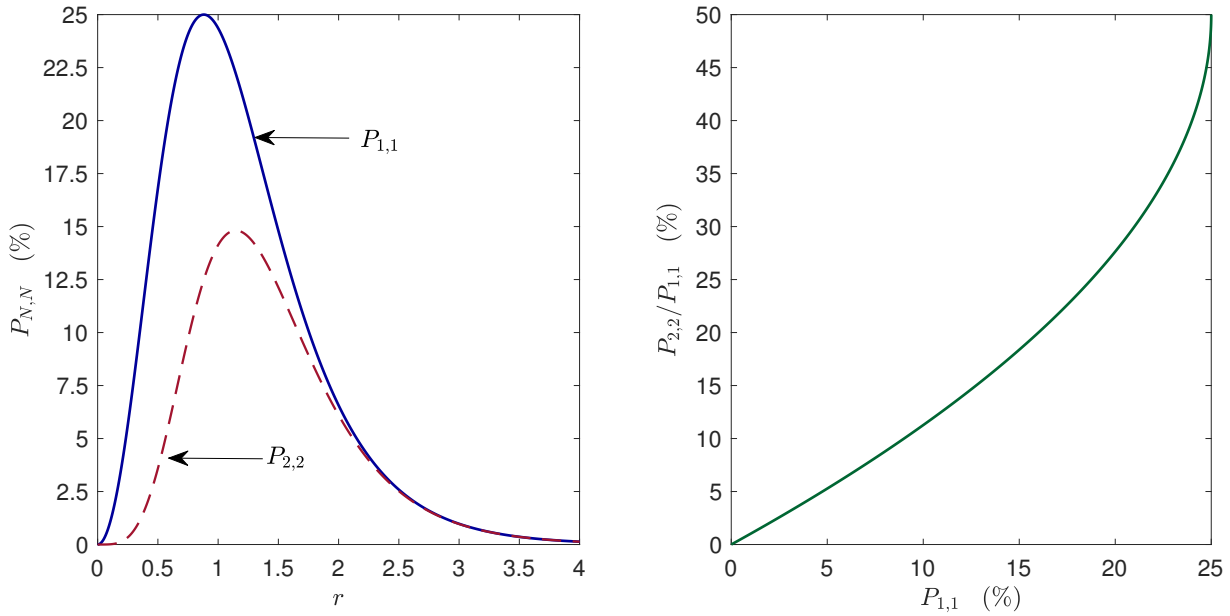

Figure 26: In the left panel, we plot $P_{1,1}$ and $P_{2,2}$ from Eq. (154) as a function of parameter r. In the right panel, we show a phase space plot for $P_{1,1}$ and $P_{2,2}$ (normalized to $P_{1,1}$). The right panel is truncated at the point of max $P_{1,1}$ (25%) as there is no benefit of considering probabilities beyond this point.

$P_{N,N}$ is a monotonically decreasing function with N, it is suffifient to only consider the next highest pair, $N = 2$. That is, if $P_{2,2}$ is reduced, then pairs of larger numbers of photons will be reduced even more. In the left panel, we see that it is ideal to choose r corresponding to $P_{1,1}$ that is not the maximum value of 25%, if it is desired to reduce the probabilities of generating other numbers of photon pairs. We quantify this in the right panel by showing the phase space of $P_{1,1}$ and $P_{2,2}$ (normalized to $P_{1,1}$). Choosing a smaller value of $P_{1,1}$ suppresses $P_{2,2}$. For example, choosing $P_{1,1} = 5\%$ corresponds to $P_{2,2} \approx 0.25\%$. Therefore, it is approximately 20 times more likely that a single photon pair is generated over a double photon pair, given that $P_{1,1} = 5\%$. According to the left panel, this corresponds to $r = \bar{g}z/2 = 0.25$. Again, this is in general true for any material.

6.5 Generating ultrafast photon pairs from vacuum–connecting theory to experiment

To better understand the detection of the TMSV photon states, we will first calculate the average intensity registered at a detector, which involves summing over all relevant $(\Omega, \vec{k}_\perp)$ modes. To do this, we calculate the Poynting vector operator. In the scalar limit, we implicitly assume the electric field of the perturbation will be polarized orthogonal to the magnetic field of the perturbation, resulting in the Poynting operator being polarized orthogonal to

these two fields, which is parallel to the propagation direction. The vacuum state expectation value of the Poynting vector,

$$\hat{S}(\mathbf{x},t) = \frac{1}{\mu_0}\left[\hat{\varepsilon}^{(-)}\hat{\beta}^{(+)} + \text{H.c}\right], \tag{158}$$

will give the the average intensity registered at the detector; we assume negligible loss at the exit of the material and during propagation to the detector. To be clear, by intensity we mean the usual optical intensity given in units of [photon energy / (time × area)]. Here, $\hat{\varepsilon}^{(-)}$ is given by Eq. (99), and $\hat{\beta}^{(+)}$ is typically called the positive-frequency component of the magnetic field of the perturbation, given by [56]

$$\hat{\beta}^{(+)} = \frac{1}{\sqrt{AT}}\sum_{\Omega,\vec{k}_\perp}\left[\frac{\hbar(\omega_p+\Omega)n(\omega_p+\Omega)}{2\epsilon_0 c^2}\right]^{1/2}\hat{a}_\Omega(z)e^{i(\omega_p+\Omega)t+i\vec{k}_\perp\cdot\vec{r}_\perp}. \tag{159}$$

Analogously to the electric field, $\hat{\beta}^{(-)} = \hat{\beta}^{(+)\dagger}$. The expectation value is taken over the vacuum state of Eq. (158); the solution for $\hat{a}_\Omega(z)$ from Eq. (104) is used, as well as the ESCR of Eq. (100) to obtain

$$\langle 0|\hat{S}|0\rangle = \langle I\rangle = \frac{\hbar}{4\pi^2}\int(\omega_p+\Omega)d\Omega k_\perp dk_\perp \frac{\bar{g}^2}{g^2}\sinh^2\left(\frac{gz}{2}\right). \tag{160}$$

By energy conservation, each pair of photons generated have frequencies that add up to $2\omega_p$. Therefore, the average photon pair flux can be calculated from the average intensity calculated in Eq. (160). Therefore, the average photon flux, in units of [photon pairs / (time × area)], is given by

$$\langle F\rangle = \frac{\langle I\rangle}{2\hbar\omega_p}. \tag{161}$$

In Eqs. (160) and (161), and similarly for all integrations, we have taken large T and A such that $\sum_\Omega/T \to \int d\Omega/(2\pi)$, and $\sum_{\vec{k}_\perp}/A \to \int d\vec{k}_\perp/(2\pi)^2 = \int k_\perp dk_\perp/(2\pi)$, converting to transverse polar coordinates in the last equality. As with the integrals that follow below, the integration is performed over the entire coordinate range for the instability. For transverse coordinates, this corresponds to the instability regime where $k_\perp$ spans $\left[\sqrt{\kappa_\perp^2-\delta_\perp^2}, \sqrt{\kappa_\perp^2+\delta_\perp^2}\right]$, for a given Ω, where $\delta_\perp^2$ is the instability regime half-width squared discussed below Eq. (104). In principle, the integration over Ω spans $[-\omega_p, \omega_p]$. In practice, the integration is done from $[\omega_{\min}-\omega_p, \omega_p]$; where $\omega_{\min}$ corresponds to the minimum frequency where the instability gain surpasses the material absorption (loss). In other words, $\lambda_{\max} = 2\pi c/\omega_{\min}$ is the longest wavelength in the transmission window of the bulk dielectric material considered. For example, for CaF_2, $\lambda_{\max} \approx 8$ μm, as discussed in Section 2.4.

Although Eq. (158) is in general a function of space and time, the expectation value for

the vacuum state, given by Eq. (160) is independent of time and transverse coordinates; and hence so is Eq. (161). In other words, photon pairs generated from vacuum arrive at a constant rate for a given propagation distance, z, on average. Further, Eq. (160) is only nonzero due to the inter-mode coupling found in the solution of $\hat{a}_\Omega(z)$, see Eq. (104). As we are dealing with the TMSV state, from Eq. (133), with $\alpha = \tilde{\alpha} = 0$, we have $D_2 = -2|\nu|^2$. Therefore, D_2 is negative, assuming the non-trivial case of $|\nu| \neq 0$, and the generation of photon pairs from vacuum using Kerr instability is a nonclassical process, as expected. Note that at sufficiently high pump intensities and/or propagation distance in material, the number of photons generated from vacuum will become very large. In this limit, the intensity of the generated photons will no longer be negligible compared to the pump, and our linearized perturbation theory might even become questionable. In this limit, we presume that the photons generated from vacuum would become like a seed, interacting back with the pump, which could be described classically. Higher order perturbation theory would be needed to treat this fully. It is not done here, for we have very small $\langle I \rangle$ compared to peak pump intensity, as will be seen below.

6.5.1 Correlation functions

The expectation values that we calculate, such as $\langle \hat{I} \rangle$ from Eq. (160) and $g^{(2)}$ (discussed below in Eq. (163)), are not sensitive to spectral phase as the expectation value is over the vacuum state. Therefore, any temporal properties we infer from the spectral content of the light correspond to transform-limited pulses. Any expectation values sensitive to the spectral phase resulting from the dispersive terms found in the phase term $K_u z$, (see Eq. (104)) require $\alpha \neq 0$. Therefore, for the TMSV state where $\alpha = 0$, no spectral phase information carries over into any expectation value from vacuum. To get a sense of the duration of such pulses, we can consider the duration over which photons arriving at the detector are bunched together. To do this, the second-order coherence function, $g^{(2)}(t_1, t_2)$ [28] is calculated. We assume the photons travel the same distance in space for detection (same $\mathbf{x}$), but can arrive at different times, t_1 and t_2. This coherence function is essentially a joint probability of detecting one photon distribution[3] at time t_1 and another at time t_2. In order to calculate $g^{(2)}$ we must calculate the second-order correlation function [28],

$$G^{(2)}(t_1, t_2) = \langle 0 | \hat{\varepsilon}^{(-)}(\mathbf{x}, t_1) \hat{\varepsilon}^{(-)}(\mathbf{x}, t_2) \hat{\varepsilon}^{(+)}(\mathbf{x}, t_2) \hat{\varepsilon}^{(+)}(\mathbf{x}, t_1) | 0 \rangle, \tag{162}$$

where $\hat{\varepsilon}^{(\pm)}$ are defined in Eq. (99). The coherence function is given by

$$g^{(2)}(t_1, t_2) = \frac{G^{(2)}(t_1, t_2)}{\left[G^{(1)}(t_1, t_1) G^{(1)}(t_2, t_2) \right]^{1/2}}, \tag{163}$$

[3]We say photon distribution because, as discussed below Eq.(167), there is always a chance that a pair of more than a single photon can be generated at a time.

where $G^{(1)}(t_i, t_i) = \langle 0|\hat{\varepsilon}^{(-)}(\mathbf{x}, t_i)\hat{\varepsilon}^{(+)}(\mathbf{x}, t_i)|0\rangle$ is the first-order correlation function for time t_i [28], which is simply proportional to the intensity at the detector at time t_i, see Eq. (160). Therefore, $G^{(1)}(t_1, t_1) = G^{(1)}(t_2, t_2) =$ constant. By means of Eq. (99) in Eq. (163) and the ESCR of Eqs. (100), we obtain

$$g^{(2)}(\tau) = 1 + \left|g^{(1)}(\tau)\right|^2 = 1 + \left|\frac{\int f(\Omega, k_\perp, z)e^{i\Omega\tau}k_\perp dk_\perp d\Omega}{\int f(\Omega, k_\perp, z)k_\perp dk_\perp d\Omega}\right|^2, \tag{164}$$

$$f(\Omega, k_\perp, z) = \frac{(\omega_p + \Omega)}{n(\omega_p + \Omega)}\frac{\bar{g}^2}{g^2}\sinh^2\left(\frac{gz}{2}\right). \tag{165}$$

The second-order coherence function is a function of the delay time only, $\tau = t_2 - t_1$. Note that for no delay, $g^{(2)}(0) = 2$, corresponding to two counts detected, which implies photon bunching−characteristic of chaotic light [28].

To quantify the distribution of photon statistics in the multimode case, the general probability distribution given by Eq. (148),

$$P_{\alpha=0}^{(\pm)} = P_{N,N}(\Omega, k_\perp, z) = (1 - |\xi|^2)|\xi|^{2N}, \tag{166}$$

can be explored further. In general, it is a function of frequency, transverse and longitudinal coordinates, and the number of photons generated in each mode, which occur in pairs. By summing over all tranverse wavevector modes, we obtain the probability distribution of the number of photons generated as a function of frequency for a given set of experimental parameters. In the limit of large A this results in an integration, as in the integrals above. The normalized probability distribution is given by

$$P'_{N,N}(\Omega, z) = \frac{\int k_\perp P_{N,N}(\Omega, k_\perp, z)dk_\perp}{\int k_\perp dk_\perp}. \tag{167}$$

Eq. (167) gives the probability distribution that a pair of N photons will be generated, as a function of frequency. It is best visualized as a 3-D colour plot for a given set of experimental parameters, and will be done below.

6.5.2 Numerical example of photon pair properties

Our main results of Eqs. (160), (161), (164), and (167) are dependent on given material and pump laser parameters, namely the linear and nonlinear refractive indices, the pump frequency and intensity, and the distance the pump propagates in the material. As a numerical example, CaF_2 is chosen to illustrate the different characteristics of our results derived above. As before, the optical properties of CaF_2 are found in Section 2.4.

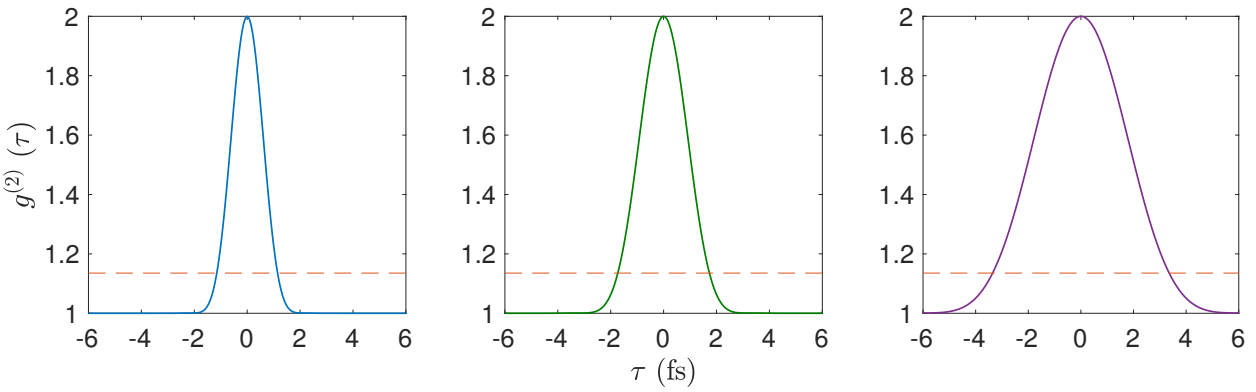

Figure 27: The second order coherence function, from Eq. (164), is plotted as a function of delay time, τ. In the left, middle and right panels, $\lambda_p = 0.532$ μm, $\lambda_p = 0.8$ μm, and $\lambda_p = 1.55$ μm are chosen, respectively. In each case, the material is CaF_2, with $I_p = 10$ GW/cm^2 and a propagation length of $L = 1$ mm. In each panel, the dashed line indicates the $1/e^2-$width, which indicates τ_c, the coherence time.

First, $g^{(2)}(\tau)$ is plotted, then we calculate $\langle \hat{I} \rangle$, $\langle \hat{F} \rangle$, and $R = \langle \hat{F} \rangle A$, where R is the photon pair production rate and A is the cross-sectional area of the pump beam. As an example, we assume a typical beam radius of 100 μm, corresponding to $A = \pi \times 10^{-4}$ cm^2. We choose 3 different cases of pump wavelength; $\lambda_p = 0.532$ μm (common green laser), $\lambda_p = 0.8$ μm (common near-IR laser), and $\lambda_p = 1.55$ μm (mid-IR, common telecommunications wavelength). In each case, we use a pump intensity of $I_p = 10$ GW/cm^2 and a propagation length of $L = 1$ mm. Eqs. (160), and (164) are integrated numerically to find the average intensity, flux, production rate, and second-order coherence function for each pump wavelength. The left panel of Fig. (27) corresponds to $\lambda_p = 0.532$ μm; the average intensity is found to be $\langle I \rangle = 620$ μW/cm^2, the average flux is $\langle F \rangle = 8.3 \times 10^{13}$ pairs/(s cm^2), $R = 2.6 \times 10^{10}$ pairs/s, and the $1/e^2-$width for $g^{(2)}(\tau)$ is $\tau_c = 2.5$ fs.
In the middle panel of Fig. (27), the pump wavelength is $\lambda_p = 0.8$ μm; the associated average intensity is found to be $\langle I \rangle = 54$ μW/cm^2, the average flux is $\langle F \rangle = 1.1 \times 10^{13}$ pairs/(s cm^2), $R = 3.4 \times 10^9$ pairs/s, and the $1/e^2-$width for $g^{(2)}(\tau)$ is $\tau_c = 3.4$ fs.
Finally, the far right panel of Fig. (27) corresponds to $\lambda_p = 1.55$ μm; the average intensity is found to be $\langle I \rangle = 1$ μW/cm^2, the average flux is $\langle F \rangle = 4.0 \times 10^{11}$ pairs/(s cm^2), $R = 1.3 \times 10^8$ pairs/s, and the $1/e^2-$width for $g^{(2)}(\tau)$ is $\tau_c = 7.2$ fs. As λ_p increases, $\langle I \rangle$, $\langle F \rangle$, and R decrease. This is consistent with the fact that for longer pump wavelengths, the maximum instability gain will be centered around longer wavelengths and will be weaker, consistent with Fig. (6) in Section 3. The coherence time, τ_c increases with λ_p.
The calculated photon pair production rates are consistent with Refs. [60, 61]. For example, in Ref. [60], the author uses pump power 1 W and wavelength of 0.42 μm. This means the pump supplies about 2.1×10^{18} photons/s, and the author quotes a generated biphoton rate of 1.3×10^{10} pairs/s. Same as above, if we assume an effective pump beam area of 10^{-4} cm^2, then the pump intensity is about 10^4 W/cm^2. This is significantly lower than our pump

intensity, but since the $\chi^{(2)}$ material, $LiNbO_3$, is used, it is consistent since $\chi^{(2)}$ materials have much higher nonlinear coefficients than $\chi^{(3)}$ materials.
Similarly, in Ref. [61], they use pump power 12 MW and wavelength of $0.355\,\mu$m. This means the pump supplies about 2×10^{25} photons/s, and the authors quote a generated biphoton rate of 10^6 photons/pulse. Each pulse is 17 ps long, so thats about 6×10^{16} photons/s. Same as above, if we assume an effective pump beam area of 10^{-4} cm^2, then the pump intensity is about 1.2×10^{11} W/cm^2. This is higher than our pump intensity, but they generate biphotons at a rate higher by about 6 to 8 orders of magnitude than our theory states and the above example. Again, it is consistent with above since they consider the BBO crystal, which is also a $\chi^{(2)}$ material.

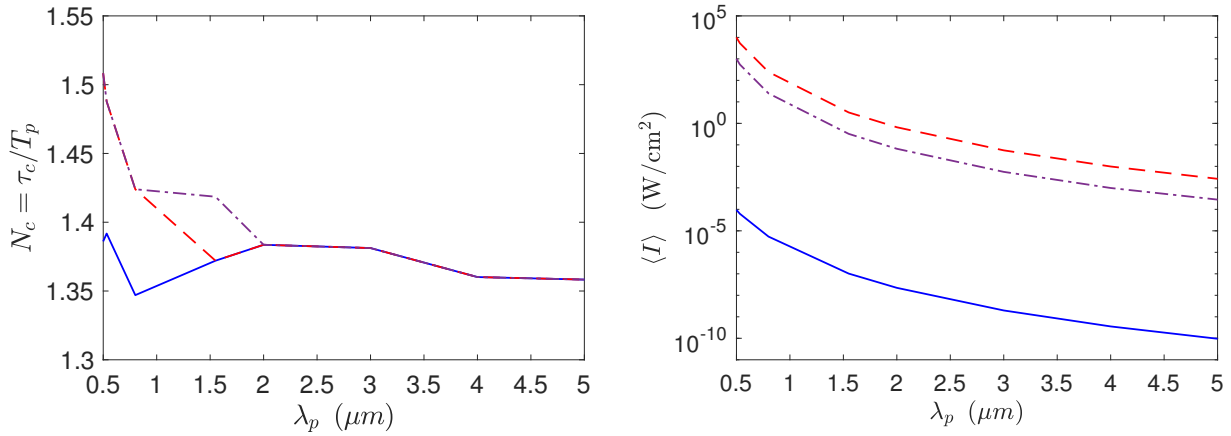

Figure 28: In the left panel, the number of cycles possible over coherence time of $g^{(2)}(\tau)$ from Eq. (168) is plotted as a function of λ_p. In the right panel, the average intensity of generated photons, from Eq. (160), is plotted as a function of λ_p. For both panels, CaF_2 is used, solid blue line is for $I_p = 10$ GW/cm^2, $L = 1$ mm, red dashed line is for $I_p = 3$ TW/cm^2, $L = 1$ mm, and purple dash-dotted line is for $I_p = 0.3$ TW/cm^2, $L = 10$ mm in each panel.

For a given pump wavelength, the number of cycles possible over the second-order coherence time depends on both $\tau_c(\lambda_p)$ and the pump frequency, $\nu_p = c/\lambda_p$, via $N_c = \tau_c \nu_p$. As λ_p increases, ν_p decreases, and the number of cycles as a function of λ_p is given by

$$N_c(\lambda_p) = \frac{c\tau_c(\lambda_p)}{\lambda_p} = \frac{\tau_c(\lambda_p)}{T_p(\lambda_p)}, \tag{168}$$

where $T_p = 1/\nu_p$ is the pump period. In Fig. (28), $N_c(\lambda_p)$, and $\langle I \rangle(\lambda_p)$ are plotted over a broad range of λ_p. Note that $\langle F \rangle(\lambda_p)$ and R are very similar qualitatively to $\langle I \rangle(\lambda_p)$, so we only plot $\langle I \rangle(\lambda_p)$ here. Any discussion on $\langle I \rangle$ applies also to $\langle F \rangle(\lambda_p)$ and R. The same material, CaF_2, is used, for various combinations of I_p and L. In the left panel of the figure,

the number of cycles defined by Eq. (28) is plotted from $\lambda_p = 0.5 - 5$ μm. The left panel of Fig. (28) shows that just over a single cycle is roughly maintained across the range of λ_p, with a small increase as λ_p gets shorter. Overall, over this range of λ_p, we can conclude that N_c does not depend strongly on these reasonable values of I_p and L.
In the right panel, the average intensity, $\langle \hat{I} \rangle$ increases with I_p. As λ_p is increased, $\langle \hat{I} \rangle$ decreases monotonically. Note that for higher I_p versus longer L, $\langle \hat{I} \rangle$ is bigger by an order of magnitude−compare red dashed line and purple dash-dotted line. Therefore, to achieve higher $\langle \hat{I} \rangle$, it is better to choose higher I_p and shorter L versus lower I_p and longer L.
Finally, in Fig. (29), we plot Eq. (167), which gives the probability distribution that a pair of N photons will be generated, as a function of frequency. The material chosen is CaF_2, and an interaction length of $L = 0.1$ mm. Different cases of pump intensity (columns) and pump wavelength (rows) are used to understand its effect on the photon distribution.

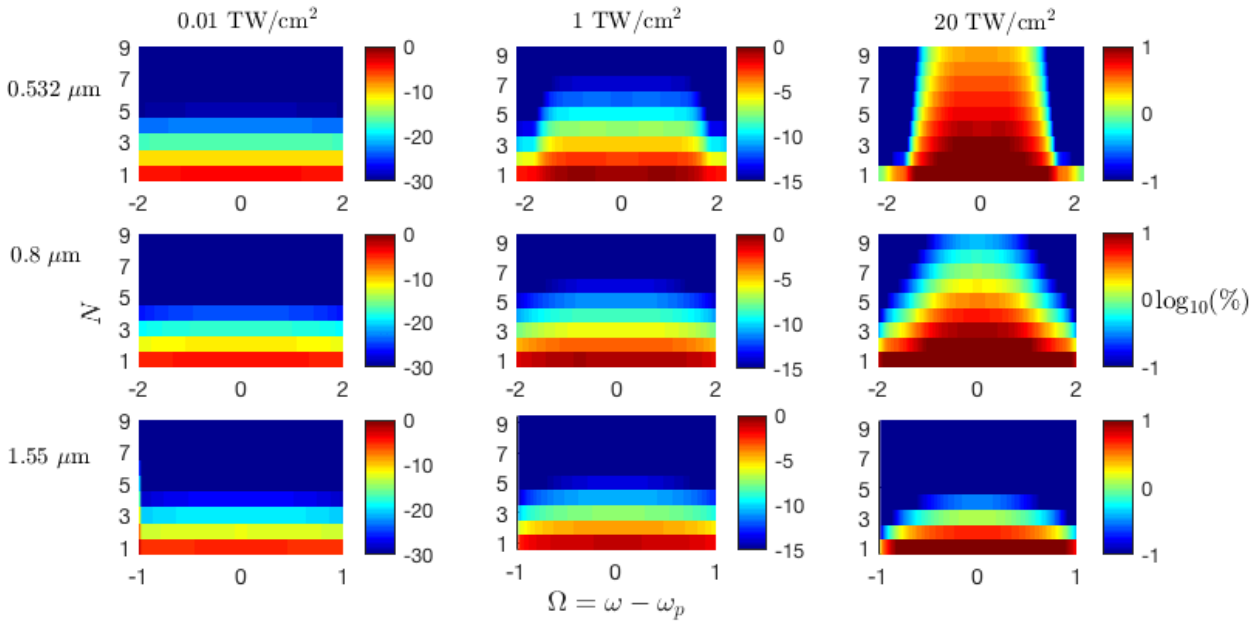

Figure 29: Probability distribution that a pair of N photons will be generated, as a function of frequency, given by Eq. (167) for CaF_2 for $L = 0.1$ mm. In each panel, the colour bar indicates the probability (in $\log_{10}(\%)$ for visibility). In the first, second, and third rows, $\lambda_p = 0.532$ μm, $\lambda_p = 0.8$ μm, and $\lambda_p = 1.55$ μm, respectively. In the first, second, and third columns, $I_p = 0.01$ TW/cm^2, $I_p = 1$ TW/cm^2, and $I_p = 20$ TW/cm^2, respectively.

In the first column of Fig. (29), the probability distribution is plotted for the lowest pump intensity of $I_p = 0.01$ TW/cm^2. At this level of pump intensity, only a single pair of photons has an appreciable probability of being generated, although pairs of larger N are still possible. As a general rule, as the pump wavelength increases, the probability of generating photon pairs decreases. As well, the photon pairs have more uniform probability across the whole spectrum.
In the middle column of Fig. (29), the pump intensity is increased to $I_p = 1$ TW/cm^2, and

the probability of generating a single pair of photons has increased by orders of magnitude across the spectrum. Most notably, here, pairs of 2 or 3 photons begin to have appreciable probabilities of being generated. As N increases, the probabilities of photons being generated are confined to smaller detunings from the pump frequency. Therefore, if a photon pair with a broad spectrum is generated, chances are very high that it is a single photon pair.
Finally, in the far right column of Fig. (29), the pump intensity is the highest at $I_p = 20$ TW/cm^2. Here, there is even higher probability of generating a single pair of photons, even up to about 10%. The most notable difference for the case of $N = 1$ is that the probability of generated photons have spectral widths that are less uniform, and it is tapered as N increases, decreasing the spectrum. Therefore, it seems that at higher intensities the photon pairs stretch over a smaller spectral domain.

7 Conclusion

7.1 Summary and results

In this section, the results of this work are summarized. The overarching theme of this work is exploring third-order optical (Kerr) nonlinear instability. Within the theory of Kerr instability, we explore an amplification scheme, which can be considered seeded conical emission. We name this amplification Kerr Instability Amplification (KIA).

In Chapter 2, the full classical theory is developed to obtain the vectorial wave equations of the instability. It is shown that for such materials of interest, vectorial effects are negligible across the instability regime and the scalar theory gives an accurate account of KIA. It is also shown that KIA is a spatiotemporal generalization to four-wave mixing, modulation instability, and filamentation instability, which avoids commonly used approximations that typically lead to the Nonlinear Schrodinger Equation (NLSE).

Following this, in Chapter 3, the theory of plane wave KIA is explored. This is of course an idealization, however, many of the key ideas of KIA are still quantified using plane wave theory, together with the two bulk dielectrics, calcium fluoride (CaF_2) and potassium bromide (KBr). As KIA theory does not use the paraxial approximation or approximations on the dispersion of the linear refractive index, it can reliably predict features of the amplification, such as a spectral range that extends from the second harmonic deep into the infrared, and large noncollinear angles. Quantitatively, the importance of pump wavelength, linear dispersive properties, and noncollinear angles for optimal amplification are demonstrated.

In Chapter 4, the effects of generalizing the seed beam to a finite pulse are explored, specifically a Gaussian beam. Using the same two materials as in the plane wave theory, the effect of a finite seed beam is quantitatively analyzed. Our analysis of KIA in CaF_2 and KBr crystals demonstrates the potential to amplify pulses in the wavelength range $\approx 1 - 14\,\mu$m. Whereas plane wave amplification in KBr extends to 40μm, material damage limits finite pulse KIA to about 14μm. There, seed pulse output energies in the $50\,\mu$J range appear feasible with a ratio of pump to seed pulse energy in the range 400-500. Our numbers are comparable to the performance of optical parametric amplifiers. The biggest three advantages of KIA are the capacity for single cycle pulse amplification, that it is intrinsically phase matched, and its simplicity and versatility. Kerr materials are more easily available than infrared materials with second-order nonlinearity. Further, amplifier wavelength can be selected by simply changing the angle between pump and seed beam. The biggest drawback is an angular chirp acquired during amplification that needs to be controlled.

The KIA gain profile is of Bessel-Gaussian nature in real space. Therefore, KIA lends itself naturally to the amplification of Bessel-Gauss beams. This is explored in Chapter 5. It is shown that the main advantages of Bessel-Gaussian seed pulses over Gaussian ones is their radial symmetry, which can align with the amplification profile about a ring in k-space, allowing for pump-to-seed energy amplification that is more efficient than the Gaussian case

by a factor of about $5-7$. Whereas in the Gaussian case, the efficiency is on the order of about $0.15-0.2\%$, in the Bessel-Gaussian case it is on the order of about 1%. The spatial walk-off between the maxima of the pump and seed beams for the Gaussian seed pulse significantly reduces the initial width along the dimension of the walk-off. Eventually, when this walk-off, together with the finite amplification profile, matches the width available from the pump, amplification is no longer possible. The symmetry of the Bessel-Gaussian profile results in no spatial walk-off, and hence amplification at longer wavelengths than in the Gaussian case is theoretically possible. Lastly, Bessel-Gauss beams are known to have favourable properties, such as being diffraction-free beams, at least over a limited propagation range [50]. We can conclude that it can be advantageous to use Bessel-Gaussian seed beams for amplification using KIA.

In Chapter 6, the quantized theory of KIA is developed, which is valid over a broad spectral and transverse range as in classical KIA. Further, as in the classical case, quantum KIA is shown to be a generalization to quantum four-wave Optical Parametric Amplifiers (FWOPAs). Subjecting a state that is initially a coherent state in the $(\Omega, \vec{k}_\perp)$ and vacuum in the $(-\Omega, -\vec{k}_\perp)$ mode to the KIA process results in a two-mode squeezed coherent state. As a result, the interplay between vacuum flucuations and the coherent state (seed beam) are directly evident (for example, see Eqs. (127) and (129)).
As with other two-mode squeezed states, the coupling between the two modes is responsible for the light being nonclassical, or having sub-Poissonian statistics [59]. In fact, it is found that the interplay between the coherent state (seed) amplitude and the average number of photons generated from vacuum determines whether the photon statistics are classical or non-classical, which may be tuned, see below Eq. (133). In general, when only one of the modes is considered, and the other is traced over (no measurement made on it), the resulting reduced photon statistics are always Poissonian (for $z = 0$) or super-Poissonian (for $z \geq 0$). That is, the photon statistics can be described classically. Specifically, in the TMSV case, the conical emission exhibits thermal (Bose-Einstein) statistics, consistent with Ref. [28].
In the limit when the coherent state amplitude is zero (no seed), the quantum state reduces to a generalized two-mode squeezed vacuum state (TMSV) [28]. In Section 6.5, the TMSV state is explored further, and a theory of generating pairs of correlated ultrafast photons (biphotons) is developed. It is shown that photon pairs exhibit second-order coherence that corresponds photon bunching that can be on the order of a single cycle due to the very broad spectral content of the photons that arise from vacuum via Kerr instability.

7.2 Future work

As for the amplification of ultra-short pulses, the results shown here are promising, but are likely still far from optimum. The amplification of Bessel-Gaussian beams shows promise over ordinary Gaussian beams, and experimental verification of this proposal would be interesting. Further to this, there are many variables to be considered, such as all potential infrared crystals and their respective linear and nonlinear dispersive properties. In fact, in

principle, KIA can be optimized by determining favorable optical properties (e.g. linear and nonlinear refractive indices) from our theory and then perhaps designing corresponding synthetic materials.

The quantized theory of Kerr instability should be explored further, to better understand how it may be applied for practical research purposes. For example, generating heralded ultrafast single photons and single cycle biphoton pulses. As well, since biphotons conserve energy and sum to $2\hbar\omega_p$, there is potential to use ultrafast biphotons in ultrashort pump probe experiments on spectrally narrow atomic systems. Further, exploring higher order perturbation theory should quantify the transition from the quantum to the classical regime of quantum nonlinear optical processes. Lastly, generalizing to a finite pump pulse in the instability analysis would provide a more complete picture, and allow one to better understand and quantify the onset of the filamentation instability process.

References

[1] R. W. Boyd, *Nonlinear Optics*, third edition, Academic Press, San Diego (2003).

[2] M. Melnichuk and L. T. Wood, "Direct Kerr electro-optic effect in noncentrosymmetric materials," Phys. Rev. A 82, 013821 (2010).

[3] V. Loriot, E. Hertz, O. Faucher, and B. Lavorel, "Measurement of high order Kerr refractive index of major air components", Opt. Express **17**, 16, pp. 13429 (2009).

[4] V. Loriot, P. Bejot, W. Ettoumi, Y. Petit, J. Kasparian, S. Henin, E. Hertz, B. Lavorel, O. Faucher, and J. Wolf, "On negative higher-order Kerr effect and filamentation," Laser Phys. **21**, pp. 1319−1328 (2011).

[5] V. I. Bespalov and V. I. Talanov, "Filamentary structure of light beams in nonlinear liquids," JETP Lett. **3**, 307 (1966).

[6] G. P. Agrawal, *Nonlinear Fiber Optics*, Academic Press, San Diego (1989).

[7] A. Couairon and A. Mysyrowicz, "Femtosecond filamentation in transparent media," Phys. Rep. **441**, 47, 47-189 (2007).

[8] A. Vincotte, and L. Berge, "$\chi^{(5)}$ susceptibility stabilizes the propagation of ultrashort laser pulses in air," Phys. Rev. A **70**, 6, (2004).

[9] M. Petrarca, Y. Petit, S. Henin, R. Delagrange, P. Bejot, and J. Kasparian, "Higher-order Kerr improve quantitative modeling of laser filamentation," Opt. Lett.**37**, 20, pp. 4347−4349 (2012).

[10] P. Bejot, J. Kasparian, S. Henin, V. Loriot, T. Vieillard, E. Hertz, O. Faucher, B. Lavorel, and J. Wolf, "Higher-order Kerr terms allow ionization-free filamentation in gases," Phys. Rev. Lett. **104** (2010).

[11] P. Polynkin, M. Kolesik, E. M. Wright, and J. V. Moloney, "Experimental tests of the new paradigm for laser filamentation in gases," Phys. Rev. Lett. **106**, 15, (2011).

[12] D. L. Weerawarne, X. Gao, A. L. Gaeta, and B. Shim, "Higher-order nonlinearities revisited and their effect on harmonic generation," Phys. Rev. Lett. **114** (2015).

[13] J. Doussot, G. Karras, F. Billard, P. Bejot, and O. Faucher, "Resonantly enhanced filamentation in gases," Optica, **4**, 7, pp. 764−769, (2017).

[14] M. Hercher, "Laser-induced damage in transparent media," JOSA**54**, 563, (1964).

[15] F. Theberge et al., "Ultrabroadband conical emission generated from the ultraviolet up to the far-infrared during the optical filamentation in air," Opt. Lett. **33**, 21, (2008).

[16] P. Maioli, R. Salame, N. Lascoux, E. Salmon, P. Bejot, J. Kasparian, and J. P. Wolf, "Ultraviolet-visible conical emission by multiple laser filaments," Opt. Express **17**, 6, pp. 4726-4731 (2009).

[17] E. Rubino, J. Darginavičius, D. Faccio, P. Di Trapani, A. Piskarskas, and A. Dubietis, "Generation of broadly tunable sub-30-fs infrared pulses by four-wave optical parametric amplification," Opt. Lett. 36, 382–384 (2011).

[18] M. I. M. Abdul Khudus, F. De Lucia, C. Corbari, T. Lee, P. Horak, P. Sazio, and G. Brambilla, "Phase matched parametric amplification via four-wave mixing in optical microfibers," Opt. Lett. 41, 761–764 (2016).

[19] M. Nesrallah, G. Vampa, G. Bart, P.B. Corkum, C.R. McDonald and T. Brabec, "Theory of Kerr instability amplification", Optica 5(3), 271278 (2018).

[20] G. Vampa, T. J. Hammond, M. Nesrallah, A. Yu Naumov, P. B. Corkum and T. Brabec, "Light amplification by seeded Kerr instability", Science 359, 673–675 (2018).

[21] R. Gattass and E. Mazur, "Femtosecond laser micromachining in transparent materials", Nat. Photonics **2**, 219 (2008).

[22] S. Ghimire, A. D. Dichiara, E. Sistrunk, P. Agostini, L. F. Dimauro and D. A. Reis, "Observation of high-order harmonic generation in a bulk crystal", Nat. Phys. **7**, 138 (2011).

[23] M. Schultze, E. Bothschafter, A. Sommer, S. Holzner, W. Schweinberger, M. Fiess, M. Hofstetter, R. Kienberger, V. Apalkov, V. S. Yakovlev, M. I. Stockman, F. Krausz, "Controlling dielectrics with the electric field of light", Nature **493**, 75 (2013).

[24] P. Malevich, G. Andriukaitis, T. Flöry, A. J. Verhoef, A. Fernández, S. Ališauskas, A. Pugžlys, A. Baltuška, L. H. Tan, C. F. Chua and P. B. Phua, "High energy and average power femtosecond laser for driving mid-infrared optical parametric amplifiers", Opt. Lett. **38**, 2746 (2013).

[25] B. E. Schmidt, N. Thiré, M. Boivin, A. Laramée, F. Poitras, G. Lebrun, T. Ozaki, H. Ibrahim and F. Légaré, "Frequency domain optical parametric amplification", Nat. Commun. **5**, 3643 (2014).

[26] C. Manzoni and G. Cerullo, "Design criteria for ultrafast optical parametric amplifiers", J. of Opt. **18**, 103501 (2016).

[27] P. Krogen, H. Suchowski, H. Liang, N. Flemens, K. Hong, F. X. Kärtner and J. Moses, "Generation and multi-octave shaping of mid-infrared intense single-cycle pulses", Nat. Photonics **11**, 222 (2017).

[28] C. C. Gerry and P. L. Knight, *Introductory Quantum Optics*, Cambridge University Press, New York (2005).

[29] J. C. Diels (Editor), M. Richardson (Editor), and L. Arissian (Editor), *Light Filaments: Structures, Challenges and Applications*, IET, (to be published 2019).

[30] M. Nesrallah, A. Hakami, G. Bart, C. R. McDonald, C. Varin, and T. Brabec, "Measuring the Kerr nonlinearity via seeded Kerr instability amplification: conceptual analysis," Opt. Express 26(6), 7646−7654 (2018).

[31] M. Sheik-Bahae, D. C. Hutchings, D. J. Hagan, E. W. Van Stryland, "Dispersion of bound electronic nonlinear refraction in solids", IEEE J. Quant. Electron. **27**, 1269 (1991).

[32] E. D. Palik, *Handbook of optical constants of solids II*, Academic Press, Boston (1991).

[33] I. H. Malitson, "A redetermination of some optical properties of calcium fluoride", App. Opt. **2**, 1103 (1963).

[34] D. Milam, M. J. Weber, and A. J. Glass, "Nonlinear refractive index of fluoride crystals", Appl. Phys. Lett. **31**, 822 (1977).

[35] H. H. Li, "Refractive index of alkali halides and its wavelength and temperature derivatives", J. Phys. Chem. Ref. Data **5**, 329 (1976).

[36] R. DeSalvo, A. A. Said, D. J. Hagan, A. W. Van Stryland, and M. Sheik Bahae, "Infrared to ultraviolet measurement of two-photon absorption and n_2 in wide bandgap solilds", IEEE J. Quantum Electron. **32**, 1324 (1996).

[37] X. Gu, S. Akturk, and R. Trebino, "Spatial chirp in ultrafast optics," Opt. Commun. 242, 599–604 (2004).

[38] A. J. Campillo, "Small-scale self focusing," in Self Focusing: Past and Present, R. W. Boyd, ed. (Springer, 2009).

[39] M. Sheik-Bahae, A. A. Said, T. H. Wei, D. J. Hagan, and E. W. Van Stryland, "Sensitive measurement of optical nonlinearities using a single beam," IEEE J. Quant. Electr. **26**, 760 (1990).

[40] A. R. Gee, D. C. O'shea, and H. Z. Cummins, "Raman scattering and fluorescence in calcium fluoride," Solid State Commun. 4, 43–46 (1966).

[41] J. P. Hurrell, S. P. S. Porto, T. C. Damen, and S. Mascarenhas, "Raman scattering from mixed KBr, KCl crystals," Phys. Lett. A 26, 194–195 (1968).

[42] Gallais and M. Commandré, "Laser-induced damage thresholds of bulk and coating optical materials at 1030 nm, 500 fs," Appl. Opt. 53, A186–A196 (2014).

[43] M. Wu, Y. You, S. Ghimire, D. A. Reis, D. A. Browne, K. J. Schafer, and M. B. Gaarde, "Orientation dependence of temporal and spectral properties of high-order harmonics in solids", Phys. Rev. A 96, 063412 (2017).

[44] Y. Ma and M. Rohlfing, "Quasiparticle band structure and optical spectrum of CaF2", Phys. Rev. B 75, 205114 (2007).

[45] L. J. Page and E. H. Hygh, "Calculation of Energy Bands in Alkali Halides", Phys. Rev. B 1, 3472 (1970).

[46] M. Schultze, E. M. Bothschafter, A. Sommer, S. Holzner, W. Schweinberger, M. Fiess, M. Hofstetter, R. Kienberger, V. Apalkov, V. S. Yakovlev, M. I. Stockman, Ferenc Krausz, "Controlling dielectrics with the electric field of light", Na- ture 493, 75 (2013).

[47] P. A. Zhokhov and A. M. Zheltikov, "Field-cycle resolved photoionization in solids", Phys. Rev. Lett. 113, 133903 (2014).

[48] C. R. McDonald, G. Vampa, P. B. Corkum, and T. Brabec, "Intense-laser solid state physics: unravelling the difference between semiconductors and dielectrics", Phys. Rev. Lett. 118, 173601 (2017).

[49] O. Mendoza-Yero, G. Minguez-Vega, J. Lanzis, and V. Climent, "Diffractive pulse shaper for arbitrary waveform generation," Opt. Lett. 35, 535–537 (2010).

[50] F. Gori and G. Guattari, "Bessel-Gauss beams," Opt. Commun. 64, 6 (1987).

[51] M. McLaren, M. Agnew, J. Leach, F. S. Roux, M. J. Padgett, R. W. Boyd, and A. Forbes, "Entangled Bessel-Gaussian beams", Opt. Expr. 20, 23589 (2012).

[52] M. McLaren, J. Romero, M. J. Padgett, F. S. Roux, and A. Forbes, "Two-photon optics of Bessel-Gaussian modes", Phys. Rev. A 88, 033818 (2013).

[53] X. Chu, Q. Sun, J. Wang, P. Lu, W. Xie, and X. Xu, "Generating a Bessel-Gaussian beam for the application in optical engineering", Sci. Reports 5, 18665 (2015).

[54] I. S. Gradshteyn and I. M. Ryzhik, *Table of Integrals, Series, and Products*, seventh edition, Elsevier Academic Press, Burlington (2007).

[55] T. Brabec and F. Krausz, "Nonlinear optical pulse propagation in the single-cycle regime", Phys. Rev. Lett. **78**, 3282, (1997).

[56] B. Huttner, S. Serulnik, and Y. Ben-Aryeh, "Quantum analysis of light propagation in a parametric amplifier", Phys. Rev. A, **42**, 5594, (1990).

[57] Y. Lai and H. A. Haus, "Quantum theory of solitons in optical fibers. I. Time-dependent Hartree approximation," Phys. Rev. A, **40**, 844, (1989).

[58] N . Bogoliubov, "On the theory of superfluidity," Journal of Phys. **11**, 23, (1947).

[59] T. S. Lee, "Nonclassical photon statistics of two-mode squeezed states," Phys. Rev. A, **42**, 1608, (1990).

[60] I. N. Agafonov, M. V. Chekhova, and G. Leuchs, "Two-color bright squeezed vacuum", Phys. Rev. A, **82**, 011801(R), (2010).

[61] S. E. Harris, "Chirp and Compress: Toward Single-Cycle Biphotons", Phys. Rev. Lett. 98, 063602 (2007).

Appendix A Comparing exact and approximate solutions for KIA gain

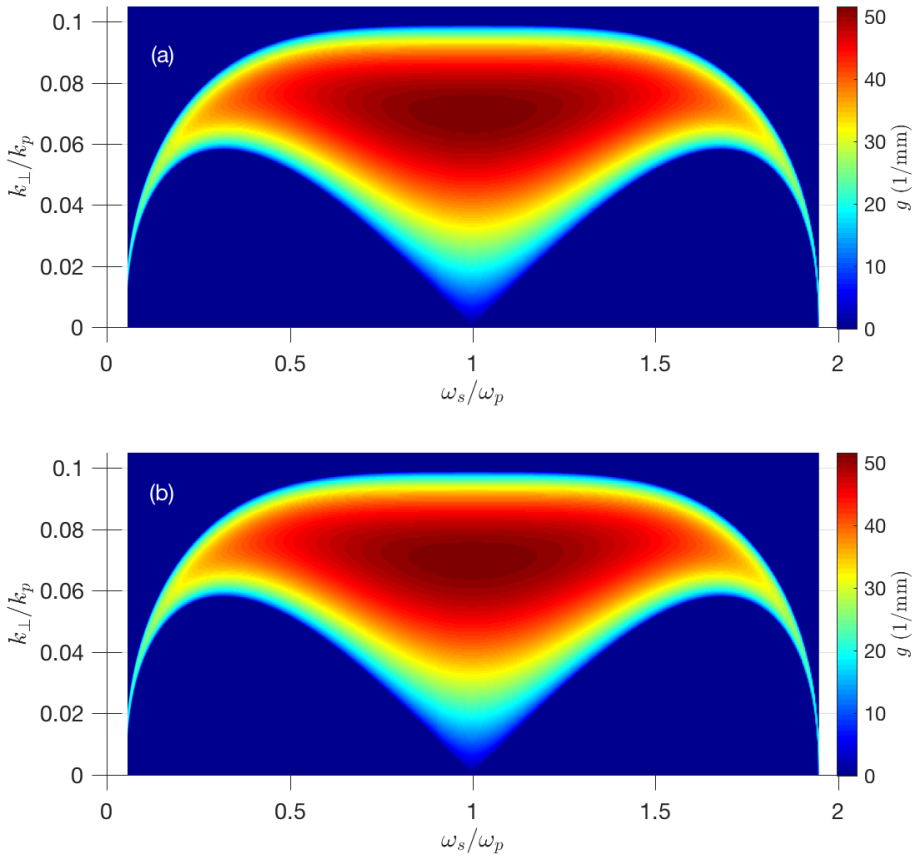

Figure 30: (a) is a replot of Fig. 6(a) in Chapter 3. (b) The exact solution of the quartic equation Eq. (47) for the parameters of Fig. 6(a).

In Fig. 30(a) we replot Fig. 6(a) from the main manuscript, which gives the KIA gain (Eq. (56)) in CaF_2, as obtained from a solution of the quadratic equation (51). The quadratic equation has been derived from the quartic equation (47) by neglecting counter propagating waves. No other approximations have been used. The quality of this solution is compared to the gain determined from a numerical solution of the coupled wave equations (27), (28), which is identical to solving the quartic equation (47). This exact solution is plotted in Fig. 30(b). The two solutions are practically identical proving that the analytical solution in Eq. (56) is virtually exact.

Appendix B Summary of definitions and parameters

We summarize the parameters and give their definitions used in scalar KIA theory, for both Chapters 3 and 4.

Variable	Description
$\mathbf{E}(\mathbf{x},t)$	$\mathbf{E}(\mathbf{x},t) = \boldsymbol{\varepsilon}(\mathbf{x},t) +$ $\hat{\mathbf{x}} E_p \exp(i\omega_\mathrm{p} t - ik_p z) + \mathrm{c.c.}$
E_p	Pump electric field amplitude
ω_p	Pump angular frequency
k_p	Pump wavevector

Variable	Description
$\boldsymbol{\varepsilon}(\mathbf{x},t)$	Small perturbation (seed)
$n(\omega)$	Linear refractive index
n_2	Optical Kerr nonlinear index
n_n	$n_n = n_2 I_p$
I_p	Pump intensity
$\boldsymbol{v}(\mathbf{x},t)$	$\boldsymbol{v}(\mathbf{x},t) = \boldsymbol{\varepsilon}(\mathbf{x},t) \times$ $\exp(-i\omega_\mathrm{p} t + ik_\mathrm{p} z)$
$\boldsymbol{k}_\perp$	Transverse wavevector
$\tilde{\boldsymbol{v}}(z, \boldsymbol{k}_\perp, \Omega)$	Fourier transform of $\boldsymbol{v}(\mathbf{x},t)$
k_v	$k_v = \sqrt{k^2 + 2k_n}$

Variable	Description
k	$k = n(\omega)\omega/c$
k_n	$k_n = \sqrt{n_n}\omega/c$
$k_\perp^2$	$k_\perp^2 = k_x^2 + k_y^2$
$\tilde{\boldsymbol{v}}_{(-)}^*$	$\tilde{\boldsymbol{v}}_{(-)}^* = \tilde{\boldsymbol{v}}^*(-\Omega)$
η	$\eta = \sqrt{n^2 + 2n_n}$
η_p	$\eta_p = \eta(\omega_p) = \eta(\Omega = 0)$
$\Delta\eta(\Omega)$	$\Delta\eta(\Omega) = \eta(\omega_p + \Omega) - \eta_p$
$\eta_g(\Omega)$	$\eta_g(\Omega) = [\Delta\eta(\Omega) + \Delta\eta(-\Omega)]/2$
$\eta_u(\Omega)$	$\eta_u(\Omega) = [\Delta\eta(\Omega) - \Delta\eta(-\Omega)]/2$
$D_g(\Omega)$	Even dispersion function
$D_u(\Omega)$	Odd dispersion function
β_1	$\beta_1 = [dk/d\omega](\omega_p)$
β_2	$\beta_2 = [d^2k/d\omega^2](\omega_p)$
σ	$\sigma = [k_v(\omega_p) + D_g]/k_p$
$\sigma^2 - 1$	$\sigma^2 - 1 \approx (k_n(\omega_p)/k_p)^2 + 2D_g/k_p$
$\kappa_\perp$	$\kappa_\perp = \sqrt{(k_p^2 - D_u^2)(\sigma^2 - 1)}$
K_v	$K_v = K_u + K_g$
K_u	$K_u = -\sigma D_u \left[1 - \frac{(\kappa_\perp^2 - k_\perp)^2}{2(k_p^2 - \sigma^2 D_u^2)}\right]$
K_g	$K_g = -\frac{k_p\sqrt{(\kappa_\perp^2 - k_\perp)^2 - \delta_\perp^4}}{2(k_p^2 - \sigma^2 D_u^2)}$
g	Intensity gain, $g = -2\mathrm{Im}(\mathrm{K_g})$
$\bar{k}_\perp$	Transverse wavevector for max gain
$\bar{g}$	Max intensity gain
$\delta_\perp$	Transverse instability half-width

l	Kerr material length
$\bar{k}_{\perp s}$	$\bar{k}_{\perp s} = \bar{k}_\perp(\Omega_s)$
$\mathbf{K}(\Omega_s)$	Instability wavevector
K_z	$K_z = k_p + \sigma D_u$
K_{zs}	$K_{zs} = K_z(\Omega_s)$
E_s	Seed electric field strength
ω_s	$\omega_s = \omega_p + \Omega_s$
ν_s	Seed frquency, $\nu_s = \omega_s/(2\pi)$
θ_s	$\theta_s = \arctan\left(\bar{k}_{\perp s}/K_{zs}\right)$
$\lambda_{p,s}$	Pump, seed wavelength

Variable	Description
$\mathrm{w}_{x,y}(0)$	$1/e^2$ initial seed widths, $\mathrm{w}_{x,y}(0) = \mathrm{w}_{x,y}$
$\Delta_{x,y}$	$\Delta_{x,y} = 2/\mathrm{w}_{x,y}$
$\tau(0)$	$1/e^2$ initial seed duration, $\tau(0) = \tau = T_s$
Δ_ω	$\Delta_\omega = 2/\tau$
$\tilde{v}_x(0)$	Initial Fourier-transformed Gaussian seed pulse
$f(\Omega)$	$f(\Omega) = \exp\left(-(\Omega - \Omega_s)^2/\Delta_\omega^2\right)$
g_2	$g_2 = \frac{2k_p\bar{k}_\perp^2}{\delta_\perp^2(k_p^2 - \sigma^2 D_u^2)}$
$\tilde{v}_x(\boldsymbol{k}_\perp, l, \Omega)$	Fourier beam amplitude at l
α	$\alpha = \frac{\sigma D_u}{k_p^2 - \sigma^2 D_u^2}$
$\tilde{v}_x(x, y, l, \Omega)$	Amplified, shifted seed
γ	$\gamma = \bar{g} - g_2(\bar{k}_\perp - \bar{k}_{\perp s})^2$
$\varkappa$	$\varkappa = \sigma D_u - \alpha/2(\bar{k}_\perp^2 - \bar{k}_{\perp s}^2)$
q_x	$q_x = \mathrm{w}_x^2 + 2(g_2 + i\alpha)l$
q_y	$q_y = \mathrm{w}_y^2 + 2i\alpha l$
$\mathrm{w}_{x,y}(l)$	$\mathrm{w}_{x,y}(l) = \frac{\lvert q_{x,y}\rvert}{\sqrt{\mathrm{Re}(q_{x,y})}}$
x_c	Complex seed center, $x_c = x_{cr} + ix_{ci}$
x_{cr}	$x_{cr} = \alpha l \bar{k}_{\perp s}$
x_{ci}	$x_{ci} = g_2 l(\bar{k}_\perp - \bar{k}_{\perp s})$
$\lvert\tilde{v}_x(l)\rvert^2$	Intensity spectrum of amplified complex-shifted Gaussian seed
ξ_{cr}	$\xi_{cr} = x_{cr} + x_{ci}(\mathrm{Im(q_x)}/\mathrm{Re(q_x)})$
Γ	$\Gamma = \bar{g} - g_2(\bar{k}_\perp - \bar{k}_{\perp s})^2 \frac{\mathrm{w}_x^2}{\mathrm{Re}(q_x)}$
Γ_s	$\Gamma_s = \Gamma(\Omega_s)$
$\tau_g(l)$	$\tau_g(l) = \sqrt{\tau^2 - \Gamma_s'' l}$
$\Delta_\omega(l)$	$\Delta_\omega(l) = 2/\tau_g(l)$
$\tau(l)$	Actual pulse duration after l
$W_s(l)$	Amplified seed pulse energy
$W_s(0)$	Initial seed pulse energy $W_s(0) = (\pi/2)^{3/2} I_s \tau \mathrm{w}_x \mathrm{w}_y$
I_s	Initial seed intensity
$\Delta\beta_1$	Group velocity mismatch, $\Delta\beta_1 = \beta_{1s} - \beta_1$

Variable	Description
w_p	Pump width, $\mathrm{w}_p = r\,(\mathrm{w}_x(l) + 0.5\lvert\xi_{cr}\rvert)$
τ_p	Pump duration, $\tau_p = r\,(\tau(l) + 0.5\lvert\Delta\beta_1\rvert l)$
r	Pump to seed width ratio, $r = 3$
W_p	Pump energy, $W_p = (\pi/2)^{3/2} I_p \tau_p \mathrm{w}_p^2$
l_{sf}	Self-focusing length, $l_{sf} = \mathrm{w}_p\sqrt{n_p/(2n_n)}$
l_n	Nonlinear length, $l_n = 2n_p c/(n_n\omega_p)$
l_d	Dispersion length, $l_d = 2\tau_p^2/\beta_2$
F_{th}	Damage threshold fluence
I_{th}	Damage threshold intensity, $I_{th} = \sqrt{2/\pi}F_{th}/\tau_p$

Table 2: Summary of the variables and their definitions used in Chapters 3 and 4.